Cross-Sectional Scanning Probe Microscopy on GaAs: Tip-Induced Band Bending, Buried Acceptors and Adsorbed Molecules

Dissertation
zur Erlangung des Doktorgrades
der Naturwissenschaften (Dr. rer. nat.)
der Fakultät für Physik
der Universität Regensburg

vorgelegt von

Gerhard Münnich

aus Deggendorf

Mai 2014

Promotionsgesuch eingereicht am: 09.04.2014
Die Arbeit wurde angeleitet von: Prof. Dr. Jascha Repp

Prüfungsausschuss:

Vorsitzender:	Prof. Dr. Jaroslav Fabian
1. Gutachter:	Prof. Dr. Jascha Repp
2. Gutachter:	Prof. Dr. Christian H. Back
Weiterer Prüfer:	Prof. Dr. Dominique Bougeard

Abstract

This thesis presents low temperature scanning probe experiments performed in the cross-sectional geometry (X-SPM) on GaAs samples. In the experiments presented here, three topics have been addressed.

The (110) surface of a GaAs-based heterostructure was utilized as a substrate to adsorb iron-II-phthalocyanine molecules. The molecules, probed from scanning tunneling microscopy (STM) and spectroscopy (STS), were found to be only weakly perturbed by the substrate, and thus to retain a possible single-molecule functionality. This finding is in analogy to molecules decoupled from a metal sample by an ultrathin insulating layer. Therefore, we have identified a system which may allow for the combination of single-molecule functionality with the rich versatility of semiconductor physics.

In the cross-sectional geometry used in our experiment, the built-in electrostatic potential of the heterostructure, which we use as substrate to adsorb molecules, can be accessed. Across a *p-i-n* junction, the electrostatic potential varies, offering a rich parameter space, in which the relevant energies, namely the vacuum level, the Fermi level, and the molecular resonances, can be tuned with respect to each other. We exploit the lateral adsorption position of iron-II-phthalocyanine molecules across a *p-i-n* junction as a quasi gate voltage to shift molecular resonances with respect to the constant Fermi level of the substrate. Thus, we demonstrate an experimental technique to tune the electronic properties of individual molecules.

Shallow acceptors buried subsurface in GaAs have been investigated from

combined STS and Kelvin probe force spectroscopy. From this combination of experimental techniques, one of the long-standing problems of scanning tunneling experiments on semiconductors, the tip-induced band bending, has been solved. Due to band bending, the energy scale in the tunneling junction is usually lost, which severely hampers the interpretation of experimental data. Here, we recover the zero point of the energy scale from Kelvin probe force spectroscopy. In particular, we find acceptor induced enhanced conductance similarly to be present in different band bending regimes. This finding contradicts single particle pictures of electronic transport through individual acceptors in an STM geometry used so far in this context, which demonstrates the need for an exact value of the zero point of the energy scale for a qualitative interpretation of STM data acquired on semiconductor surfaces.

Contents

1. Introduction

> One shouldn't work on semiconductors,
> that is a filthy mess...
>
> *(W. Pauli, 1931 [1])*

When the scanning tunneling microscope was invented in 1982, for the first time ever it became possible to image the atomic structure of a flat surface in real space [2]. In later years, many derivations of the STM have been developed, first and foremost to mention the atomic force microscope (AFM) [3], which are all based on the concept of a probe tip locally interacting with a sample surface. The STM and all its derivations are hence referred to as scanning probe microscopy (SPM). By now, SPM is one of the most powerful techniques to probe and manipulate the electronic and geometric structure of matter at the single atom scale.

Since its early days, the SPM has been widely used to study the properties of semiconductors. Indeed, the break-through of the STM was its capability to resolve the so far puzzling geometry of the Si(111)–7×7 surface reconstruction in 1983 [5]. In 1985, R. Feenstra and A. P. Fein for the first time reported the imaging of a surface prepared by sample cleavage, as they investigated the (110) surface of the III-V semiconductor GaAs [6]. As the (110) surface plane is the cross section of (001) oriented wafers (see Fig. 1.1), such experiments are referred to as cross-sectional SPM.

The cross-sectional geometry offers quite unique experimental prospects to SPM. Sample preparation by wafer cleavage results in surfaces of unsurpassable cleanliness, as the cleavage reveals a previously buried atomic layer which never was exposed to ambient conditions. Further, in this

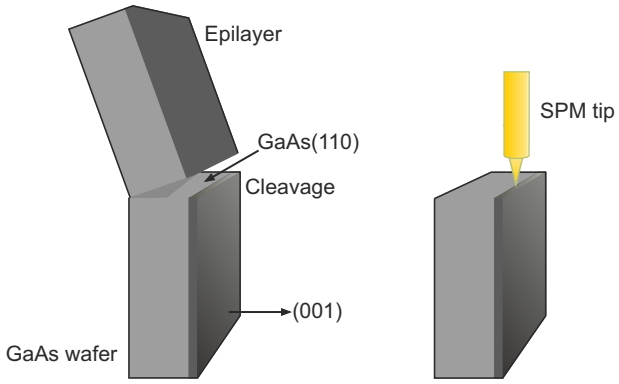

Figure 1.1: The principle of cross-sectional scanning probe microscopy. The surface imaged by the probe tip is prepared by wafer cleavage, that is, by mechanically removing the top part of a wafer. Thereby, a previously buried atomic layer is made accessible to the tip. After Ref. [4].

geometry all buried layers of epitaxially grown heterostructures can be simultaneously accessed by the microscope's tip (Fig. 1.1). Finally, in contrast to other semiconductor surfaces, the (110) surface of a III-V semiconductor has no surface states within its band gap. Hence, electrostatic fields are not screened at this surface, which allows the SPM to catch up the fingerprints of defects such as dopant atoms buried below the surface layer [7]. That is, the SPM is not limited to probe only features of the topmost atomic layer, but can directly access structures embedded entirely in the host material. However, the open band gap of the (110) surface at the same time is a severe impediment to STM. As the field of the probe tip is not screened at this surface, it partially drops off inside the sample, where it shifts the energetic positions of all sample states by an unknown amount and direction. This effect is referred to as tip-induced band bending [8], and due to this effect, not even at the most fundamental level the impact of the probe tip on the experiment can be neglected [9].

In this context, we performed STM and combined STM/AFM experiments on GaAs in the cross-sectional geometry. In our experiments,

we exploit the prospects offered by the GaAs(110) surface. In particular, we used a GaAs based heterostructure as a substrate to adsorb π-conjugated molecules, which we probe from STM and STS. The molecules were found to be only weakly disturbed by the substrate. As we have access to the cross-section, we use the built-in potential of the heterostructure to gate the individual molecules. Finally, we solve the long standing problem of the tip-induced band bending by a combination of STS with the AFM-based technique of Kelvin probe force spectroscopy. As a model system, we study the well known and technologically relevant system of individual shallow acceptors (zinc) buried in GaAs by combined STS and Kelvin probe force spectroscopy.

Part I.

Theoretical Background

2. Scanning Probe Microscopy

In scanning probe microscopy (SPM) a sharp probe tip is raster scanned above the surface of a sample, and a highly localized tip-sample interaction is utilized to produce an image of the surface. SPM is principally capable of resolving the electronic and geometric structure of matter at the atomic level.

The experimental data presented in this thesis were acquired using two different scanning probe techniques, namely scanning tunneling microscopy and atomic force microscopy. As illustrated in Figure 2.1, in STM the tip-sample interaction utilized for imaging is the tunneling current I which flows for sub-nanometer distances between a biased sample and a grounded probe tip. In AFM, one utilizes the force F_{ts} between the sample and the probe tip. The probe tip in AFM is attached to a flexible cantilever and F_{ts} can be detected in conceptually different ways. In frequency modulation AFM (FM-AFM), the tip is driven to oscillate at a constant amplitude, and the change in eigenfrequency of the oscillation is taken as a measure of F_{ts}. This technique is also referred to as non-contact AFM.

After a brief historical review, the theoretical background of STM and FM-AFM will be presented in the following chapters. The discussion presented here necessarily is incomplete, given the large field of SPM, and is strongly focused on what is directly related to the experimental data presented in part III of this thesis. Comprehensive overviews of the contents presented in this part can be found in Refs. [10–13].

SPM was pioneered by G. Binnig, H. Rohrer, Ch. Gerber and E. Weibl,

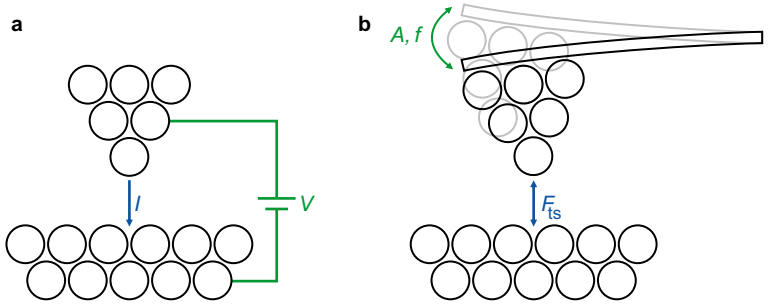

Figure 2.1: The basic principles of STM and of frequency modulation AFM. **a**, In STM, a metallic tip is placed atop a conducting sample. At a tip-sample distance in the sub-nanometer regime, a sample bias V results in a tunneling current I. **b**, In frequency modulation AFM, the tip is driven to oscillate at a constant amplitude A. The force F_{ts} between the tip and the sample changes the resonance frequency f of oscillation.

who in 1981 invented, designed, and built up the first STM [2, 14]. The impact of the STM on nanotechnolgy and surface science became clear immediately, when *atomically resolved* STM images clarified the true nature of the Si(111)–7×7 surface reconstruction [5], which was one of the great puzzles of surface science of the time. Consequently, only five years later the main contributors to the invention of the STM, G. Binnig and H. Rohrer, where awarded the Nobel prize in physics in 1986. Yet, the STM is much more than just a microscope capable of atomic resolution. It also allows the *manipulation* of matter at the single atom level, which was first demonstrated by D. Eigler and E. K. Schweizer, who in 1990 created single-atom scaled artificial structures by deliberately manipulating xenon atoms adsorbed on a nickel surface [15]. Besides imaging and manipulation, STM also allows *spectroscopy* of the electronic states of the sample, a technique referred to as scanning tunneling spectroscopy (STS). This was first demonstrated in 1987, when R. M. Feenstra, A. Stroscio, and A. P. Fein used STS to probe the band structure of the Si(111)–2×1 surface [16]. Since then, the STM has been successfully used to study and manipulate the electronic and geometric properties of a tremendous variety of surfaces and adsorbates, see e.g. Ref. [10] for a comprehensive overview on STM.

Despite its capabilities, STM has one major limitation. As STM utilizes a tunneling current, it can only be used on conductive samples [11]. This limitation was overcome in 1986, when G. Binnig, C. F. Quate, and Ch. Gerber extended the STM to the AFM [3]. As the AFM detects forces instead of a tunneling current, it can be used both on conductive as well as on insulating samples. As mentioned above, in AFM the probe tip is attached to a flexible cantilever. When Binnig et al. invented the AFM, they used the minute deflection of the cantilever as a measure of the tip-sample force. This mode of operation is referred to as "contact" or static operation mode. The first true atomic resolution from AFM was reported in 1995, when F. J. Giessibl utilized the "non-contact" (dynamic) mode to image the Si(111)–7×7 surface [17]. In dynamic AFM, first demonstrated by T. Albrecht et al. in 1991 [18], the prong is driven to oscillate, and changes in either the amplitude A or the frequency f of oscillation are utilized to detect the tip-sample force. Most often, the prong is driven to oscillate at a constant amplitude A and changes in the frequency of oscillation f are taken as a measure of the tip-sample force (FM-AFM). Since the beginning of FM-AFM, the oscillation of the prong was widely detected by means of a laser beam reflected from the prong and detected by a four-segmented photo-detector [19] and for many applications comparatively soft silicon-based cantilevers were used at large oscillation amplitudes. In 2000, F. J. Giessibl presented an all-electronic detection scheme for the prong oscillation, utilizing the piezoelectric effect present in a quartz tuning fork (qPlus sensor) [20]. Due to its all-electronic detection scheme and in particular due to the very high stiffness of the free prong of the quartz tuning fork, which allows for small oscillation amplitudes at very short tip sample distances, the qPlus sensor is highly suitable for the combination of STM and AFM.

The results presented in this thesis are obtained from STM and from combined qPlus based STM/AFM, strictly speaking, from STM and from the FM-AFM based technique of Kelvin probe force spectroscopy.

2.1. Scanning Tunneling Microscopy

STM is based on the concept of electron tunneling. Electron tunneling is a pure quantum mechanical phenomenon, which allows electrons of energy E to be transmitted through a potential barrier of height $V_0 > E$. The probability for an electron to tunnel from one side of the barrier to the other exponentially decays with barrier width d. As a rule of thumb, the tunneling probability is reduced by one order of magnitude as the barrier width increases by one angstrom [10]. Tunneling of electrons results in a tunneling current. As schematically depicted in Fig. 2.2a, in STM the tunneling current is maintained constant by a feedback-loop as the tip is raster scanned above the surface. The vertical movement z of the tip necessary to maintain a constant tunneling current (which, in the most simple case, corresponds to maintaining a constant tip-sample

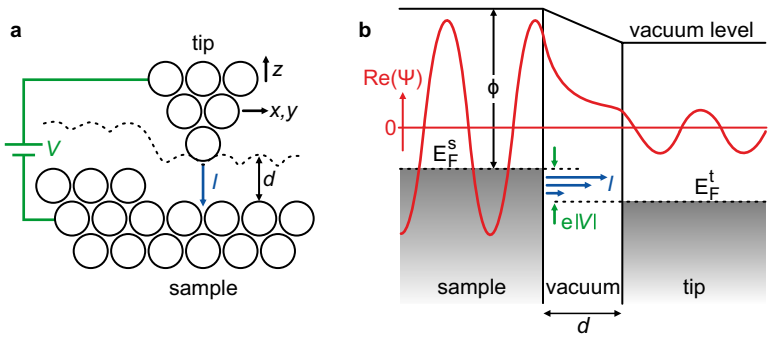

Figure 2.2: The concept of STM in a nutshell. **a**, Schematic representation of an STM tip scanned over a surface. The tip-sample distance d, typically a fraction of a nanometer, is kept constant. **b**, Energy diagram of the sample-vacuum-tip tunneling junction for a metallic tip and sample. Occupied states are shaded gray, the work function of the sample is denoted ϕ. The bias V applied between tip and sample shifts the Fermi and vacuum levels with respect to each other. Within the energy interval $E_\mathrm{F}^\mathrm{s} - eV$ and E_F^s, occupied states in the sample face empty states in the tip, which results in a tunneling current I. Overlaid is the real part of a sample-state wave function of energy $E < \phi$, which penetrates into the region of the tip. After [10].

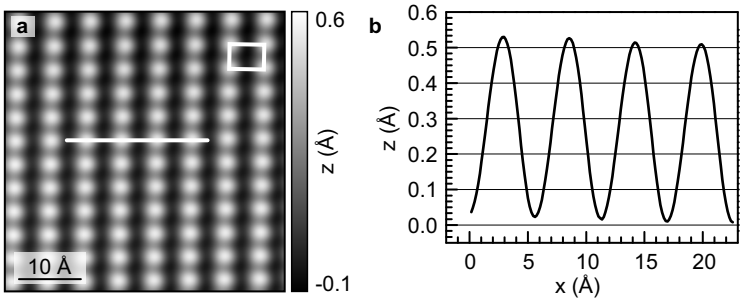

Figure 2.3: Constant current STM image and topography along line. **a**, Gray scale STM image of GaAs(110) acquired at $V = -1.3$ V, $I = 0.47$ nA. Bright and dark spots correspond to protrusions and depressions as indicated by the scale bar. At the particular sample bias chosen, the individual As atoms appear as protrusions. The white rectangle indicates a surface unit cell of dimensions 5.6×4.0 Å^2. **b**, Topography along a line along as indicated in (a). The slight overall shift on the order of 0.02 Å is attributed to an acceptor atom located deep below the surface layer.

distance d), is recorded for each lateral position (x, y) of the tip above the surface. The STM image is then the plot of the vertical tip position $z(x, y)$. This mode of operation of an STM is called the *constant-current mode*. As an example, Fig. 2.3 shows an atomically resolved constant-current STM image of the GaAs(110) surface. As will be detailed below, the contrast observed in an STM image is rather due to a variation of the electronic density of states of the sample than due to its topography only. The latter may be the case for a metallic surface, where the local density of states has no lateral variation, but it is typically not the case for a semiconducting sample. For example, in the negative-bias STM image of GaAs shown in Fig. 2.3, only one atom per surface unit cell is observed (the As atom), although the surface unit cell is composed of two atoms, each one Ga and one As atom.

As can be seen from Figure 2.3, our low-temperature STM routinely achieves lateral and vertical resolutions of a fraction of one angstrom. In general, the high spatial resolution in STM is enabled by the decay constant of the tunneling current of about one order of magnitude per

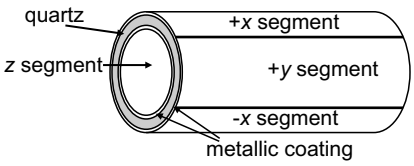

Figure 2.4: A piezo tube. The tube is fabricated from piezo-active quartz, its outer and inner surface are plated with a metallic coating. The outer coating is divided in segments. The tube changes its dimensions (e.g. bends) if a voltage is applied between the segments. After [10].

angstrom increase in tip-sample distance. Due to this, even a macroscopically blunt tip is capable of atomic resolution. Clearly, some atom at the tip's apex is the foremost one. Electrons tunneling from this atom will largely dominate the tunneling current, as the tunneling probability from any atom further away from the sample by one angstrom is suppressed by a factor of ten. For achieving sub-angstrom resolution, it is obvious that isolation against mechanical vibrations of the tunneling junction is one of the key elements. The vibration isolation system of our SPM setup is discussed in chapter 6. The stability of the tunneling junction is aided by the low temperatures (≈ 5 K) at which our experiments are performed. The latter is due to the reduced thermal drift as well as due to the low mobility of any adsorbates or adatoms present in the tunneling junction.

The horizontal and vertical motion of the tip is performed by a piezo drive. A piezo drive makes use of the inverse piezoelectric effect inherent in anisotropic crystals such as quartz [10]. This effect results in a deformation of the crystal if a voltage is applied. In our setup, tube-shaped piezos (Fig. 2.4) are used as a piezo drive. The piezo constant (i.e., the change of dimension of the tube per applied voltage) of a piezo tube typically is on the order of angstrom/volt.

2.1.1. Scanning Tunneling Microscopy - Theory

Much about STM can be understood already from considering the simple problem of a single electron tunneling through a one-dimensional, rec-

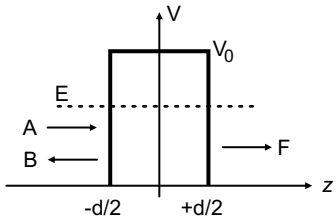

Figure 2.5: A one-dimensional rectangular barrier of height V_0 and width d. An electron of energy $E < V_0$ travels from left to right. A, B and F depict the impinging, reflected and transmitted part of the wave function. After [21].

tangular barrier. This problem is discussed in the following. Assuming a rectangular barrier of height V_0 and width d, $V(z) = V_0\Theta(d/2 - |z|)$ where Θ is the Heaviside function (Fig. 2.5), a piecewise solution to the corresponding time-independent Schrödinger equation for the wave function $\psi(z)$ can be found. For a single electron of energy $E < V_0$, it reads [21]:

$$\psi(z) = \begin{cases} A\mathrm{e}^{ikz} + B\mathrm{e}^{-ikz}; & z < -d/2 \\ C\mathrm{e}^{-\kappa z} + D\mathrm{e}^{\kappa z}; & |z| < d/2 \\ F\mathrm{e}^{ikz}; & z > +d/2 \end{cases} \tag{2.1}$$

where the wave number k and the inverse decay length κ are given by $k = \sqrt{2mE}/\hbar$ and $\kappa = \sqrt{2m(V_0 - E)}/\hbar$, respectively, and m and $\hbar$ are the mass of the electron and the reduced Planck's constant. The real part of $\psi(z)$ is sketched in Fig. 2.2b. The coefficients A, B, C, D and F in Eq. 2.1 depend on each other, as the wave function $\psi(z)$ and its derivate $\mathrm{d}\psi(z)/\mathrm{d}z$ have to be continuous at $z = \pm d/2$. For a wide and high barrier ($\kappa d \gg 1$), the transmission probability $T = |F|^2/|A|^2$ is approximately given by [21]:

$$T \cong \exp\left(-2\sqrt{2m(V_0 - E)}\frac{d}{\hbar}\right). \tag{2.2}$$

From classical mechanics, an electron of energy $E < V_0$ would be reflected from the barrier. From quantum mechanics, however, we see that there is a finite probability T for the electron to tunnel through the barrier. Under the assumptions made, the tunneling probability exponentially decays with barrier width d and with barrier height V_0.

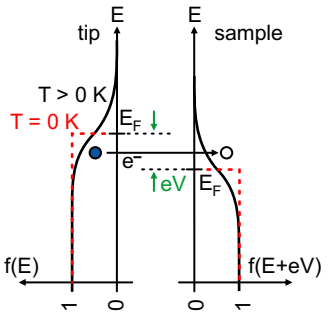

Figure 2.6: The Tersoff-Hamann picture of electron tunneling. The black (dashed red) curve depicts the Fermi distribution of occupation probability $f(E)$ at finite (zero) temperature T. The distributions in tip and sample are shifted w.r.t. each other by the applied bias eV. Electron tunneling occurs only between occupied (filled circle) and unoccupied (open circle) states located at the same energy E.

For a metal-vacuum-metal tunneling junction, the tunneling barrier V_0 of a state located at the Fermi level is given by the work function ϕ of the metal (assuming both metals have an equal work function), see Fig. 2.2b. The work function of a metal typically is about $\phi \approx 5$ eV [10]. From this, the inverse decay length $\kappa = \sqrt{2m\phi}/\hbar$ is estimated to be about $\kappa \approx 1.1$ Å^{-1}. According to Eq. 2.2, this value results in a decay of the tunneling probability (and hence of the tunneling current) by a factor of 9.8 per angstrom increase in barrier width. This decay of about one order of magnitude in tunneling current per angstrom tip-sample distance is one of the key features of STM. As already explained above, it is the reason for the high spatial resolution obtained in STM.

While the one-dimensional model described above qualitatively explains the dependence of the tunneling current on gap width, a more realistic description is necessary for a quantitative understanding of the tunneling process. A three-dimensional many-body description of electron tunneling was presented in 1961 (that is, two decades *before* the invention of the STM) by J. Bardeen [22] and applied to STM in 1985 by J. Tersoff and D. R. Hamann [23]. In the Tersoff-Hamann model, the tunneling current I is given to first order by:

$$I = \frac{2\pi}{\hbar} e^2 \sum_{\mu,\nu} f(E_\mu)\left[1 - f(E_\nu + eV)\right] |M_{\mu\nu}|^2 \delta(E_\mu - E_\nu) \qquad (2.3)$$

where $f(E)$ is the Fermi function, V is the bias applied between tip and sample, $M_{\mu\nu}$ is Bardeen's tunneling matrix element, $\delta(E)$ is Dirac's delta

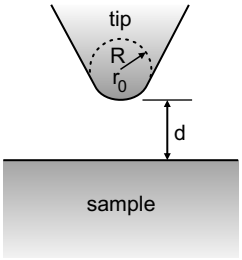

Figure 2.7: The Tersoff-Hamann picture of the tunneling geometry. A spherically symmetric probe tip with radius of curvature R is separated by a shortest distance d from the sample surface. The center of curvature of the probe tip is located at r_0. After [23].

function, and finally, the summation runs over all electronic states in the tip (subscript μ) and in the sample (subscript ν) [11]. This equation can be understood as follows. First, tunneling can only occur from occupied to empty states. The latter is ensured by the Fermi functions, which yield the probability of occupation of an electronic state of energy E, see Fig. 2.6. Second, energy has to be conserved, which is taken into account by Dirac's delta function. That is, a tunneling event occurs only between two states equal in energy (elastic tunneling). Finally, Bardeen's tunneling matrix element $M_{\mu\nu}$ must be non-zero [11]. As shown by Bardeen, $M_{\mu\nu}$ is evaluated from

$$M_{\mu\nu} = \frac{\hbar^2}{2m} \int_A \left(\chi_\mu^* \nabla \psi_\nu - \psi_\nu \nabla \chi_\mu^* \right) \cdot d\vec{S} \tag{2.4}$$

where χ_μ and ψ_ν denote electronic wave functions of the tip and of the sample, respectively, and the integral is evaluated on an infinite surface area A located entirely in the vacuum region separating tip and sample [22]. Without further assumption on the sample wave functions, but for an assumed radial symmetry of the tip wave functions (that is, for an s-wave tip), Tersoff and Hamann have shown that

$$M_{\mu\nu} = \frac{\hbar^2}{2m} 4\pi \Omega_t^{-1/2} R e^{\kappa R} \psi_\nu(\vec{r}_0) \tag{2.5}$$

where $\vec{r}_0$ and R are the center and radius of curvature of the probe tip as depicted in Fig. 2.7, and Ω is the volume of the probe tip, and κ finally is the inverse decay length $\kappa = \sqrt{2m\phi}/\hbar$ introduced above [23]. Substituting this into Eq. 2.3 and taking the limit of low temperature

($T \lesssim 300$ K) and of small bias voltage ($|V| \lesssim 10$ mV) yields the desired result for the tunneling current:

$$I = \frac{32\pi e^2 R^2 \phi^2 \mathrm{e}^{2\kappa R}}{\hbar \kappa^4} V \rho_{\mathrm{tip}}(E_{\mathrm{F}}) \sum_{\nu} |\psi_\nu(\vec{r_0})|^2 \delta(E_\nu - E_{\mathrm{F}}), \tag{2.6}$$

where $\rho_{\mathrm{tip}}(E_{\mathrm{F}})$ is the density of states (DOS) per unit volume of the probe tip taken at the Fermi energy [23]. Note that the effect of the low-temperature limit was to reduce the Fermi functions to step functions as depicted in Fig. 2.6. As the definition of the local density of states $\rho(\vec{r}, E)$ is given by

$$\rho(\vec{r}, E) = \sum_{\nu} |\psi_\nu(\vec{r})|^2 \delta(E_\nu - E), \tag{2.7}$$

the insight gained from Eq. 2.6 is the following. For an *s*-wave tip, assuming low temperatures and small bias voltages, constant current STM images resemble *contours of constant local density of states* of the sample taken at the Fermi level [23].

For our experiments, performed at the temperature of liquid Helium, clearly the low-temperature limit is valid. However, as we typically use sample biases on the order of volts, the low sample bias limit is not valid. Assuming that Bardeen's tunneling matrix element is independent of energy, Tersoff and Hamann's theory of tunneling can easily be extended to finite bias voltages. The equation for the tunneling current then reads:

$$I = \frac{4\pi e}{\hbar} \int_0^{eV} \rho_{\mathrm{tip}}(E_{\mathrm{F}} - eV + \epsilon) \rho_{\mathrm{sample}}(E_{\mathrm{F}} + \epsilon) |M|^2 d\epsilon \tag{2.8}$$

where ρ_{tip} and ρ_{sample} are the density of states of the tip and the sample, respectively [10]. In the case of a finite bias[1], all states within the energy interval eV contribute to tunneling, as it is depicted in Fig 2.1b. This is taken into account by integrating over this energy interval, and the current then reflects the *convolution* of tip and sample DOS. To gain

[1] Note that in our SPM the bias is applied to the sample. That is, a positive bias corresponds to tunneling of electrons from the tip into the sample, while a negative bias corresponds to tunneling of electrons from the sample into the tip.

further insight, the tip density of states $\rho_{\mathrm{tip}}(E)$ in Eq. 2.8 is assumed to be constant within the energy interval eV around the Fermi level $\rho_{\mathrm{tip}}(E) = \rho_{\mathrm{tip}}(E_{\mathrm{F}})$. Re-invoking the definition of the local density of states (Eq. 2.7), the tunneling current is then proportional to:

$$I \propto \rho_{\mathrm{tip}}(E_{\mathrm{F}}) \int_0^{eV} \rho_{\mathrm{sample}}(E_{\mathrm{F}} + \epsilon, \vec{r}_0) d\epsilon. \tag{2.9}$$

Hence, at finite bias voltage the tunneling current is derived from the integration over the local density of states of the sample from E_{F} to $E_{\mathrm{F}} + eV$. Constant current images acquired at finite sample biases therefore reflect the integrated local density of states of the sample.

2.1.2. Scanning Tunneling Spectroscopy - Theory

From Eq. 2.9, the differential conductance, $dI/dV(V)$, is found to be

$$\frac{dI}{dV}(V) \propto \rho_{\mathrm{sample}}(E_{\mathrm{F}} + eV, \vec{r}_0). \tag{2.10}$$

In the framework of the assumptions made, this quantity is proportional to the local density of states of the sample at the energy $E_{\mathrm{F}} + eV$. In *scanning tunneling spectroscopy* (STS), the bias voltage V is ramped while the differential conductance is recorded. As an example, Fig. 2.8 shows conductance and differential conductance spectra acquired on bare Cu(111) and on bare p-type GaAs(110), respectively. The most prominent features of these two surfaces are the presence of a surface state on Cu(111) at around -0.45 eV (taken with respect to the Fermi level of Cu) [24], and the presence of the bulk band gap of width $E_{\mathrm{g}} = 1.5$ eV on GaAs(110) [8], respectively. Clearly, the spectra acquired on Cu(111) show non-zero current and differential conductance within the entire bias interval, as it is expected for a (gap-less) metallic sample. The spectrum shows a peak in the differential conduction at around -0.45 V, which corresponds to the surface state expected at this voltage. The spectra acquired on GaAs(110), on the other hand, show zero current and differential conduction within a bias interval of about 1.5 V, which corresponds

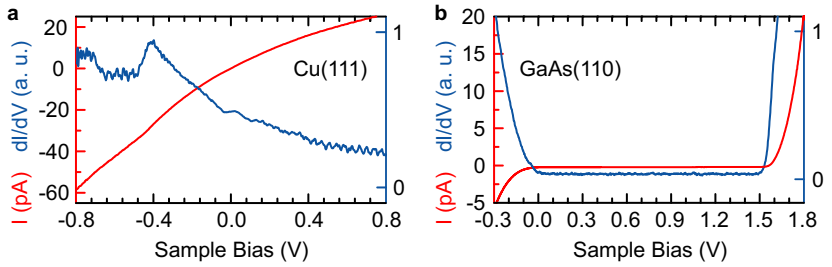

Figure 2.8: Scanning tunneling spectroscopy. **a**, $I(V)$ and $\mathrm{d}I/\mathrm{d}V(\mathrm{V})$ tunneling spectra acquired on clean Cu(111). As expected for a metallic sample, the spectra show non-zero conductance for all sample biases. The feature observed at around -0.45 V corresponds to a surface state present on Cu(111). **b**, $I(V)$ and $\mathrm{d}I/\mathrm{d}V(\mathrm{V})$ tunneling spectra acquired on the (110) surface of p-doped GaAs. The tunneling conductance is zero within a bias interval from zero to about $+1.5$ V. The width and the location of the zero-conductance-interval correspond well to the known band-gap of GaAs of $E_\mathrm{g} = 1.52$ eV and to the p-type doping of the sample.

well to the region of zero density of states (e.g., the band gap) present on this surface.

In the derivation of Eq. 2.10, the energy dependence of the tunneling matrix element $M_{\mu\nu}$ and the tip's density of states ρ_tip have been assumed to be constant within the energy interval eV around the Fermi level. For a metallic tip, a constant density of states ρ_tip around the Fermi level may be justified. The independence of $M_{\mu\nu}$ on energy, however, is questionable. As discussed by C. J. Chen, the effect of the energy dependence of $M_{\mu\nu}$ can be seen from Eq. 2.5, considering the exponential decay of the sample wave function $\psi_\nu(d)$ into vacuum; $\psi_\nu(d) \propto \exp(-\kappa_\nu d)$, where κ_ν is the inverse decay length corresponding to a state of the sample of energy E_ν, that is $\kappa_\nu = \sqrt{2mE_\nu/\hbar^2}$ [10]. That is, Bardeen's tunneling matrix element depends on energy as

$$M_{\mu\nu} \propto \exp\left(-\sqrt{2mE_\nu}\frac{d}{\hbar}\right). \tag{2.11}$$

Substituting this into Eq. 2.8, one sees that the effect of the energy dependence of the tunneling matrix element is to exponentially suppress

the contribution of states located energetically below E_F. In Fig. 2.2b, this suppression is indicated by the different arrow length indicating the tunneling current I. Note that similar arguments on the energy dependence of the tunneling matrix element have been presented by R. J. Hamers [25]. For STS, the energy dependence of the tunneling matrix element has the following consequence. An additional term in $dI/dV(V)$ occurs, which is the partial derivative of of the tunneling matrix element with respect to energy. Hence, only for matrix elements smoothly varying with energy, the quantity $dI/dV(V)$ can be interpreted in terms of the density of states of the sample only. In the experiments presented here, we have quantified the spectroscopic reliability of the particular tip apices by performing STS on bare Cu(111), the spectra of which is well known (Fig. 2.8), before taking spectra of dopant atoms buried below the surface layer of GaAs. Unreliable tip apices where changed by soft indentations into the Cu(111) surface.

This section is summarized as follows. STM images reflect the integrated local density of states rather than the geometry of the sample. All electronic states of the sample within the energy interval from E_F to $E_F + eV$ contribute to the tunneling current, but the latter (and hence the STM image) is dominated by the highest state tunneling. For a tip density of states and a tunneling matrix element only smoothly varying with energy, tunneling spectra reflect the local denstiy of states of the sample.

2.2. Atomic Force Microscopy

In similarity to STM, in AFM a probe tip locally interacts with a sample surface. In AFM the forces between the tip and the sample are sensed as instead of a tunneling current.

Several conceptually different measuring schemes exist in AFM. Here, we only focus on the non-contact frequency modulation mode. In this mode, the flexible cantilever is mechanically driven to oscillate at its

eigenfrequecy f_0 with a constant amplitude A, without the tip making contact to the sample[2]. This mode is depicted in Fig. 2.1b. As the tip is brought close to the surface, the tip-sample interaction starts to influence the resonance frequency f of the cantilever. While the amplitude of oscillation A is kept constant by a closed feedback-loop, the frequency shift $\Delta f = f_0 - f$ is taken as a measure of the force acting on the cantilever. As frequencies can be measured easily with high accuracy of a fraction of one Hertz at a base frequency of several hundred kilohertz, FM-AFM is particularly suitable for the detection of weak forces of below one nanonewton [10].

In similarity to STM, in AFM the cantilever (to which the tip is attached) is moved above the surface by a piezo drive. An additional piezo excites the cantilever to oscillate at or close to its eigenfrequency, by mechanically shaking the cantilever.

As in this thesis not AFM but the AFM-derived technique of Kelvin probe force spectroscopy is utilized, the description of AFM given here is limited to the basic features necessary to the understanding of KPFS. A detailed description of KPFS is then provided in chapter 5.

2.2.1. Frequency Modulation Atomic Force Microscopy - Theory

In FM-AFM, the tip is rigidly mounted to a flexible prong which is driven to oscillate at or close to its eigenfrequency, and the observable is the frequency shift Δf of the cantilever. In this section, the connection between Δf and the force F_{ts} is derived.

In the very simple model shown in Fig. 2.9, the tip attached to the cantilever is treated as an effective mass m^* attached to a spring of

[2]It is noted that at the atomic length scale, the term “contact” is not well defined. In the context of NC-AFM, non-contact means without plastic deformation of tip or sample.

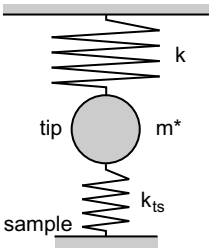

Figure 2.9: A simple model of the tip-sample interaction in FM-AFM. The tip mounted to the cantilever is modeled by a mass m^* which is attached to a spring of stiffness k. The tip-sample interaction is taken into account by an additional spring of stiffness k_{ts}. After [13].

stiffness k [13]. Then, the movement of the (unperturbed) cantilever is given by $q(t) = A\cos(2\pi f_0 t)$, and its eigenfrequency f_0 is given by:

$$f_0 = \frac{1}{2\pi}\sqrt{\frac{k}{m^*}}. \tag{2.12}$$

As shown by T. R. Albrecht et al., the influence of the tip-sample interaction can be described by an additional spring of stiffness k_{ts}, which corresponds to the force gradient experienced by the tip moving in the force field of the sample, $k_{\mathrm{ts}} = -\partial F_{\mathrm{ts}}/\partial z$ [18, 26]. For oscillation amplitudes A significantly smaller than the decay length of the tip-sample interaction, k_{ts} can be assumed to be constant during the oscillation cycle. Then, the effective stiffness becomes $k' = k + k_{\mathrm{ts}}$ and the frequency of oscillation of the cantilever becomes

$$f = \frac{1}{2\pi}\sqrt{\frac{k + k_{\mathrm{ts}}}{m^*}}. \tag{2.13}$$

That is, the movement of the tip is described by a weakly disturbed harmonic oscillator of effective stiffness k'. If the force gradient is much smaller than the stiffness of the spring, $k_{\mathrm{ts}} \ll k$, the square root in Eq. 2.13 can be approximated to lowest order by a power series of k_{ts}/k,

$$f = f_0\sqrt{1 + \frac{k_{\mathrm{ts}}}{k}} \approx f_0\left(1 + \frac{1}{2}\frac{k_{\mathrm{ts}}}{k}\right). \tag{2.14}$$

That given, the frequency shift $\Delta f = f_0 - f$ observed in FM-AFM is approximately equal to the *force gradient* at the position of the apex of the tip z above the surface plane

$$\Delta f \approx -\frac{f_0}{2k}\frac{\partial F_{\mathrm{ts}}}{\partial z}. \tag{2.15}$$

Equation 2.15 is the desired relation between frequency shift and tip-sample force. Per definition, force is the negative gradient of the interaction potential, $F = -\partial U(z)/\partial z$. The frequency shift is then directly proportional to the second derivative of the interaction potential with respect to tip-sample distance, that is

$$\Delta f \propto \frac{\partial^2 U(z)}{\partial z^2}. \tag{2.16}$$

Equation 2.15 was derived in the limit of oscillation amplitudes small compared to the decay constant of the tip-sample interaction. In our experiments, we used oscillation amplitudes of $A = 2.5$ Å or smaller, at absolute tip-sample distances of approximately $d = 15$ Å or larger. The approximation of small amplitudes is therefore expected to be well justified [27].

2.2.2. Forces in Atomic Force Microscopy

In general, the force F_{ts} can be composed of many contributions, which are assumed to act additively. The individual force contributions are e.g. chemical forces, magnetic forces, electrostatic forces and Van der Waals forces [28–30]. Here, the individual contributions relevant to the presented experiments are discussed, particularly in view of their dependence on sample bias. The relevant forces are the Van der Waals force and in particular the electrostatic force. These two force components always act attractive and are long-range in nature.

The *Van der Waals force* has its origin in the fluctuation of the electric dipole moment of an atom induced by the fluctuating moment of a second

nearby atom. Typically, the Van der Waals interaction potential u_{vdw} between two individual atoms is expressed as

$$u_{\mathrm{vdw}} = -\frac{C}{r^6}, \tag{2.17}$$

where r is the distance separating both atoms and C is a positive constant depending on the polarizability of the individual atoms [10]. As Van der Waals forces act additively, the *total* Van der Waals interaction between the tip and the sample of an AFM can be derived by integrating over all individual terms u_{vdw}. As shown by H. C. Hamaker, the interaction potential between a semi-infinite continuum (the sample) and a paraboloid (the tip) is given by

$$U_{\mathrm{vdw}} = -\frac{HR_{\mathrm{c}}}{6z}, \tag{2.18}$$

where z is the tip-sample distance and H and R_{c} are a material dependent constant and the radius of curvature of the paraboloid, respectively [10, 31]. Then, the Van der Waals force is given by

$$F_{\mathrm{vdw}} = -\frac{HR_{\mathrm{c}}}{3z^2}. \tag{2.19}$$

Hence, the Van der Waals force between tip and sample is always attractive and is long range in nature. It drops off as $1/z^2$ as opposed to the exponential drop off of the tunneling current as observed in STM. As the Van der Waals force is attractive, the corresponding frequency shift Δf of the force sensor is a negative one. Importantly, for a given tip and sample the Van der Waals force only depends on the absolute tip-sample distance and is independent of sample bias [29].

Per definition, the origin of an *electrostatic force* is an electrostatic potential difference. In STM or AFM, such potential difference arises due to the applied sample bias V. Additionally, any difference in work functions ϕ between the tip and the sample, $\Delta\phi = \phi_{\mathrm{sample}} - \phi_{\mathrm{tip}}$, causes a contact potential difference (CPD). If the tip-sample junction is considered as a capacitor, it can be attributed a capacitance $C(z)$ [11, 32]. Clearly, this capacitance depends on the geometry of the junction and

in particular on the tip-sample distance z. The electrostatic interaction potential reads

$$U_{\mathrm{el}} = -\frac{1}{2}C(z)(V - V_{\mathrm{CPD}})^2, \tag{2.20}$$

where V_{CPD} is the voltage drop due to the CPD, $V_{\mathrm{CPD}} = \Delta\phi/e$ [32, 33]. Hence, the electrostatic force that acts on the tip is given by

$$F_{\mathrm{el}} = \frac{1}{2}\frac{\partial C(z)}{\partial z}(V - V_{\mathrm{CPD}})^2 . \tag{2.21}$$

For a metallic tip and sample, the coefficient $\partial C(z)/\partial z$ does not depend on sample bias and is always *negative*, as the tip-sample capacitance decreases with increasing tip-sample distance. That is, the electrostatic force is always attractive, and the corresponding frequency shift is negative. Importantly, F_{el} has a parabolic dependence on bias voltage, $F_{\mathrm{el}} \propto -V^2$. Due to the CPD, the parabola is offset with respect to zero bias by V_{CPD}.

As an example, the tip-sample junction is modeled by an ideal plate capacitor of capacitance $C(z) = \epsilon A/z$, where ϵ is the vacuum dielectric constant and A is the surface area of the capacitor plate. Substituting $C(z)$ into Eq. 2.21, the frequency shift of the force sensor Δf can be calculated from Eq. 2.15, it reads:

$$\Delta f = -\frac{f_0}{k}\frac{\epsilon A}{z^3}(V - V_{\mathrm{CPD}})^2 . \tag{2.22}$$

From this example one sees that the electrostatic interaction is long range in nature, which is in similarity to the Van der Waals interaction. Additionally to a potential drop-off, localized charged entities such as charged adatoms present on the sample surface give rise to a electrostatic contribution to the force. For such localized charges the force interaction was shown to decay much faster with increasing tip-sample distance, typically on a length scale of 10 Å [27].

3. Gallium Arsenide and its (110) Surface

In this thesis, gallium arsenide (GaAs) has been utilized as a substrate for adsorbed molecules and as a host to buried dopant atoms. In the experiments presented in chapters 8 and 9, we have probed individual molecules adsorbed on the (110) surface of a GaAs based heterostructure from STM. In chapter 10, we present combined STM/AFM experiments probing individual shallow acceptors buried below the (110) surface of *p*-doped GaAs. Both experiments were conducted on the (110) surface of GaAs. This surface is prepared from wafer cleavage, that is, from mechanically removing the top part of a wafer. Thereby, a previously buried atomic layer is made accessible to the microscope's tip. To avoid post-cleavage contamination of the surface, cleavage is performed inside a vacuum chamber.

The relevant geometric and electronic properties of GaAs and of its (110) surface are briefly summarized in the subsequent sections. An extensive review on GaAs can be found in Refs. [34, 35].

3.1. Bulk Properties of Gallium Arsenide

Gallium arsenide is a solid compound of the group-III element gallium (Ga) and of the group-V element arsenic (As). It is a direct band gap semiconductor that crystallizes in the cubic zinc-blende structure.

In principle, all electronic and crystallographic properties of GaAs can be understood from a consideration of the bonds between the Ga and

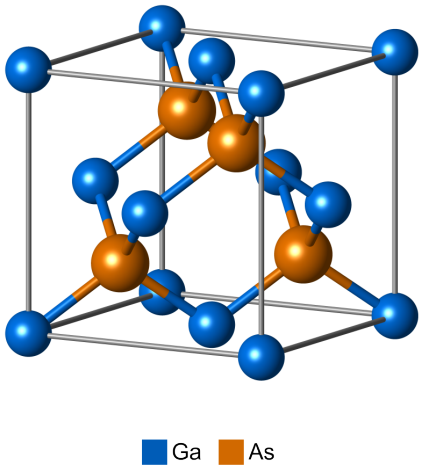

Figure 3.1: Ball-and-stick model showing the zinc-blende crystal lattice of gallium arsenide. The primitive cell is indicated by the gray sticks. Four Ga and four As atoms are each contained in the primitive cell. In a tetrahedral configuration, each As atom is bound to four neighboring Ga atoms. Vice versa, each Ga atom is tetrahedrally coordinated to four As atoms. The size of the primitive cell is $(5.65\ \text{Å})^3$.

the As atoms in solid GaAs. Neglecting closed shells, the electronic configuration of the atoms composing GaAs reads:

$$\text{Group-III element – Ga: } 4s^2 4p^1 \tag{3.1}$$

$$\text{Group-V element – As: } 4s^2 4p^3 \tag{3.2}$$

It is very important to notice that such configuration leads to a bonding which is partially covalent and partially ionic in nature. This can be seen as follows. If one electron is donated from As to Ga, both atoms can form each four singly occupied s^1p^3 hybrid orbitals. If, on the other hand, three electrons were donated from Ga to As, a pure ionic bonding can be established between Ga^{+3} and As^{-3} ions. In reality, the bonding in GaAs is neither purely covalent nor ionic, but is found to be in between these two extrema [34]. From experiment and theory, the charge transfer in the bonding of GaAs has been determined to be about one half of an electron transferred from Ga to As [36, 37].

The partially covalent nature of bonding directly relates to the zinc-blende crystal structure of GaAs shown in Fig. 3.1. In this structure, each s^1p^3 hybridized Ga atom is tetrahedrally coordinated to four As atoms, and vice versa each s^1p^3 hybridized As atom is tetrahedrally coordinated to four Ga atoms. The zinc-blende crystal structure shares

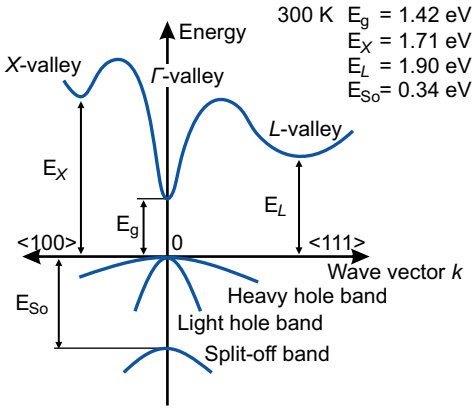

Figure 3.2: Sketch of the band structure of GaAs around the Γ ($\vec{k} = 0$) point. GaAs is a direct band gap semiconductor, both the valence band maximum and the conduction band minimum are located at the Γ point. The valence band states are four-fold degenerate at the Γ point, two times due to spin degeneracy, and two times due to the degeneracy of heavy and light hole bands. After [38].

great similarity with the diamond lattice structure, except that one half of all lattice sites is occupied by As atoms while the other half is occupied by Ga atoms. Due to this, the zinc-blende lattice structure lacks a center of inversion.

Since the valence of Ga is three and the valence of As is five, in total eight electrons contribute to the bonding in GaAs. Accordingly, the valence band of GaAs is completely occupied and the conduction band is completely empty. As valence and conduction bands are separated by a band gap of width $E_g = 1.42$ eV (room temperature value), GaAs is a semiconductor [34]. Figure 3.2 shows a sketch of the band structure of GaAs around the Γ point. The zero point of the energy scale is chosen to be equal to the maximum of the valence band, which consists of the heavy and light hole bands, the split-off band and an additional band the maximum of which is located at about -10 eV (this band is not shown in Fig. 3.2). The shortest distance between the valence band and the conduction band is referred to as the fundamental band gap E_g. Since in GaAs both the valence band maximum and the conduction band minimum are located at the Γ point, the fundamental band gap is a direct one. The width of the fundamental band gap has a slight dependence on temperature, it increases with decreasing temperature. At 5 Kelvin, the fundamental band gap width is $E_g = 1.52$ eV [34]. This and other relevant parameters of GaAs are summarized in Table 3.1.

Table 3.1: Selected properties of intrinsic GaAs. Except where stated otherwise, the values are given for a temperature of 300 K. The dielectric constant is given relative to the value of vacuum. Values taken from [34].

Parameter	GaAs
Lattice Constant (Å)	5.65
Crystal density (g/cm^3)	5.32
Molecular density ($\times 10^{22}$ cm^{-3})	2.21
Band gap (eV)	1.42
4.2 K band gap (eV)	1.52
Dielectric constant (1)	13.1

3.2. Properties of the GaAs(110) Surface

The orientation of the principle cleavage plane of GaAs is directly related to its zinc-blende lattice structure and the partially ionic character of bonding in GaAs. Usually, the principle cleavage plane of a brittle solid is the one for which the smallest number of bonds per unit area have to be severed by the cleavage process[1]. For the zinc-blende crystal structure, this surface is the {111} surface. In GaAs, there exist two different types of {111} surfaces, which are either composed of only Ga atoms or of only As atoms, respectively. Due to the partial ionic character of bonding in GaAs, these surfaces are polar and therefore have a large surface energy. This makes them unfavorable as the principle cleavage planes. The {110} surfaces of GaAs on the other hand are composed of an equal number of Ga and As atoms each, and therefore these surfaces carry no net charge. Consequently, the {110} surfaces are the principle cleavage planes of GaAs [34]. Note that for the pure covalently bound semiconductor silicon, the principle cleavage plane is indeed the {111} surface.

After cleavage, the GaAs{110} surface undergoes a 1×1 relaxation. That is, the {110} surface has the same periodicity as the truncated bulk structure, but the atomic positions perpendicular to the {110} plane are shifted with respect to the bulk atomic positions. The relaxation

[1] Strictly speaking, the principle cleavage plane is defined by the surface energy necessary to separate a crystal along a certain plane.

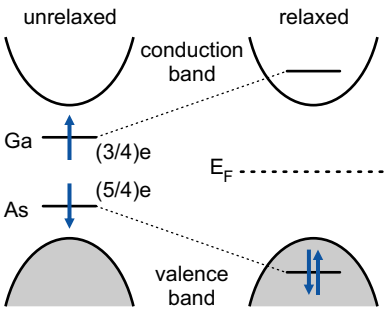

Figure 3.3: Schematic energy diagram of the relaxation of GaAs(110). For the unrelaxed surface, partially occupied dangling hybrid states are present in the band gap. The numbers give the partial occupation as fraction of the elementary charge. The relaxation shifts the dangling hybrid states beyond the valence and conduction band edges, the full band gap width of bulk GaAs is restored. After [39].

can be understood as follows. Prior to the relaxation (that is, for the truncated bulk geometry), s^1p^3 hybridized Ga and As surface atoms are 3-fold coordinated to other surface atoms, while the fourth bond has been severed. It sticks out into vacuum as a partially occupied dangling hybrid. Due to their partial occupation, the energy levels of the dangling hybrids are located within the fundamental band gap. As the electronegativities of Ga (1.81 after Pauling [40]) and As (2.18) differ from each other, the Ga and As dangling hybrids are non-degenerate. As shown in Fig. 3.3 the dangling hybrid of Ga is higher in energy as the one of As. The energy of the surface is then lowered by transfer of the electronic charge from the Ga dangling hybrid to the As dangling hybrid, which becomes doubly occupied [39]. Due to this change in occupation, the energy of the surface can even be further lowered by a rehybridization of the surface Ga and As atoms. The energy of the doubly occupied As dangling hybrid is lowered by an enhancement of its s-like character (note that an s orbital is located lower in energy than an s^1p^3 hybrid orbital). In turn, the three As bonding hybrids have to enhance their p-like character. Consequently, the bonding angle between surface As and its three surrounding Ga atoms shifts from the tetrahedral angle of 109.5° closer to a value of 90°, which is the angle between orthogonal p-orbitals. By the same token, the Ga atom enhances the p-like character of its unoccupied dangling hybrid and the s-like character of its bonding hybrids. The latter is due to rehybridization of surface Ga from s^1p^3 to s^1p^2. The bonding hybrids are then in an almost planar geometry, and the unoccupied p orbital sticks out into vacuum

as a dangling bond [39]. As the bonding angles change, the atomic positions of the surface atoms parallel to the (110) surface plane have to relax. Relative to the (110) surface plane, Ga atoms move outward and As atoms move inward. This relaxation is described by a surface buckling angle $\omega \approx 27°$ [41–43] indicated in Fig. 3.4b.

The geometry of the {110} surfaces and the effect of the surface relaxation is shown in Fig. 3.4. As the zinc-blende lattice lacks a center of inversion, two distinguishable {110} surfaces exist. These are the (110) and the $(\bar{1}10)$ surfaces. While these two surfaces are identical from stoichiometry, they are distinct by the sequential arrangement of As and Ga atoms in the crystallographic [001] direction, see Fig. 3.4a. For the (110) surface the arrangement is Ga–As–Ga, while for the $(\bar{1}10)$ it is As–Ga–As. Perpendicular to the [001] direction, As and Ga atoms are arranged in zig-zag rows. In between these zig-zag rows, the atoms of the first layer subsurface are visible. As the {110} surface is relaxed rather than reconstructed, the dimension of the surface unit cell equals the one of the truncated bulk structure. The surface unit cell has a size of 4.0×5.65 Å^2 and contains one As and one Ga atom each. The effect of the surface relaxation is shown in Fig. 3.4b. As mentioned above, Ga atoms are almost in a planar bonding geometry in the relaxed surface. For the experiments described in this thesis, only the (110) surface was utilized.

As mentioned above, the effect of the surface relaxation is to shift the dangling hybrid states beyond valence and conduction band edges. Consequently, there are no electronic states present within the fundamental band gap on GaAs(110), and accordingly no electronic surface states exist [45]. As shown by Ph. Ebert et al., the electronic structure of GaAs(110) is largely dominated by *surface resonances* [44]. Figure 3.5 shows a sketch of the calculated density of states of the (110) surface of a III-V semiconductor. Within the energy interval accessible to STM, four surface resonances are located, labeled $A4$, $A5$, $C3$ and $C4$. The lateral periodicity of these surface resonances is the same as for the geometry of the GaAs(110) surface. However, the resonances labeled A are preferentially located atop the *anionic* species (As), while the surface resonances

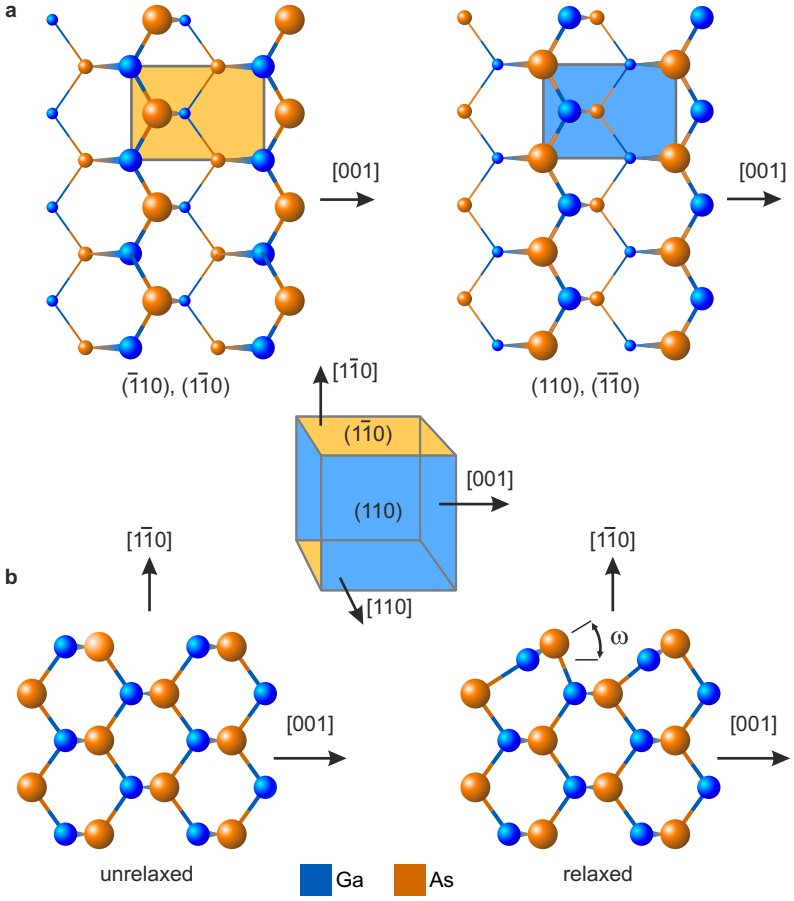

Figure 3.4: Ball-and-stick model of the GaAs{110} surface. **a**, Top view, showing the two distinct subsets of $\{110\}$ surfaces, which have identical stoichiometry but are distinct by the sequential arrangement of Ga and As atoms in the crystallographic $[001]$ direction. Larger spheres indicate the surface layer atoms, smaller spheres indicate the atoms of the first layer subsurface. The colored rectangles indicate a surface unit cell. Crystallographic directions are given by the colored cube shown in the center. After [12]. **b**, Side view, showing the effect of the 1×1 surface relaxation. Relative to the $\{110\}$ plane, the As atoms move outward and the Ga atoms move inward by an angle of $\omega \approx 27^{\circ}$.

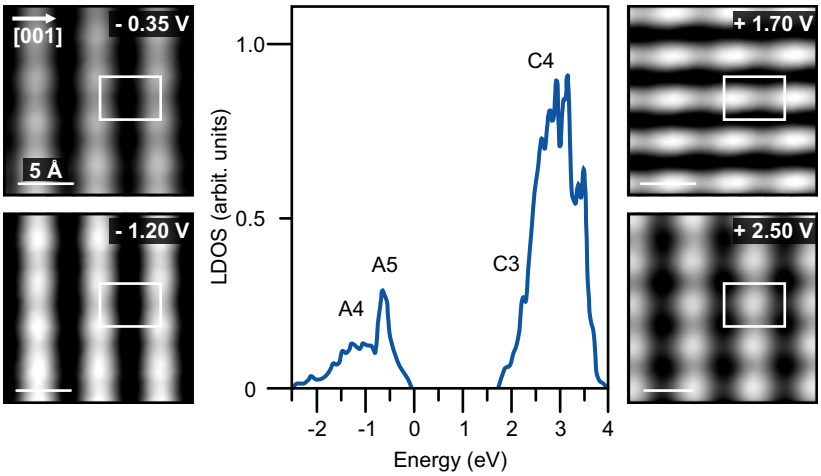

Figure 3.5: The surface resonances of GaAs(110). Center: Sketch of the density of states of the (110) surface of a III-V semiconductor for energies around the fundamental band gap (after Ref. [44]). The origin of the energy scale is arbitrarily positioned at the top of the valence band, which corresponds to a p-type doped sample. Four surface resonances labeled $A4$, $A5$, $C3$, and $C4$ are present within the energy interval shown. Left and right: Bias-dependent STM topographies of the (110) surface of p-type doped GaAs ($I = 20$ pA, bias voltages as indicated). A surface unit-cell (4.0×5.6 Å^2) is indicated in each topography. The corrugation of GaAs(110) shows a strong dependence on bias voltage, it depends on the surface resonances contributing to tunneling.

labeled C are preferentially located atop the *cationic* species (Ga) [44]. Due to this, the corrugation observed in STM images of GaAs(110) has a strong dependence on sample bias, which was experimentally first observed by R. Feenstra et al. [42]. For negative sample biases, the tunneling current is due to tunneling of electrons from the occupied $A4$ and $A5$ resonances into empty states of the tip. For these sample biases, corrugation runs along the [001] crystallographic direction, and the maxima of corrugation are expected to be atop the As atoms. For a positive sample bias of about +1.7 V, for which electrons tunnel from occupied tip states into the unoccupied $C3$ surface resonance, the corrugation runs perpendicular to the [001] direction (see Fig. 3.5). For a higher positive sample

bias at which the tunneling current is dominated by electrons tunneling into the empty $C4$ surface resonance, the corrugation is *rotated* by 90° and again is along the [001] direction. For positive bias voltages, the maxima in corrugation are expected to be mainly atop the Ga atoms. In chapter 8, we used this chemical sensitivity of STM to determine the adsorption site of individual molecules deposited on GaAs(110).

The lack of surface states on GaAs(110) has profound consequences for STM experiments [12]. First, there exists an energy interval of zero density of states at the GaAs(110) surface (the band gap). Consequently, no tunneling current can be drawn for sample biases at which the Fermi level of the tip is located inside this band gap, see Fig. 2.8. Second, zero or only a small density of electronic states is present at the Fermi level of the sample. Hence, electric fields are not screened from the (110) surface, which allows the STM to catch up the electronic signatures of defects such as dopant atoms *buried* below the (110) surface layer [7, 46]. However, by the same token the electrostatic field that emanates from the probe tip is not screened, it partially penetrates into the interior of the sample where it shifts the electronic positions of all states present below the tip. This effect, known as tip-induced band bending, can severely influence experimental data, as is in detail discussed in the next chapter.

4. Tip-Induced Band Bending

In SPM experiments on semiconductors, the presence of the microscope's tip in front of the semiconducting surface can severely influence experimental data. This is due to the penetration of the electrostatic potential between tip and sample into the interior of the sample. In a semiclassical approximation, this potential drop inside the sample will bend the bands of the semiconductor at its surface, as it is illustrated in Fig. 4.1. Therefore, this effect is referred to as "tip-induced band bending" (TIBB). As the size and polarity of TIBB depends on a number of parameters like the tips work function that are *a priori* unknown in STM, it can be a severe impediment even to the qualitative interpretation of experimental data, as was realized by R. Feenstra and co-workers [8, 47–50] already

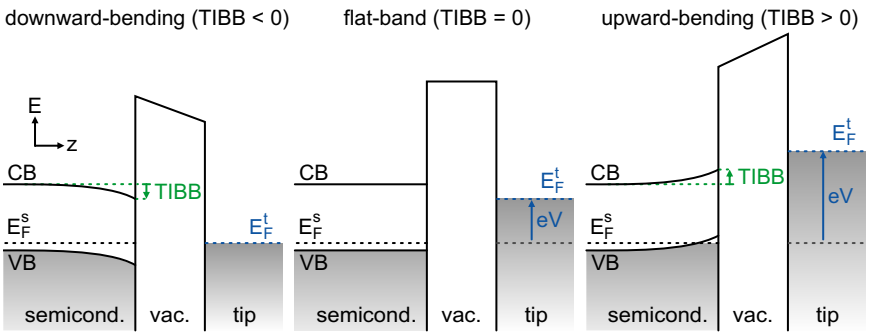

Figure 4.1: Different regimes of tip-induced band bending. Depending on the sample bias taken with respect to the contact potential difference, the bands at the semiconductors surface are either bent downward (left) or are flat (center) or are bent upward, respectively (right). On p-type GaAs, for downward (upward) band bending electrons (holes) will accumulate below the tip of the SPM. After [12].

shortly after the invention of the STM. The effect of TIBB and its consequences have been addressed in many publications and are summarized in the following [9, 12, 49, 51, 52].

In general, the total potential drop ϕ_{T} between the microscope's tip and the sample is due the applied sample bias, eV, plus the *contact potential difference* (CPD), $\Delta\phi$. The latter arises from the different work functions of tip and sample, respectively. Hence,

$$\phi_T = eV + \Delta\phi \qquad \text{with} \qquad \Delta\phi = \phi_{\mathrm{sample}} - \phi_{\mathrm{tip}}. \tag{4.1}$$

For a metallic tip and sample, this potential drops off almost entirely in the vacuum gap. This is due to the large number of mobile charge carriers in a metal, which results in an extreme short value for the (Thomas-Fermi) screening-length of an electric field of below 1 Å [12, 35]. For a GaAs sample however, the screening is much less effective. As discussed in Sec. 3.2, no surface states are present at the (110) surface of the GaAs crystal, and the density of states at the sample's Fermi level (and hence the screening-length) is determined by the local concentration of dopant atoms. Even for a very high dopant concentration, the density of states at the Fermi level (and hence the number of mobile charge carriers) is much lower than the one of a metal. Accordingly, an appreciable fraction of the total potential will drop inside the surface region of the semiconductor. This potential drop shifts the positions of all electronic states present beneath the microscope's tip.

Depending on the polarity of the total potential ϕ_{T}, different band bending regimes can be identified. Three regimes most import to the experiment are described in the following. If ϕ_{T} is negative, the bands will be bent downward as it is illustrated in Fig. 4.1, left panel. Consequently, the distance between the conduction band minimum (valence band maximum) and the sample's Fermi level is locally lowered (increased). Hence, at the surface of the sample electrons (holes) are accumulated (depleted). By the same token, holes (electrons) are accumulated (depleted) below the microscope's tip for a positive value of ϕ_{T}, at which the bands bend upwards. This situation is illustrated in Fig. 4.1, right panel. At a sample

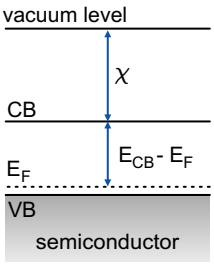

Figure 4.2: The work function of a semiconductor is given by the difference between Fermi level and conduction band minimum, $E_{\mathrm{CB}} - E_{\mathrm{F}}$, which is a bulk property, and by the electron affinity χ, which is specific to the surface orientation.

bias exactly canceling out the difference in work functions, $eV = -\Delta\phi$, the total electrostatic potential between tip and sample is zero, $\phi_{\mathrm{T}} = 0$. In this situation, there is no potential to penetrate the semiconductor and the bands are flat, TIBB = 0 (Fig. 4.1, middle panel). The corresponding sample bias is referred to as *flat-band voltage* V_{CPD}.

As discussed above, the sample bias with respect to the CPD determines the band bending regime (downwards, flat-band or upwards). The CPD arises from the difference in work functions between tip and sample. The work function is not only determined by bulk properties but strongly depends on the surface orientation, roughness and cleanliness. Usually, the work function is well known for a low indexed, clean surface. Such is the GaAs(110) surface produced by cleavage in ultrahigh vacuum. Its work function is the difference in energy between the Fermi level and the conduction band minimum, which is a property of the bulk, plus the electron affinity χ, which is specific to the surface orientation (see Fig. 4.2):

$$\phi_{\mathrm{GaAs(110)}} = (E_{\mathrm{CB}} - E_{\mathrm{F}}) + \chi_{\mathrm{GaAs(110)}}. \tag{4.2}$$

For a given dopant concentration, $E_{\mathrm{CB}} - E_{\mathrm{F}}$ is well known, and the electron affinity of clean GaAs(110) is [35]:

$$\chi_{\mathrm{GaAs(110)}} = 4.07 \text{ eV}. \tag{4.3}$$

For the work function of the micoscope's tip, however, the situation is different. The tips used for the experiments described in this thesis are cut from polycrystalline (90/10) Platinum-Iridium-alloy (Pt/Ir) wires. The work function of polycrystalline Pt/Ir is about 5.5 eV [10]. The

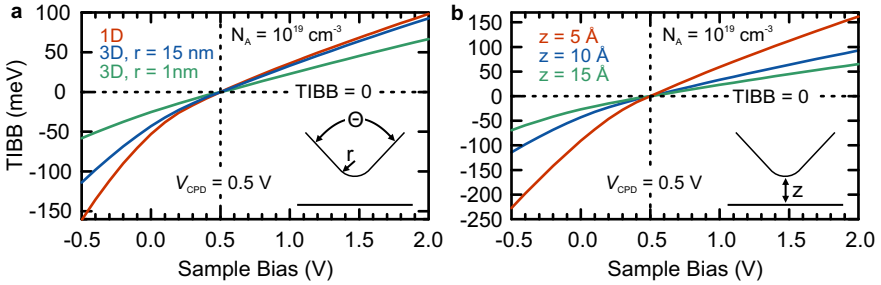

Figure 4.3: Calculated value of the band bending at the semiconductors surface as a function of the sample bias V, TIBB(V), for various different geometric parameters (see insets). **a**, Variation of the probe tip's radius of curvature r, for a fixed shank angle θ of 120° and a fixed tip-sample distance z of 10 Å. For comparison, the result of a one-dimensional calculation is shown. **b**, Variation of the tip-sample distance z at fixed values of θ and r of 120° and 15 nm, respectively. For all calculations, the CPD has been chosen to be -0.5 eV and the acceptor density was 1×10^{19} cm^{-3}.

tips are prepared by repeated indentations into a clean Cu surface. Such method most likely results in tip apices covered by copper. For clean Cu surfaces, the work functions varies from 5.1 eV for a (100) oriented surface to 4.5 eV for a (112) oriented one [40], to 4.4 eV for polycrystalline Cu [53]. Further, it is well known that the work function of high indexed surfaces can be drastically decreased as compared to low indexed ones [52, 54, 55]. Certainly the surface of the microscope's tip is composed of several different high-indexed facets of unknown crystallographic orientations of either Cu or Pt/Ir. Hence the work function of the tip is *a priori* unknown and can only be assumed to be within a reasonable range from 3-6 eV. Further, the work-function of the tip will be different for each individual tip apex, as the apex's geometry is changed by the controlled indentation into the Cu crystal during tip preparation. Accordingly, the CPD is unknown, and its uncertainty is of the same order as the applied sample bias. Thus, within the relevant bias range, the *polarity* of TIBB is unknown.

Neglecting quantum mechanical effects, the *magnitude* of TIBB can be

calculated by solving the Poisson equation of the corresponding problem of a metal tip in close vicinity to a (biased) semiconductor. This problem is an analogy to a Schottky contact, except for the vacuum gap [56]. While some input parameters of the calculation such as the dopant density and the dielectric constant of the sample are known with high accuracy, the calculation also requires the geometry of the junction, which can only be estimated. If the tip is idealized and modeled by a cone with a spherical tip apex, the geometric parameters of the junction are the tips radius of curvature r, its shank angle θ, and the absolute tip-sample distance z. These quantities are defined in the insets of Fig. 4.3, which shows calculated values for TIBB(V) for various different geometric parameters. The calculations have been performed using a Poisson-equation solver developed by R. M. Feenstra [49, 57]. As input parameters we have chosen a zinc acceptor concentration of $N_\mathrm{A} = 1 \times 10^{19}$ cm^{-3}, a flat-band voltage of $V_\mathrm{CPD} = 0.5$ V, and a temperature of 5 K. The quantity plotted [TIBB(V)] is the band bending at the semiconductors surface at a position directly opposite the microscope's tip. The general features that can be inferred from Fig. 4.3 are the following. TIBB(V) is a monotonic function of the applied sample bias, shifted with respect to zero by the CPD. Further, the slope of TIBB(V) is shallower for $V > V_\mathrm{CPD}$ than for $V < V_\mathrm{CPD}$. The latter is a consequence of the assumed p-type doping. On p-type samples, the screening is more effective for sample biases exceeding V_CPD, at which the bands are bent upwards. As the Fermi level is just above the valence band edge on p-type samples, even a small TIBB is associated with large DOS being dragged across the Fermi level. For downward band bending, only the relatively small DOS of a (dopant induced) impurity band itself is dragged across the Fermi level, as the conduction band is separated from the Fermi level by almost the entire band gap.

Figure 4.3a shows TIBB(V) for different values of the tip's radius of curvature r. The calculations have been performed for a very small tip apex of $r = 1$ nm and for a reasonable value of $r = 15$ nm. For comparison, the results of a one-dimensional calculation are also shown (for both the one- and the three-dimensional calculation an identical tip-sample distance of $z = 10$ Å has been used). As can be seen, the

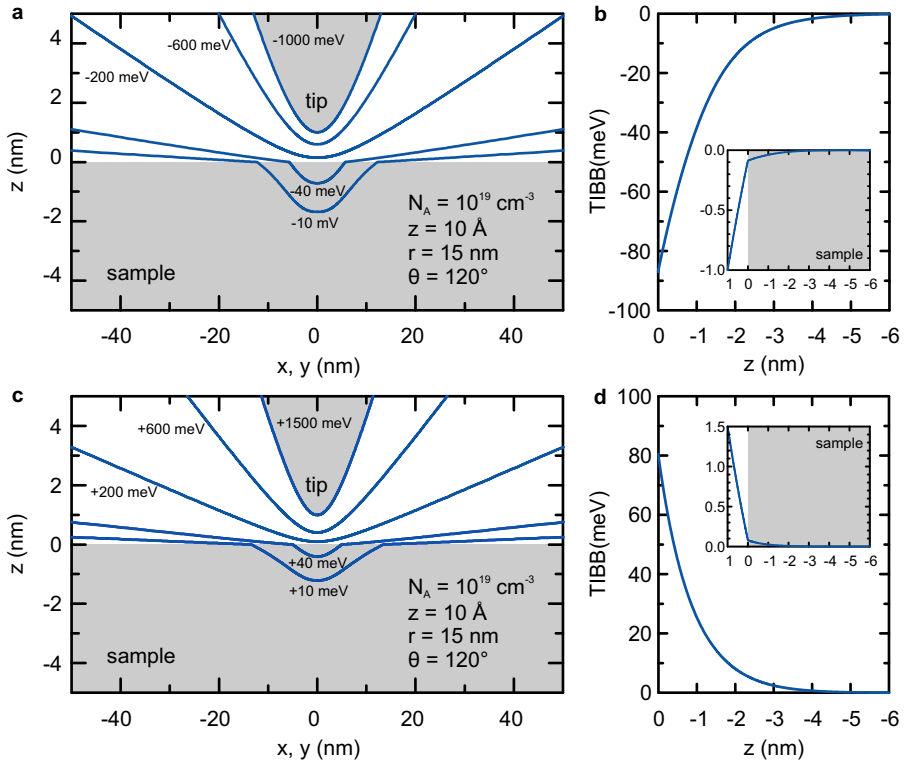

Figure 4.4: **a** and **c**, Potential energy profiles between a biased probe tip and a semiconductor for a total potential $\phi_{\mathrm{T}} = eV + \Delta\phi$ of -1.0 eV (a) and $+1.5$ eV (c). Dopant density and geometric parameters are as specified in the figures. **b**, and **d**: TIBB(z) for $x, y = 0$ corresponding to (a) and (c). The insets also show the potential drop-off inside the vacuum gap separating tip and sample. After Ref. [58].

smaller the tip's radius of curvature, the smaller the magnitude of TIBB is. Figure 4.3b shows TIBB(V) for different values of the absolute tip-sample distance z; for a very small value of 5 Å, a reasonable value of 10 Å and finally a rather large value of 15 Å. As it is expected, TIBB effects are more pronounced for short tip-sample distances (clearly, for an infinite tip-sample distance the potential would entirely drop-off inside the vacuum gap only).

For reasonable geometric parameters, Figs. 4.4a and 4.4c show potential energy profiles. The parameters of the semiconductor are identical to those of Fig. 4.3. The surface plane is located at $z = 0$ and the semiconductor is located in the half-space of negative z. The shortest tip-sample distance is 10 Å. For the calculations the total potential $\phi_{\mathrm{T}} = eV + \Delta\phi$ has been chosen to be -1.0 eV (Fig. 4.4a) and $+1.5$ eV (Fig. 4.4c), respectively. Figures 4.4b and 4.4d show the potential profile along the z axis at a position directly opposite the tip (that is, for $x, y = 0$). As can be seen, for the high concentration of acceptors in the sample and for the geometric parameters and potentials chosen, the penetration of the electrostatic field is of about 20 nm in the lateral direction and of about 3 nm in the vertical direction.

The above is summarized as follows. In a semiclassical approximation, the band bending shifts the position of any electronic state of energy E located at the position $\vec{r}$ beneath the microscope's tip by an amount $\mathrm{TIBB}(V, \vec{r})$. The polarity of the band bending is determined by the CPD between tip and sample. The magnitude of TIBB depends on the geometry of the tip's apex; TIBB effects are more pronounced for a blunt tip apex as well as for short tip-sample distances.

For scanning tunneling spectroscopy, the important consequence of TIBB is the following. Due to TIBB, the relation between the energy at which a particular state (located at the surface of the sample) is observed in STM changes from $E - E_{\mathrm{F}} = eV$ to

$$E - E_{\mathrm{F}} = eV - \mathrm{TIBB}(V). \tag{4.4}$$

Exemplary, Fig. 4.5 depicts the TIBB-shift of the onset of tunneling into empty conduction band states. As in STM neither the CPD nor the tip's geometry are known, due to TIBB the energy scale within the tunneling junction is unknown.

In particular, the lack of an exact value for the CPD turns out to be a severe impediment to the interpretation of experimental data [9]. As the CPD determines the polarity of the band bending, it determines if any

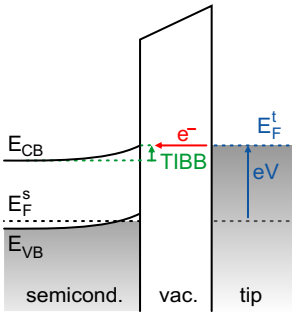

Figure 4.5: The influence of tip-induced band bending on tunneling spectroscopy. Without TIBB, the onset of tunneling of electrons from occupied states of the tip into empty states of the conduction band occurs for a bias voltage corresponding to $eV = E_{\mathrm{CB}} - E_{\mathrm{F}}^{\mathrm{s}}$. In the presence of TIBB, a larger sample bias is necessary, which corresponds to $eV = E_{\mathrm{CB}} - E_{\mathrm{F}}^{\mathrm{s}} + \mathrm{TIBB}$.

electronic state close the Fermi level E_{F} of the sample is TIBB-shifted across E_{F}, which, in turn, determines the permanent occupation of this particular state. Without knowledge of its occupation, however, it is a priori unknown if this state can contribute to the tunneling current, which is the main topic of chapter 10.

As an indirect measure on the tip's work function, many researchers have exploited the tip-sample distance dependence of the tunneling current from $I(z)$ spectroscopy in STM. This method will be discussed in detail in appendix A. Importantly, this indirect method has been shown to only provide a very qualitative measure for CPD with variations on the order of 1 eV. In AFM, however, there exists a direct and straight forward method to extract the CPD, which is Kelvin probe force spectroscopy. This method is presented in the next chapter.

5. Kelvin Probe Force Spectroscopy

Kelvin probe force spectroscopy (KPFS) is an AFM-based technique that allows a direct measurement of the contact potential difference between the microscope's tip and the surface of the sample [32]. The electrostatic potential $\phi_{\mathrm{T}} = eV + \Delta\phi$ between the tip and the surface of the sample gives rise to an electrostatic force that acts on the AFM tip. In KPFS, one nullifies this component of the force by application of a *dc* sample bias. As the *dc* sample bias cancels out the difference in work function, $V_{\mathrm{CPD}} = -\Delta\phi/e$, the electrostatic field in the vacuum gap between tip and sample becomes zero and the electrostatic component of the force vanishes.

After a brief historical review, the basic principle of KPFS is discussed by considering a metallic tip and a metallic sample. After this, KPFS on semiconducting samples is considered.

The Kelvin probe method originates back to Lord Kelvin, who in 1897 nullified the *ac* current induced by the distance-oscillation of parallel plates made from different metals by application of an appropriate *dc* voltage. As the *dc* voltage cancels out the difference in work function between the metals, the total electrostatic field between the parallel plates becomes zero and no current is induced [32, 59]. The Kelvin probe method was first combined with AFM by M. Nonnenmacher et al. in 1991 [60]. In KPFS, the electrostatic force acting on the AFM tip is measured instead of an *ac* current as used in the original Kelvin probe method.

5.1. KPFS on a Metal

The concept of KPFS is illustrated in Fig. 5.1. For a metallic tip and a metallic sample far apart from each other and not in electrical contact with each other, the vacuum levels E_{vac} will be aligned. Due to the contact potential difference $\Delta\phi$, the Fermi levels in tip and sample are at different positions, see Fig. 5.1a. Once tip and sample are electrically connected by a voltage source, electrons will flow from the material of lower work function into the material of higher work function until the Fermi levels in tip and sample are aligned, see Fig. 5.1b. The CPD then drops off within the vacuum gap and causes an electrostatic force acting between tip and sample. In AFM, this force can be detected. A *dc* sample bias is now applied to minimize this component of the force. As the *dc* sample bias cancels out the contact potential difference, $V_{\mathrm{CPD}} = -\Delta\phi/e$, the electrostatic field between tip and sample becomes

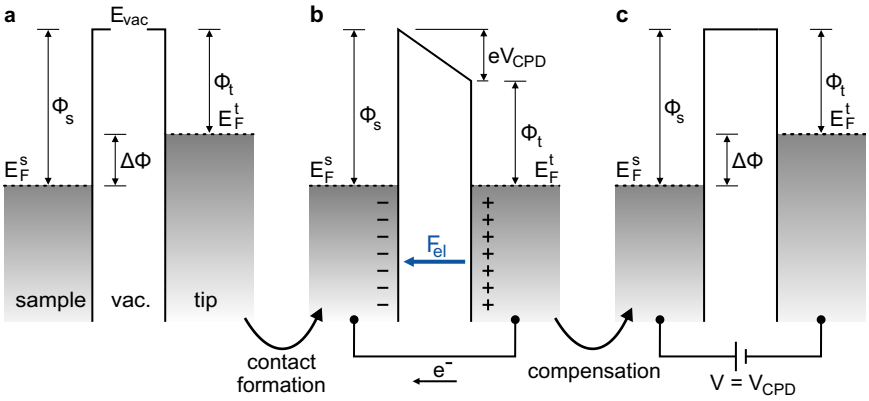

Figure 5.1: The principle of Kelvin Probe Force Spectroscopy. **a**, Energy levels of a metallic tip and a metallic sample which are not electrically connected to each other. **b**, After contact formation, electrons flow from the tip (lower work function material) into the sample (higher work function material) until the Fermi levels are aligned. The contact potential difference $\Delta\phi$ drops off in the vacuum gap; tip and sample electrostatically attract each other. **c**, A *dc* bias is applied to nullify the electrostatic force. After [11].

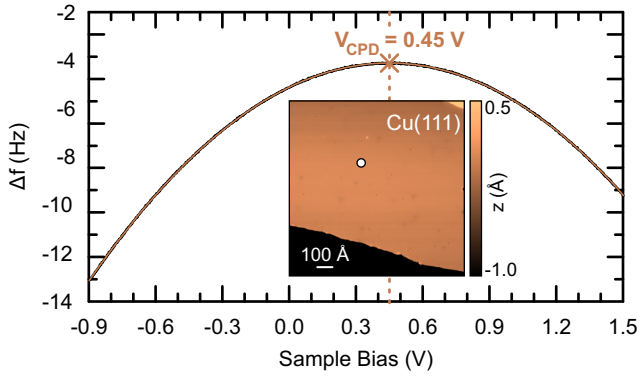

Figure 5.2: Kelvin probe force spectroscopy on bare Cu(111). At a fixed tip position (as indicated in the inset STM image taken at $V = +50$ mV, $I = 2.5$ pA), the frequency shift of the force sensor $\Delta f(V)$ is recorded as a function of the *dc* sample bias V (black line). The peak of the parabolic fit to the data (colored line) directly corresponds to the contact potential difference.

zero and the electrostatic force vanishes (Fig. 5.1c) [32, 33].

As seen from equations 2.15 and 2.21, the frequency shift of the force sensor $\Delta f(V)$ at a fixed tip-sample distance z due to an electrostatic force is:

$$\Delta f(V) = -\frac{1}{2}\frac{\partial^2 C(z)}{\partial z^2}(V - V_{\mathrm{CPD}})^2 \tag{5.1}$$

where $\partial^2 C(z)/\partial z^2$ is the second derivative of the tip-sample capacitance $C(z)$ with respect to the absolute tip-sample distance z. Hence, the frequency shift due to an electrostatic force is expected to be of parabolic shape, and to be minimal for $V = V_{\mathrm{CPD}} = -\Delta\phi/e$. Accordingly, the peak of the $\Delta f(V)$ parabola directly corresponds to a compensated contact potential difference $\Delta\phi$.

Figure 5.2 shows a KPFS measurement on a clean Cu(111) surface. For the data shown here, the tip was retracted by 5 Å once the feedback loop of the STM was interrupted at a setpoint of $V = +50$ mV, $I = 2.5$ pA. With the tip position fixed, the frequency shift of the force sensor has been recorded as the *dc* sample bias was ramped. As expected, $\Delta f(V)$

is a parabola offset with respect to zero bias. For this particular tip apex, $\Delta f(V)$ and hence the electrostatic force acting on the sensor is minimized for a sample bias of $V = 0.45$ V. Hence, the CPD between the Cu(111) surface and this particular tip apex is 0.45 eV. As the work function of clean Cu(111) is well known to be 4.94 eV [40], Eq. 4.1 yields a work function of $(4.94 - 0.45)$ eV $= 4.49$ eV for the microscope's tip. This value is in the possible range of 3-6 eV discussed in chapter 4. Note that for compensated CPD $\Delta f(V)$ is non-zero, but is negative. For this particular tip apex, one finds $\Delta f(V_{\mathrm{CPD}}) = -3.3$ Hz. That is, even for compensated CPD a residual attractive force acts on the sensor. The latter is due to other force contributions between tip and sample, which may be due to localized charges or Van der Waals attraction.

5.2. KPFS on a Semiconductor

When KPFS is performed on semiconductors, two effects not present on metallic surfaces have to be taken into account. The first effect concerns the tip-sample capacitance C, which may change due to TIBB. This effect is of purely electrostatic origin. The second effect concerns an ohmic voltage drop inside the sample due to a tunneling current. Both effects are discussed in the following.

Voltage Dependence of the Tip-Sample Capacitance

For a metallic tip and sample, the junction capacitance is independent of the applied bias voltage, it only depends on the tip-sample distance, $C(z)$. Hence $\partial^2 C(z)/\partial z^2$ is constant for a fixed value of z. For a semiconducting sample, however, the capacitance may change with sample bias, $C(z, V)$ [61, 62]. As discussed in chapter 4, in a semiconductor the screening of an electrostatic potential is much less effective than in a metal; the potential penetrates into the interior of the semiconductor where it bends the bands. Hence, the electrostatic potential drops not only in the vacuum gap of width z but also inside the sample across a screening-length s (Fig. 5.3). The latter depends in a non-trivial man-

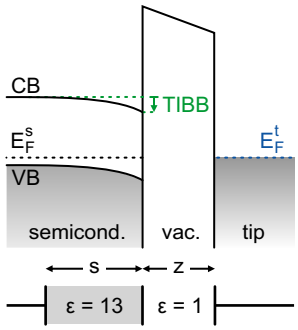

Figure 5.3: In the presence of tip-induced band bending, the electrostatic potential between tip and sample drops off not only in the vacuum gap of width z but also inside the semiconductor across the screening length s. The total tip-sample capacitance is modeled by two plate capacitors connected in series, having relative dielectric constants of $\epsilon = 1$ (vacuum gap) and $\epsilon = 13$ (GaAs).

ner on the sample bias V and on the absolute tip-sample distance z, $s = s(z, V)$. Due to this, the tip-sample capacitance depends on the sample bias.

To qualitatively describe this effect, the following two assumption are made: First, it is assumed that the tunneling junction can be described by a one-dimensional model. Second, it is assumed that the accumulated (or depleted) charge carriers that screen the potential are not distributed within the screening length s, but are entirely located within a plane parallel to the surface. This plane is separated from the surface by the screening length s. That given, the potential drops off linearly within the sample and the tip-sample capacitance can be modeled as two plate capacitors connected in series as illustrated in Fig. 5.3. The first capacitor is the metallic tip separated by a distance z from the surface plane of the sample. The second capacitor is the surface plane of the sample separated by the screening length s from a plain inside the sample, at which the electrostatic potential has dropped off to zero. The relative dielectric constants of vacuum and GaAs are 1 and 13, respectively [35]. In this model, the total capacity of the tip-sample junction is given by [62]:

$$C(z, V) = \frac{\epsilon\epsilon_0 A}{s(z, V) + \epsilon z} \tag{5.2}$$

where A is the surface area of the capacitor plates and ϵ_0 and ϵ are the absolute and relative dielectric constants of vacuum and of GaAs, respectively. That is, the curvature of $\Delta f(V)$, $\partial^2 C(z, V)/\partial z^2$, may itself depend on V, giving rise to a non-parabolic shape of $\Delta f(V)$.

Most importantly in the context of this thesis, this effect changes only the shape of $\Delta f(V)$, but it does *not* influence its peak position, which still corresponds to the CPD. Hence, the determination of the CPD from KPFS on semiconductors is not affected by this effect. Note that for compensated CPD, $V_{\mathrm{CPD}} = -\Delta\phi/e$, the total electrostatic field within the junction is zero. In this situation there is no band bending and the screening length s becomes zero.

The bias dependence of the tip-sample capacitance $C(z, V)$ is expected to decrease for increasing tip-sample distances [61, 62], as the magnitude of TIBB decreases. Accordingly, the shape of $\Delta f(V)$ is expected to converge to a perfect parabola for large tip-sample distances.

Current-Induced Voltage Drop

As recently shown by Weymouth et al. [63, 64], KPFS measurements on semiconductors can be influenced if simultaneously to recording $\Delta f(V)$ a tunneling current is injected into the sample. As the electric conductance of a semiconductor may be poor compared to the one of a metal, current flow may result in a considerable ohmic voltage drop *inside* the semiconducting sample. Such ohmic voltage drop will increase with increasing tunneling current. Similar to TIBB, this ohmic voltage drop reduces the total potential drop-off between the microscope's tip and the surface of the semiconductor.

As illustrated in Fig. 5.4, ohmic effects can be modeled by treating the tunneling junction as two resistors R connected in series [64]. The first resistance is the one of the tunneling junction, R_{t}, and the second one is the resistance of the sample, R_{s}. In this model, TIBB is neglected as the sample is simply treated as an ohmic resistor. Hence, at zero bias the voltage corresponding to the CPD, V_{CPD}, drops off entirely within the vacuum gap. Any applied sample bias V causes a current I through the junction. Accordingly, the voltage drop between the tip and the surface

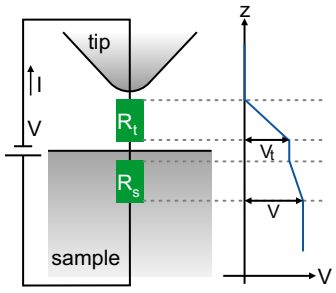

Figure 5.4: The tunneling junction is modeled by two ohmic resistors connected in series. The bias voltage V is split into to two parts. Between the tip and the sample surface, a fraction of $V_t < V$ drops off across the tunneling gap of resistance R_t. A small fraction of the bias drops off inside the sample across a resistance R_s. After [64].

of the sample, V_t, is given by [64]:

$$\begin{aligned} V_t &= V_{CPD} + R_t I \\ &= V_{CPD} + V \frac{R_t}{R_t + R_s}. \end{aligned} \tag{5.3}$$

In KPFS, one nullifies the electrostatic force that acts on the AFM tip by nullifying the total electrostatic potential between the tip and the surface of the sample $\phi_T = eV_t$. Hence, demanding $V_t = 0$ in Eq. 5.3, we see that

$$V = -V_{CPD} \frac{R_t}{R_s + R_t} \neq V_{CPD}. \tag{5.4}$$

That is, the sample bias at which the electrostatic force acting on the AFM tip is nullified is no longer V_{CPD}, but V_{CPD} times the ratio between the respective resistances of tunneling junction and sample. In general, these resistances are unknown. Hence, the peak of the KPFS parabola does not correspond to the contact potential difference, and the CPD can *not* be extracted from KPFS if ohmic effects are present. A more elaborate treatment of the ohmic effect discussed here shows that additionally to a shift of the peak of the parabola also its curvature may be changed [64].

Ohmic effects can easily be avoided, if the KPFS data are acquired at tip-sample distances large enough for the tunneling current to be zero (or, equivalently, for which $R_t \gg R_s$). In this work, KPFS has been combined with STS measurements on the GaAs(110) surface. From the

KPFS data, the CPD and hence the flat-band voltage was determined. These experiments are presented in chapter 10. For these experiments, the knowledge of the CPD is the key to the correct interpretation of the experimental data. All related KPFS data have been acquired at large tip-sample distances at which the tunneling current was zero for all sample biases. Hence, both the electrostatic effect and the ohmic effect are negligible.

5.3. Errors in KPFS

In this section, possible contributions to the experimental uncertainty of KPFS are discussed which may arise due to an inhomogeneous tip apex.

In general, KPFS measurements can be subject to averaging effects, if areas of different work function contribute to the measurement [32, 65]. Since the GaAs samples discussed in chapter 10 are atomically flat and

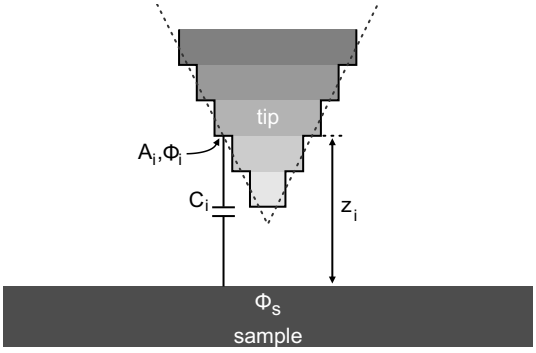

Figure 5.5: The staircase model of the microscope's tip. In this model, the tip is assumed to consist of a series of parallel plate capacitors C_i at distances z_i from the surface. Each capacitor plate has a surface area A_i and a work function ϕ_i. Image adapted from [32].

homogeneous, such effects can arise only if the work function of the tip is spatially inhomogeneous. An inhomogeneous tip can be described in the framework of the staircase model (Fig. 5.5) [32, 66]. In this model, the tip is assumed to consist of a series of parallel plate capacitors arranged in a staircase-like geometry as depicted in Fig. 5.5. Each capacitor plate is separated by a distance z_i from the surface and has an area A_i and a work function ϕ_i. The total energy of the system is thus the sum over the electrostatic energies of the individual plate capacitors,

$$U_{\mathrm{el}}(V) = -\frac{1}{2}\sum_i C_i \left(V - V_{\mathrm{CPD}i}\right)^2 \tag{5.5}$$

where C_i is the capacity of the ith plate with respect to the surface, V is the applied sample bias and $eV_{\mathrm{CPD}i}$ is the contact potential difference between the ith plate and the surface, respectively. Hence, the frequency shift of the cantilever, $\Delta f(V)$, given by the second derivative of the total interaction potential U_{el} with respect to the tip-sample distance z (Eq. 2.16), is given by

$$\begin{aligned}\Delta f(V) &= -\sum_i \left(\frac{\partial^2 C_i}{\partial z^2}\right)\left(V - V_{\mathrm{CPD}i}\right)^2 \\ &= -\left(\sum_i \frac{\partial^2 C_i}{\partial z^2}\right)\left(V - \frac{\sum_i \left[\frac{\partial^2 C_i}{\partial z^2}\right] V_{\mathrm{CPD}i}}{\sum_i \frac{\partial^2 C_i}{\partial z^2}}\right)^2 + \text{const.},\end{aligned} \tag{5.6}$$

where the constant term does not depend on sample bias. From Eq. 5.6 we see that $\Delta f(V)$ has a parabolic dependence on V, $\Delta f(V) \propto -V^2$, which is similar to the case of a homogeneous tip. However, for the inhomogeneous tip considered here, the maximum of the parabola V_{CPD} is a *weighted average* of the different areas of the tip of different work functions,

$$V_{\mathrm{CPD}} = \frac{\sum_i \left[\frac{\partial^2 C_i}{\partial z^2}\right] V_{\mathrm{CPD}i}}{\sum_i \frac{\partial^2 C_i}{\partial z^2}} \tag{5.7}$$

with the spatial second derivatives of the respective capacitances $\frac{\partial^2 C_i}{\partial z^2}$ acting as weighting factors [66].

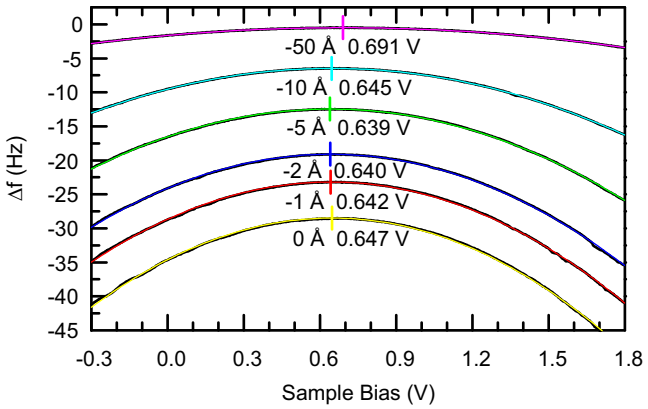

Figure 5.6: KPFS for different tip-sample distances. The frequency shifts $\Delta f(V)$ (black) are fitted by Kelvin parabolas (colored). The standard deviation of each fit is below 1 mV. The relative tip-sample distances Δz and the corresponding contact potential differences V_{CPD} are indicated below each curve. The total variation of V_{CPD} is very small compared to sample bias range considered in our experiment.

For a plate capacitor, the second derivative of the capacitance $C_i(z)$ with respect to tip-sample distance z is

$$\frac{\partial^2 C(z)_i}{\partial z^2} = 2\frac{\epsilon A_i}{z_i^3} \tag{5.8}$$

and hence the weighting factors in Eq. (5.7) strongly depend on z as $1/z^3$. That is, if the microscope's tip is inhomogeneous as its surface has areas of different work function, we expect to find a strong variation of the CPD measured at different absolute tip-sample distances z.

Figure 5.6 shows KPFS measurements for different absolute tip-sample distances acquired with one particular tip apex labeled #1, performed on clean GaAs(110). At a setpoint of $V = 1.8$ V and $I = 20$ pA the feedback loop of the STM was opened. The tip was then retracted by different values of Δz ranging from 0 to 50 Å, and $\Delta f(V)$ was recorded. We find the peak positions of the Kelvin parabolas to differ by less than 45 mV in total. For two additional tip apices labeled #2 and #3 we

proceeded likewise, finding total variations of below 23 mV and 52 mV, respectively. This variation of the CPD for individual apices is very small compared to the bias voltage range considered in our experiments (chapter 10). Accordingly, for the tip apices used, inhomogeneities can be largely ruled out, and we expect the error of V_{CPD} from this side to be on the order of a few tens of meV.

In chapter 10 the tip apices #1 to #3 discussed here were used to investigate the electronic transport through individual buried Zn acceptors.

Part II.

Experimental Procedures

6. Low-Temperature Scanning Probe Microscopy

The research described in this thesis was performed by means of ultrahigh vacuum low-temperature scanning probe microscopy (LT-SPM). The experiments have been performed with two different LT-SPMs, a modified commercial STM and a homebuilt combined STM/AFM. Both machines are based on a design first introduced by G. Meyer at the Freie Universität Berlin [67] and later refined and commercialized by S. Zöphel at SPS-CreaTec [68, 69]. In the following, the relevant parts of the system are briefly summarized; a more detailed description can be found elsewhere [70].

The entire vacuum system of the LT-SPM is sketched in Fig. 6.1a. The scan-head of the SPM is mounted to a 5 K bath cryostat attached to a system of three vacuum chambers, which are interconnected via gate valves. The individual chambers of the vacuum system are (i) a load-lock chamber, pumped by turbomolecular and roughening pumps, for quick introduction of samples into the vacuum system, (ii) a preparation chamber, equipped for sample preparation by sputtering cleaning and for wafer cleavage as well as for residual gas analysis by quadrupole mass spectrometry, and (iii) an SPM chamber, upon which the cryostat is mounted. Both preparation and SPM chamber are brought to ultrahigh vacuum (UHV) conditions by a combination of Ti sublimation and ion-getter pumps as well as by the cryo-pumping effect of the cryostat, with a typical background pressure in the chamber below 1×10^{-10} mbar. Inside the UHV-chamber, samples are handled by a 3-axis manipulator which also allows rotation along its longitudinal axis. The manipulator can be cooled by cryogenic liquids. This allows individual steps of the sample preparation to be performed at sample temperatures down to

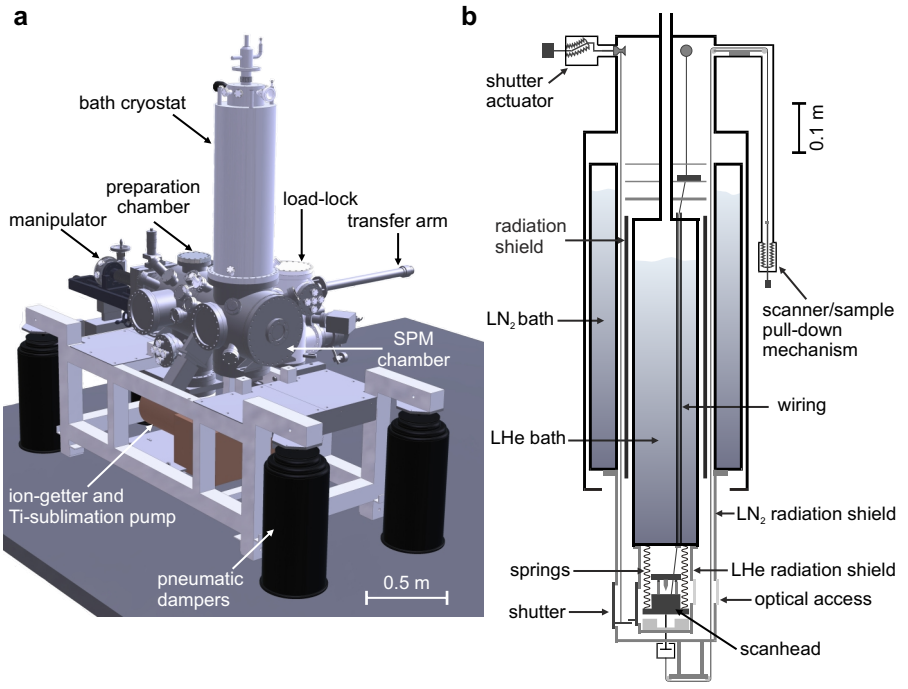

Figure 6.1: The UHV-LT SPM. a, Sketch of the complete UHV-system (design by SPS CreaTec GmbH [68]). The scanner of the SPM is mounted to a 5 K bath cryostat attached to a system of interconnected vacuum chambers. **b**, Cross-sectional view of the bath cryostat. The scanner, concentrically surrounded by cooled radiation shields, is suspended from springs from the base of the LHe cryostat. Image adapted from [69].

about 30 K. For decoupling of external mechanical perturbations, the entire vacuum system rests on four pneumatic dampers.

The bath cryostat of the system is shown in cross-sectional view in Fig. 6.1b. Surrounded by concentric radiation shields, the scanner of the SPM is suspended from springs attached to the base of a 4 l LHe bath cryostat. The latter, thermally isolated by a 15 l LN_2 bath, has a hold time of more than two days, such that the SPM can continu-

ously be operated at 5 K for more than 48 hours. As the sample is entirely surrounded by a radiation shield cooled with LHe, the residual gas pressure at the position of the sample is expected to be far below 1×10^{-10} mbar. This is confirmed by experiments carried out on a single sample where, over several months, no significant increase in the density of adsorbates was detectable. A shutter system allows for sample transfer under vacuum conditions, and optical access allows for guidance of the microscope's tip coarse movement by eye.

During the course of this thesis, a combined STM/AFM scanner was built up from scratch by the author. It is shown in Fig. 6.2. It is similar to the one used to produce the data shown in this thesis. Its details are illustrated in the following. The design of the scanner follows the Besocke *beetle* principle [71, 72]. In this design, three four-segment piezo-tubes (Fig. 2.4), each carrying a sapphire ball, support a ramp ring made out of copper. The latter, having its name from three helical ramps at its lower side (cf. Fig. 6.3a), is moved relative to the piezos by slip-stick motion. Such is induced by application of a proper saw-tooth voltage signal to the segments of the piezo-tubes (Fig. 2.4); up and down rotation (z-coarse movement) by a tangential motion of all piezos, and (x, y)-coarse movement by a parallel motion, respectively. Fine movement of the ramp ring, i.e. the scanning of the sample by the microscope's tip, is performed by the same piezo-tubes.

The actual sensor of the SPM is located at the center of the ramp ring. The entire scan-head is suspended from springs attached to the base of the LHe cryostat. This, in combination with magnets at the scanner's bottom side, sets up an eddy current damping system; damping mechanical low-frequency excitations of the scanner. To provide the lowest possible noise floor of the electronic signal generated by the STM/AFM sensor, an electronic preamplification-stage is located spatially as close as possible to the sensor. Further details on the preamplification are beyond the scope of this thesis. Figure 6.3 shows the sensor of a combined STM/AFM based on the tuning fork design as introduced by F. J. Giessibl [20], mounted at the center of a ramp ring (Figs. 6.3a and 6.3b). It was built up by the author during the course of his thesis. In this

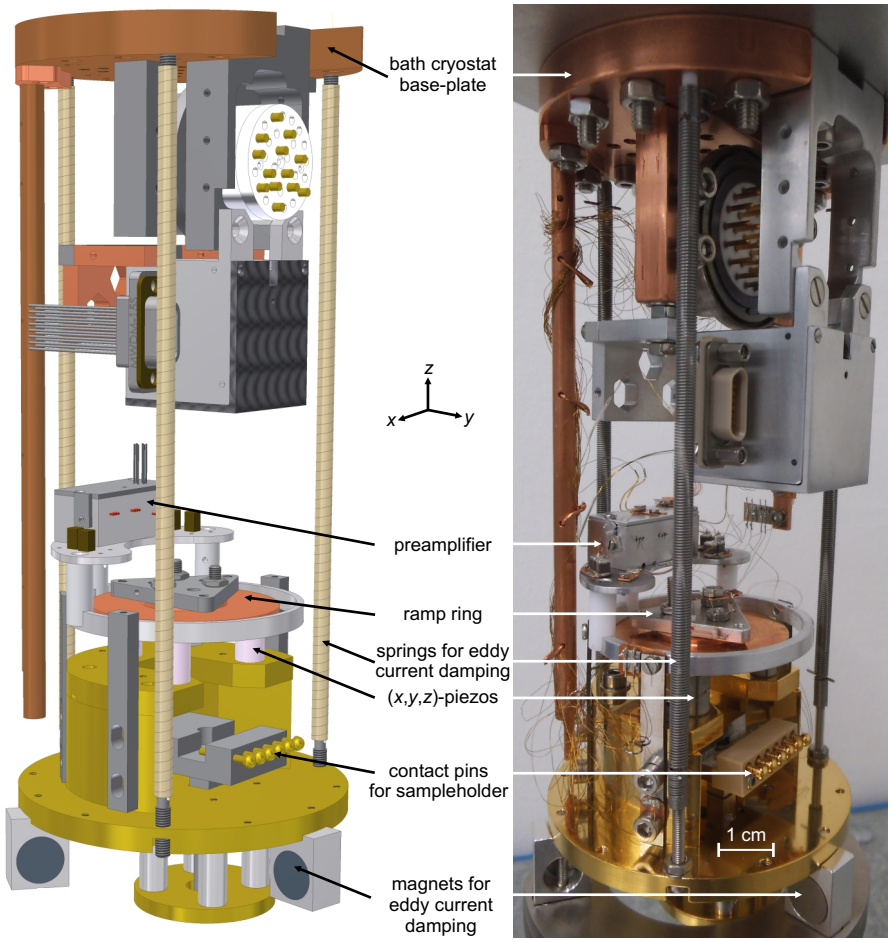

Figure 6.2: The SPM scan-head. Sketch (left) and photograph (right) of a homebuilt STM/AFM scanner (based on a design by SPS CreaTec [68]). The design follows the Besocke beetle principle; a ramp ring is placed atop of three tube piezos, moving it via slip-stick motion. The STM/AFM sensor is placed at the center of the ramp ring; it is shown in detail in Fig. 6.3. The entire scanner is suspended from springs attached to the He bath cryostat, which, together with magnets at the bottom of the scan-head, set up an eddy current damping system. A low electronic noise floor of the STM/AFM signal is provided by a preamplifier stage, located spatially as close as possible to the STM/AFM sensor.

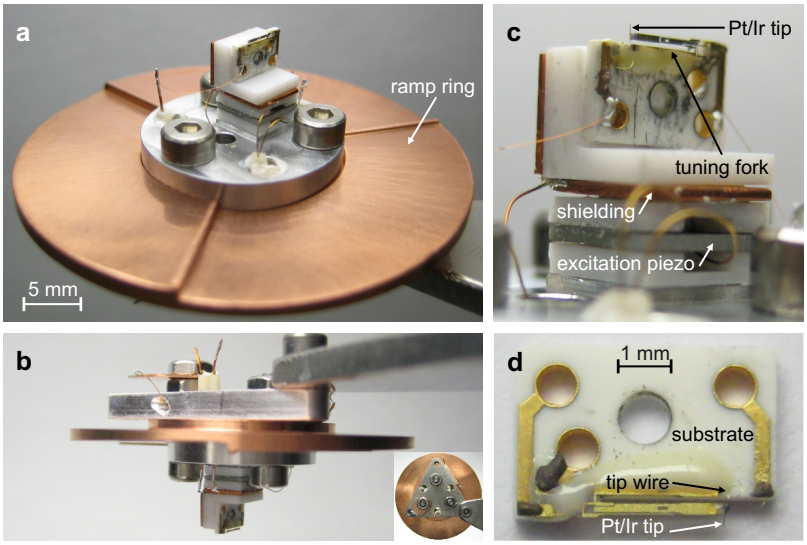

Figure 6.3: The STM/AFM ramp ring. **a** and **b**, Bottom and side view of a homebuilt ramp ring for combined STM/AFM, (inset: top view). **c**, Close-up view of the active part of the ramp ring. The tuning fork of the AFM is mechanically driven by an excitation piezo to resonate close to its eigenfrequency. **d**, One prong of a tuning fork is glued to a substrate, a metallic tip is mounted to its other prong. As the tuning fork is composed of piezoelectric material, mechanical oscillation of the latter converts into oscillation of electric charge. Such can be detected, enabling AFM operation. The metallic tip, connected via a separate tip wire, enables STM operation.

design, a metallic tip is attached to one prong of a tuning fork, the other prong is fixed to a macor substrate (qPlus sensor) [73]. The sensor is shown in detail in Figs. 6.3c and 6.3d. The tuning fork is composed of piezoelectric material. Accordingly, a mechanical oscillation of the tuning fork at some frequency f is correlated to an oscillation of electric charge at the same frequency. The latter can easily be detected and serves as a feedback signal for AFM. The oscillation of the tuning fork is induced mechanically by virtue of a so-called excitation piezo, that is, by mechanically shaking the tuning fork. The excitation piezo is mounted on a stack just below the tuning fork, see Fig. 6.3c. An appropriate voltage signal applied to its top and bottom sides causes the thickness of the

piezo-plate to change on the angstrom scale, which is more than enough to drive the mechanical oscillation of the tuning fork. The metallic tip glued to the free prong of the sensor, contacted via a separate tip wire, allows for a tunneling current between a biased sample and the tip and therefore for the usability of the sensor not only for AFM but also for STM. As the tip of the microscope is rigidly glued onto the free prong of the tuning fork, which itself is rigidly mounted to the ramp ring, *in-situ* tip exchange is not possible in our experimental setup.

Typical values of the qPlus force sensor as used for the experiments described in Sec. 10 are a spring constant k of about 1.8×10^3 N/m^{-1}, a resonance frequency f_0 of about 26 kHz, and a quality factor Q of about 10^4 [70]. Note that the quality factor Q is defined by the resonance frequency of oscillation f_0 divided by the full width at half maximum δf of the resonance peak; $Q = f_0/\delta f$.

The used LT-STM is identical in all parts to the combined STM/AFM described above, except for the sensor. In STM, the tip is rigidly mounted to the ramp ring, as instead of to a tuning fork.

7. Dual-Sample Holder and Sample Preparation

In this thesis, semiconductor samples were investigated in cross-sectional geometry. Such experiments add some extra demands to the already ambitious setup necessary for low-temperature ultrahigh vacuum SPM. These demands concern the preparation of the microscope's tip as well as the sample preparation. In the following, a dual-sample holder is described which allows for reliable *in-situ* tip preparation. Further, the methods of sample preparation are discussed.

7.1. Dual-Sample Holder

As detailed in Sec. 2.1.1, tunneling spectroscopic data are theoretically derived from a convolution of the density of states of the tip with the density of states of the sample (cf. Eq. 2.8). Thus, the assignment of STS data to the sample DOS is only valid in the ideal case of a metallic tip apex the DOS of which is flat.

As our SPM setup does not facilitate tip exchange without breaking of the vacuum, *in-situ* tip preparation is of particular importance. Tip preparation on a semiconducting surface (e.g. via microsecond voltage pulses) might result in the pick-up of clusters of semiconducting material, however, and thus may yield neither a metallic tip apex nor a flat tip DOS. Consequently, such tip preparation results in tunneling spectra whose interpretation in terms of the sample DOS is questionable. Hence, tip preparation on a semiconducting surface is not considered a valid method here. On metallic surfaces, however, preparation of the tip's

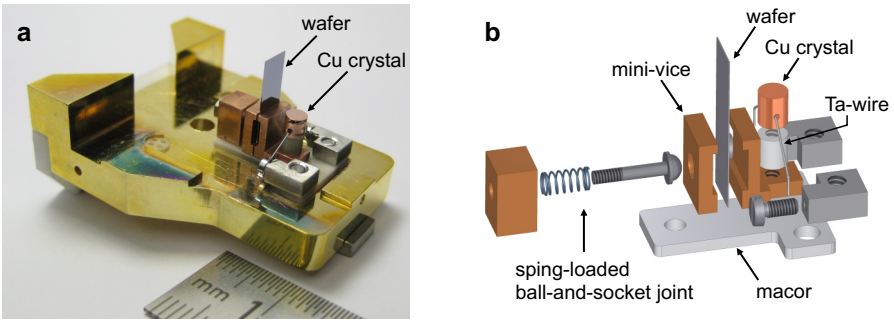

Figure 7.1: The dual-sample holder. **a**, Photograph. The dual-sample holder supports both a metallic as well as a semiconducting sample. As such, the apex of the microscope's tip can be prepared/characterized on the metallic sample before being used to investigate the semiconductor. **b**, Sketch, illustrating the relevant parts of the sample holder. The wafer is clamped by a mini-vice via a spring loaded ball-and-socket joint, ensuring good mechanical and electrical contact both at room and at low temperatures. The Cu crystal is mounted by use of a Ta-wire which also serves for resistive heating via direct current.

apex has been demonstrated to be a ready means to produce reliable tip apices, via microsecond voltage pulses in combination with intended mechanical tip-sample interactions [11, 74, 75]. Moreover, a metallic surface typically does not exhibit an electronic band-gap at its surface, which may allow one to test the spectroscopic reliability of a particular tip apex right after its preparation within a large bias interval.

Consequently, a dual-sample holder has been designed and built up as a part of this thesis. It supports both a metal single-crystal as well as a mini-vice allowing for experiments on semiconductors in the cross-sectional geometry, see Fig. 7.1. Due to this dual-sample holder, within one and the same setup, the tip's apex can be characterized and/or changed on the metallic sample before it is used to investigate properties of the semiconductor. Details of the dual-sample holder are as follows. As metal sample, a (111) terminated Cu single-crystal has been particularly chosen, as (i) this surface exhibits an electronic surface state, the observation of which may be used as a further indication on the spec-

troscopic reliability of a particular tip apex (Fig. 2.8) [24, 76], and as (ii) Cu single-crystals are easily prepared via repeated cycles of sputter-cleaning and annealing, requiring only relatively low annealing temperatures ($T \approx 550\,^{\circ}\mathrm{C}$). The Cu single crystal is mechanically fixed by a Ta-wire, which, at the same time, serves for annealing via direct-current heating, by running a current of about 3.5 A (at a voltage of about 2.2 V) through the wire. The actual temperature of the Cu sample is read out via a thermocouple directly attached to the sample. For the wafer, a mini-vice is used as a sample holder. It is spring-loaded to ensure good mechanical and electrical contact between wafer and mini-vice both at room temperature and at low temperature. To further facilitate this purpose, the load is applied via a ball-and-socket joint, see Fig. 7.1b for a detailed illustration of the relevant parts of the sample holder. Further, this dual-sample holder allows for a cross-voltage to be applied to the wafer; both jaws of the mini-vice can be set at a different electrostatic potential such that a current can be driven through the wafer. The latter also allows for the contact-resistance between wafer and mini-vice to be determined, see Sec. 7.3.

7.2. Sample Preparation

The surface investigated in this thesis is the (110) surfaces of GaAs. This surface is prepared via wafer cleavage, i.e. by the mechanical removal of the upper part of a piece of a wafer [34]. This preparation technique not only allows experiments in the cross-sectional geometry, but also produces surfaces consisting of previously buried atomic layers and thus surfaces of unsurpassable cleanliness.

Although this technique of sample preparation has been employed since the last 20 years by many researchers [6, 9], its physics of brittle fracture and especially the prerequisites necessary to produce large (i.e. µm-scale sized) defect free atomic terraces by cleavage are still far from being well understood. This lack of understanding is due the cleavage process being a highly nonlinear one, involving a macroscopic number of bonds to be

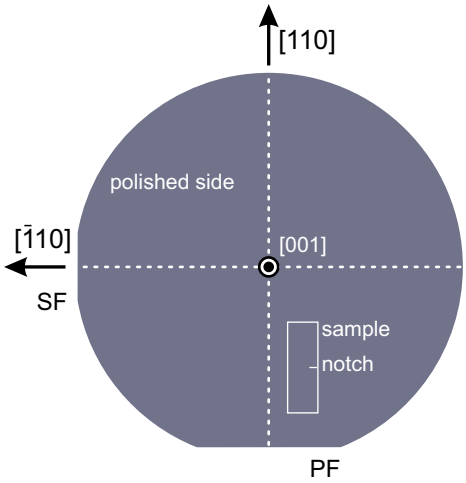

Figure 7.2: To-scale sketch of a 2″-wafer. Wafer directions, as specified by primary and secondary flat (PF, SF; European/Japanese convention) are indicated. A rectangular piece of sample of 4×12 mm^2 is marked. A notch, structurally weakening the wafer and predefining the height at which the cleavage will take place, is indicated. The surface produced from cleavage is of (110) orientation. After [83].

severed [9, 77, 78], which may render theoretical calculations unfeasible.

However, large and defect-free terraces are one of the prerequisites to the experiments aimed for in this thesis. Although there exist some rules in the literature which seem to be of general importance to the production of well-cleaved surfaces, such as the thinning of the wafer to a thickness of below 150 µm and the wafer's structural weakening by application of a notch prior to cleavage [12, 79, 80]; for our setup the procedure to routinely produce well-cleaved surfaces had to be figured out by trial and error. The final procedure is given here, starting from the 2″-wafer as purchased (or as received from the molecular beam epitaxy). First, wafers were either thinned down by hand via etch polishing using a bromine-methanol solution[1] to a thickness of about $90-130$ µm, or were already purchased at a thickness of about 150 µm, which is the minimal thickness commercially available [81, 82]. Second, small rectangular pieces of 4×12 mm^2 size were cut out of the 2″-wafer, such that the surface finally prepared by cleavage is of (110) orientation, see Fig. 7.2. Third, a notch is mechanically applied to one side of the wafer,

[1]The solution consists of 12 ml bromine and 100 ml ethanol, which yields a thinning rate of about 40 µm per minute.

using a tungsten-carbide scribe. The notch is 1 mm long and located 50 µm away from the edge of the wafer in the one direction and 6 mm away in the perpendicular direction (Fig. 7.2). This notch serves two purposes, (i) it structurally weakens the sample, thereby it reduces the mechanical load necessary to initiate the cleavage process. A low mechanical load should enhance the probability that the cleavage process results in a defect-free, atomically flat surface, as any excess energy put into the elastic deformation of the wafer is expected to be released by the creation of steps or defects [78] and, (ii) it fixes the position of the fracture plane with respect to the lower edge of the wafer to be at the correct height for the microscope's tip. Fourth, the wafer is mounted to the mini-vice and introduced into the vacuum chamber.

As both the surface of the Cu single crystal as well as the surface of the wafer had to be available in one and the same experimental run, they had to be prepared in parallel inside the vacuum chamber. The individual steps of this preparation process are illustrated in Fig. 7.3. First, the surface of the Cu single crystal is prepared by repeated cycles of sputter-cleaning and annealing. Sputtering of the GaAs sample during this preparation step is avoided by a removable high-purity Cu mask, see Fig. 7.3a. Without this, the Cu(111) surface would be contaminated by sputtered GaAs particles. Once the Cu(111) surface is prepared, the removable Cu shield is dropped off, see Fig. 7.3b. The GaAs(110) surface is then prepared by removing the upper part of the sample via cleavage, by applying mechanical force to the sample's upper part, typically while the sample is at a temperature of below 150 K and at a back-ground pressure of below 1×10^{-9} mbar; see Fig. 7.3c. To avoid post-cleavage contamination of the samples, the sample holder is transferred into the cold STM or STM/AFM scan-head within less than one minute after cleavage; see Fig. 7.3d. In the best case, this procedure results in clean, µm-wide atomically-flat terraces of (110) terminated GaAs, as well as in a well-prepared Cu(111) surface, both accessible to the microscope's tip.

Although great efforts have been made, it was not possible to reliably produce atomically flat surfaces via cleavage of *n*-type GaAs wafers doped

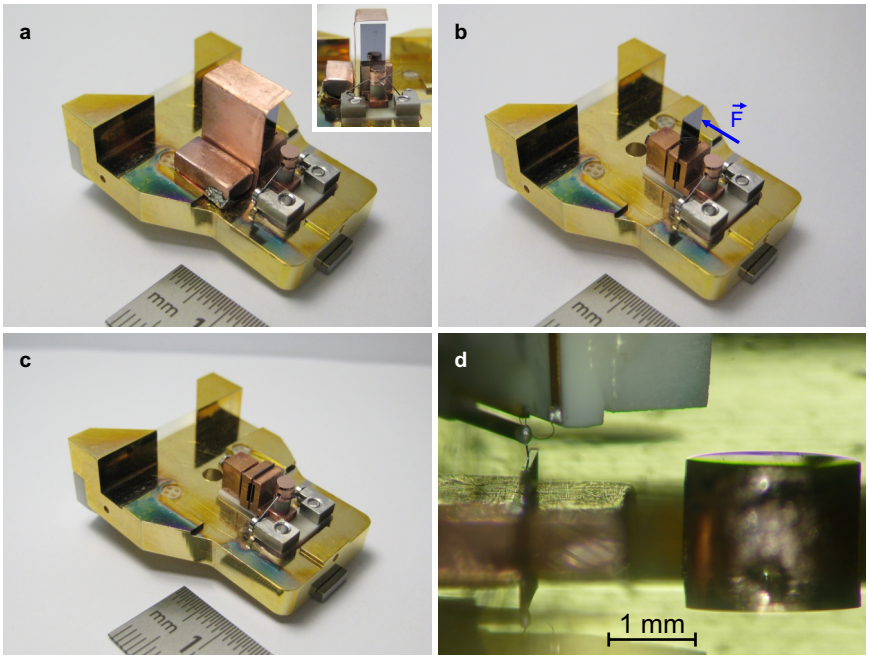

Figure 7.3: The individual steps of sample preparation. **a**, A high-purity copper shielding is used to avoid sputtering of the GaAs sample during the sputter-cleaning of the Cu(111) surface (inset: front view). **b**, and **c**: Before and after the GaAs(110) surface is prepared by sample cleavage, by mechanically removing the top part of the wafer. **d**, Sample holder mounted inside the STM/AFM scan-head; the microscope's tip is positioned above the GaAs sample surface.

with Si atoms. However, when *p*-type GaAs wafers doped by Zn atoms were used, the above described method nearly always resulted in cleaved surfaces of low defect density and of large-size atomically flat terraces almost everywhere on the wafer. That *p*-type GaAs wafers doped with Zn indeed cleave more easily is in accordance with the experience of other work groups, which reported atomically flat surfaces even from the cleavage of non-thinned (i.e. 300 µm thick) Zn-doped wafers [58]. A explanation of this fact is so far not available in the literature.

An example of a successful sample preparation is shown in Fig. 7.4,

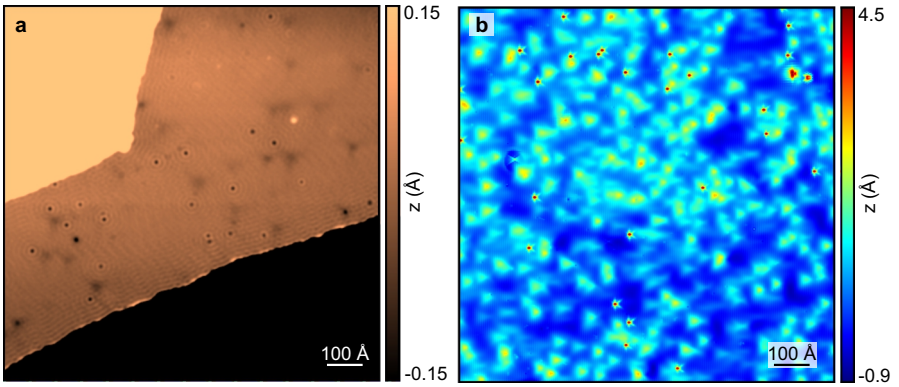

Figure 7.4: Typical constant-current STM images of Cu(111) and of GaAs(110). **a**, STM image of Cu(111). The z scale is chosen to highlight the standing wave pattern related to scattering of surface state electrons on step edges and adsorbates. Sample bias +50 mV, tunneling current 2.5 pA. **b**, Low-bias empty state STM image of the (110) surface of Zn-doped GaAs. The surface is atomically flat; the observed features are the fingerprints of Zn acceptors located in and below the (110) surface. Sample bias +1.5 V, tunneling current 10 pA.

depicting large-scale constant-current STM topographies of Cu(111) as well as of the (110) surface of Zn doped GaAs.

7.3. Voltage Drop in Sample Contacts

For the experiments reported in this thesis, one key ingredient to the qualitative interpretation of the STS data is the correct assignment of features observed in STS to the sample bias at which they are observed. Accordingly, it is of great importance that the bias applied to the SPM indeed corresponds to the bias that is applied to the sample. For semiconducting samples, however, it is well known that a Schottky contact between metallic sample holder and sample can reduce the sample bias by some unknown and current-dependent fraction [84].

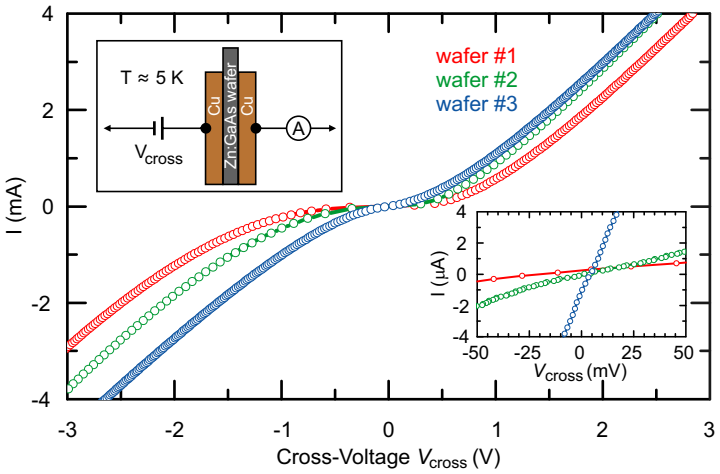

Figure 7.5: Current versus cross-voltage characteristic, $I(V_{\mathrm{cross}})$, of the sample holder with a mounted Zn-doped GaAs wafer (geometry as illustrated in the top-left inset). Curves are acquired for three different wafers, labeled #1 to #3, with the sample holder mounted inside the cold STM/AFM. The bottom-right inset shows $I(V_{\mathrm{cross}})$ for a limited voltage range around zero volts.

Figure 7.5 shows the current versus cross-voltage characteristic, $I(V_{\mathrm{cross}})$, of the sample holder with mounted Zn-doped GaAs wafer, acquired at a temperature of 5 K with the sample holder mounted inside the cold STM/AFM. Curves are acquired for three different pieces of GaAs wafers, having similar nominal Zn acceptor concentrations (as specified by the supplier) of about 1×10^{19} cm^{-3}. The geometry of the setup is sketched in the top-left inset of Fig. 7.5. No specific treatment has been applied to the GaAs wafer to achieve ohmic contacts between the wafer and the metallic (Cu) clamps of the sample holder. The experimentally determined $I(V_{\mathrm{cross}})$ trace shows a non-ohmic behavior, as it is expected for a metal-semiconductor-metal contact. Slight variations, as observed for wafers #1 to #3, are expected to be due to slightly different mechanical clampings of the individual samples inside the mini-vice. The bottom-right inset shows $I(V_{\mathrm{cross}})$ for a limited voltage range around zero volts (note that the zero-crossing of the current traces does not occur ex-

actly at zero volts, which is due to some small offset in the bias). Most important, the voltage drop observed at a current in the µA range is on the order of 10 mV. The tunneling currents used in our experiments are in the pA range, i.e. six orders of magnitude below the µA range. Hence, in our experiments, the fraction of the sample bias that will drop off across the sample contacts is (for the Zn-doped GaAs samples investigated) far below 10 mV and can safely be neglected. This finding is of particular importance to the experiments described in chapter 10.

Part III.

Experimental Results

8. Probing Individual Weakly Coupled π-conjugated Molecules on Semiconducting Surfaces

The research presented in this chapter has been partially published in Journal of Applied Physics [85]. Parts of the text are identical to the publication[1,2]*.*

This chapter presents an STM study of iron(II)-phthalocyanine (FePc) molecules adsorbed on the (110) surface of GaAs. A weak perturbation of a single molecule by the supporting substrate is a key ingredient to molecular electronics. Here, we show that individual FePc molecules adsorbed on GaAs(110) surfaces represent a prototype for weakly coupled single-molecule/semiconductor hybrid systems. This is demonstrated by scanning tunneling spectroscopy and by bias-dependent scanning tunneling microscopy images that closely resemble orbital densities of the free molecule. This is in analogy to results for molecules decoupled from a metal substrate by an ultrathin insulating layer [87] and proves a weak electronic molecule-substrate coupling. Therefore, such system will allow single-molecule functionality to be combined with the versatility of semiconductor physics.

[1] G. Münnich et al., *Journal of Applied Physics* **112**, 34312 (2012).
[2] This research was, in part, conducted in collaboration with Florian Albrecht and some of the presented results are also discussed in [86].

8.1. Introduction

In the ultimate limit of downscaling electronic devices, the functional parts would be single molecules or even atoms. One promising route towards this goal is the combination of single-molecule functionality with semiconductor based nanoscale devices, which are the building blocks of today's electronics [88–90]. On this route, the coupling between the molecule and the substrate is of key importance. Here, one needs to discriminate between (i) the molecule-surface bond, which is required to be strong to achieve thermal stability of the device, and (ii) the electronic coupling of the molecule's *frontier orbitals*[3] [91], which must be weak to retain a desired single-molecule functionality. At first glance, these two premises seem to be contradictory. However, the use of molecular anchoring groups, e. g. carboxylic acids [92], allows to pin the molecule to the substrate. Such anchoring groups will not significantly contribute to the frontier orbitals and will therefore allow to ensure thermal stability independent of premise (ii). Here, we focus on the latter, by presenting an electronically weakly coupled molecule-substrate system.

A weak coupling between the molecule's frontier orbitals and the substrate can be oppressed by the chemical reactivity of semiconductor substrates, leading to a rich variety of reactions like chemisorption with strong covalent bonding [88, 93], cycloaddition reactions [94, 95] or even molecular fragmentation [96]. This obstacle may be overcome by surface passivation [97] or by the use of a low-reactive molecule/semiconductor system.

Single-molecule functionality has been demonstrated for the class of phthalocyanine (Pc) molecules, exhibiting molecular magnetism [98–100] and various types of conductance switching [101–103]. Interestingly, Pc molecules on some III–V semiconductor surfaces are believed to interact weakly with the substrate, as is mainly concluded from self-ordering in

[3]The *frontier orbitals* are the highest occupied molecular orbital (HOMO) and the lowest unoccupied molecular orbital (LUMO), respectively.

thin molecular films, as found by averaging techniques like low energy electron diffraction [104–106]. In addition, the appearance of these molecules in films in STM imaging hinted at a weak coupling [107]. However, despite these promising indications, to date the electronic structure of an *individual* physisorbed molecule on a bare semiconducting substrate has not been resolved.

To this end, we performed STM of FePc adsorbed on bare GaAs(110), deposited at a substrate temperature below 20 K. The STM, introduced in chapter 6, was operated at ~ 5 K in UHV.

We probe the electronic properties of individual molecules using scanning tunneling spectroscopy and bias-dependent imaging. These images closely resemble the orbital densities of the free molecule. In analogy to molecules electronically decoupled by an insulating layer from a metal substrate, this finding proves a weak electronic coupling [87]. This is further corroborated by the possibility of current-induced lateral movement of the FePc molecules by inelastic excitation.

8.2. The Substrate System

The GaAs sample used as substrate was grown by molecular beam epitaxy by M. Utz and D. Schuh (University of Regensburg). It consists of a 250 nm thick slab of nominally undoped (*intrinsic*) GaAs grown atop of a degenerately n-doped GaAs-based heterostructure (Si, 4×10^{18} cm^{-3}), capped by a 200 nm thick degenerately p-doped layer (Mn, $\approx 5 \times 10^{20}$ cm^{-3}). The heterostructure contains AlGaAs marker layer which are used to pilot the microscope's tip to the desired region above the heterostructure. From its layout, the heterostructure constitutes a p-i-n diode. The cross-section of this diode, i.e. the (110) surface of the wafer, is made accessible to the tip via wafer cleavage, as it is introduced in chapter 7. The sample was thinned down to about 130 µm to enhance the likeliness of the cleavage process resulting in atomically flat terraces of macroscopic size.

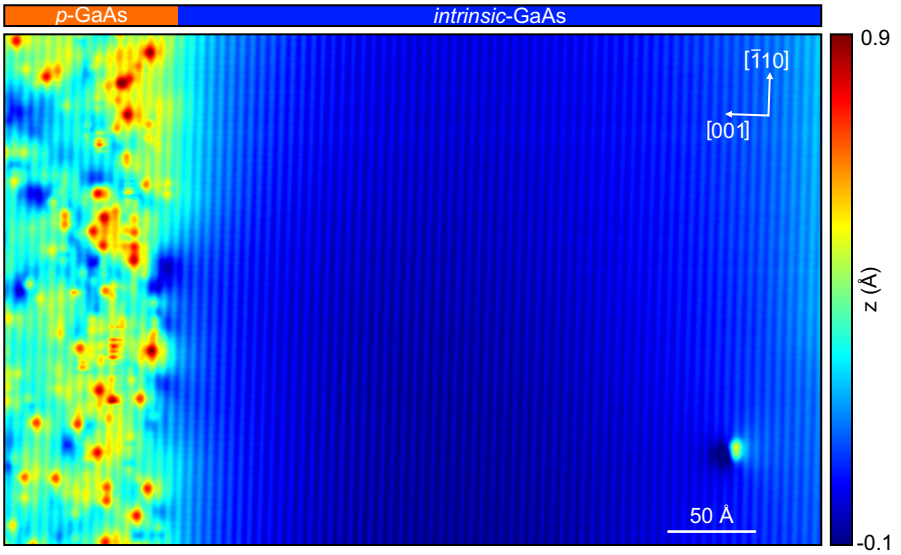

Figure 8.1: Atomically resolved constant-current filled-state STM image (V = -2.2 V, I = 8 pA) of the p-GaAs/*intrinsic*-GaAs interface. The p-doped layer appears bright in the image, the short-range features visible in this layer are the fingerprints of individual Mn dopant atoms. At this particular sample bias, the GaAs lattice is visible as parallel stripes running along the $[\bar{1}10]$ direction. The long-range apparent height change in the intrinsic region originates from the built-in potential of the heterostructure. A single defect (the bright feature at the lower right edge) is visible in the otherwise atomically flat and clean (110) surface prepared by sample cleavage.

The use of such a *p-i-n* heterostructure as a substrate to study single molecules is of particular interest, as it (i) allows one to study individual molecules adsorbed in the intrinsic region, where any influence from nearby located dopant atoms to adsorbed molecules can be excluded, and as it (ii) provides a built-in electrostatic potential which can be exploited to tune molecular resonances, which will be the topic of chapter 9.

Figure 8.1 shows a large-scale STM image of a part of the heterostructure; the p-GaAs/*intrinsic*-GaAs interface. The AlGaAs marker layer embedded in the n-doped region of the heterostructure were used to

pilot the microscope's tip to this part of the wafer. The image was acquired prior to the deposition of molecules and shows an atomically flat and almost defect free (110) surface. At the particular sample bias chosen ($V = -2.2$ V, filled state imaging), the p-doped layer appears bright and the GaAs lattice is visible as parallel stripes running along the $[\bar{1}10]$ direction. The short-range corrugation observed in the p-doped layer is caused by individual Mn dopant atoms located in and below the sample's (110) surface [108, 109]. The long-range corrugation observed in the intrinsic region along the [001] direction is a consequence of the built-in electrostatic potential of the sample.

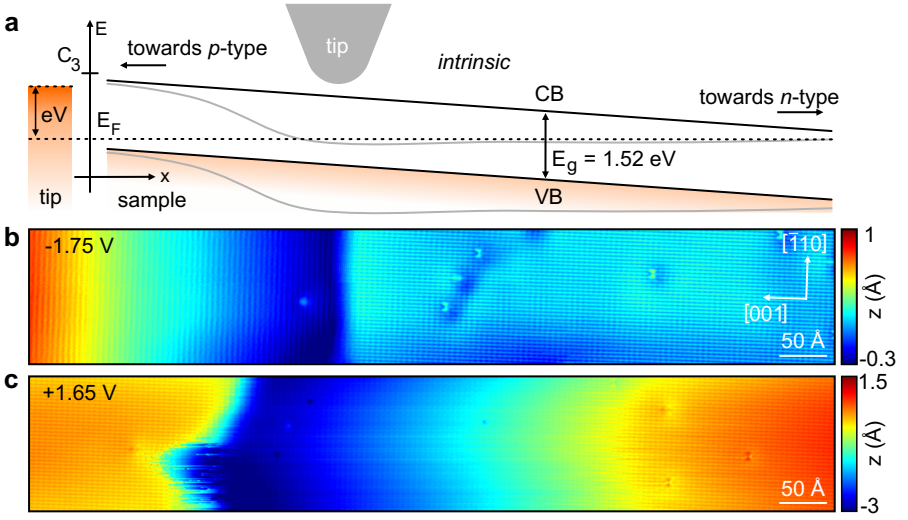

Figure 8.2: a, Sketch of the band-edge alignment within the intrinsic region of a p-i-n diode in absence (black lines) and under consideration of TIBB (gray lines, sketch for negative sample bias). The $C3$ surface resonance is, in energy, located above the conduction band edge. In the absence of TIBB, for filled (empty) state imaging, the $C3$ resonance is expected to contribute nowhere (everywhere) to imaging (see main text). **b** and **c**, Filled and empty state constant-current STM images of the intrinsic region (sample biases as indicated, set-point current 1 pA). Both images show the same area of the wafer, the drastic change in corrugation is an electronic effect as the surface is atomically flat. The observation (absence) of the $C3$ surface resonance in b (c) is a consequence of tip-induced band bending.

The finite conductance within the *intrinsic* part at low temperatures, necessary to perform STM, is attributed to TIBB effects, spatially extended across the intrinsic region. It is assumed that for negative (positive) sample bias exceeding a certain magnitude, the conduction (valence) band is dragged across the Fermi level, resulting in an accumulation or depletion layer at the surface. Such assumption is plausible, as in the intrinsic region the number of free charge carriers screening the tip's electrostatic field is expected to be extremely low, and thus TIBB effects are assumed to be strong. This assumption is experimentally corroborated by Fig. 8.2. It shows STM images of the intrinsic region, acquired at different sample biases, as well as an energy-scheme of the tunneling-junction and of the band-edge alignment within the *intrinsic* region in absence of TIBB (black lines). Interestingly, in the STM images a $C3$ surface resonance related corrugation is observed (absent) for filled (empty) state imaging. A contribution of the $C3$ surface resonance to tunneling results in a corrugation along the $[\bar{1}10]$ direction (see Sec. 3.4), as it is observed in right section of Fig. 8.2b and as it is absent in the center of Fig. 8.2c, respectively. In energy, the $C3$ surface resonance is located above the edge of the conduction band (cf. Fig. 8.2a). If TIBB effects were negligible, the $C3$ surface resonance should not at all (everywhere) contribute to tunneling for a sample bias of $V = -1.75$ V ($V = +1.65$ V), exceeding the band gap of GaAs. However, as the $C3$ surface resonance is observed (absent) in the filled (empty) state STM image, there must be significant TIBB effects in the intrinsic region, locally dragging the $C3$ surface resonance below (above) the Fermi level and making it contribute to the imaging process. Such situation is depicted by the gray lines in Fig. 8.2a, sketching the band-edge alignment under the influence of TIBB for a negative sample bias. The TIBB (locally) pushes the conduction and valence band edges downward in energy, and the conduction band edge (locally) crosses the Fermi level (as will the $C3$ surface resonance). Hence, electrons will accumulate below the microscope's tip and the $C3$ surface resonance will (locally) be occupied and therefore locally contributes to tunneling.

It is noted that, as imaging of the complete heterostructure for both bias polarities was already possible prior to the adsorption of molecules (cf.

Figs. 8.1 and 8.2) doping by FePc can be ruled out as a reason for the finite conductance observed in the *intrinsic* region at low temperatures.

8.3. Iron(II)-Phthalocyanine

In the experiments described here, iron-II-phthalocyanine was studied as an adsorbate. The chemical structure and a ball model of FePc are shown in Figures 8.3a and 8.3b. FePc is a molecule of the family of the metal phthalocyanines (MPcs). The MPcs are metal complexes, i.e. molecules in which a metal atom is bound to a surrounding organic molecule (the ligand). For the MPcs, the ligand is the macrocyclic aromatic molecule Pc, which is characterized by a conjugated π-system, that is, by a system of electronic states delocalized over the entire macrocycle of the molecule [111, 112].

Within the family of the MPcs, molecular properties such as energy level spacings, orbital occupancies and molecular magnetism are determined by the particular metal atom coordinated [113]. For FePc, the latter is iron at a formal charge state of II. The spin state of FePc is the spin-triplet one ($S = 1$) [114]. The geometry of FePc is shown in Fig. 8.3b. FePc is a cross-shaped planar molecule [111]. Figure 8.3c shows the electronic energy levels as well as sketches of the molecules frontier orbitals (including the HOMO-1), as calculated by density functional theory (DFT) [110]. The orbitals are overlayed to the molecular geometry, blue and green indicate the sign of the wave function. The HOMO of free FePc is centered at the molecules ligand. It is of a_{1u} symmetry. The HOMO-1 is of a_{1g} symmetry and is located solely at the metal center of the molecule. Finally, the LUMO of free FePc is two-fold degenerate, and both e_g symmetric orbitals are spread similarly over the molecules ligand as well as over its metal center.

It is noted that the sequence of molecular resonances calculated by DFT varies for different functionals and basis sets [110, 113]. However, independent of the latter, the highest occupied ligand centered molecular

resonance is always of a_{1u} symmetry, while the highest occupied metal centered molecular resonance is always of a_{1g} symmetry. This is in accordance with experimental data of STM of MPcs decoupled from metal substrates by ultrathin insulating layers [115].

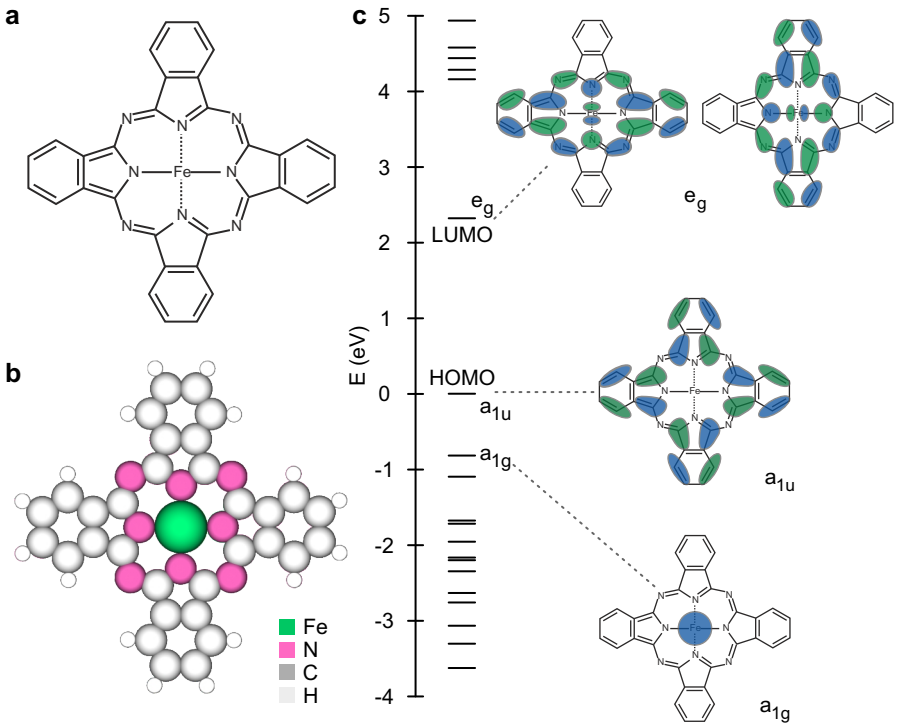

Figure 8.3: Iron(II)-phtalocyanine. a and **b**, Chemical structure and ball model of iron(II)-phthalocyanine (FePc, $C_{32}H_{16}FeN_8$). FePc is a macrocyclic aromatic molecule of cross-shaped planar geometry. **c**, Energy levels and sketches of selected molecular orbitals, as calculated by DFT. The highest occupied molecular orbital (HOMO) is arbitrarily shifted to 0 eV. The lowest unoccupied molecular orbital (LUMO) is two-fold degenerate, both (e_g symmetric) orbitals are shown. The HOMO (a_{1u}) and HOMO-1 (a_{1g}) are exclusively centered at the molecules ligand or its metal center. The LUMO is spread out across the ligand as well as the metal center. Blue and green represent the sign of the wave function. After Ref. [110].

The FePc molecules were sublimated from a thermal evaporator source (at a temperature of about 500 °C) onto the GaAs(110) surface at a sample temperature of $T < 20$ K, with the sample mounted inside the STM.

8.4. Weak Electronic Molecule-Substrate Coupling

Having introduced the substrate and adsorbate systems in the previous sections, experimental results for FePc adsorbed on the heterostructure's *intrinsic* layer are now discussed.

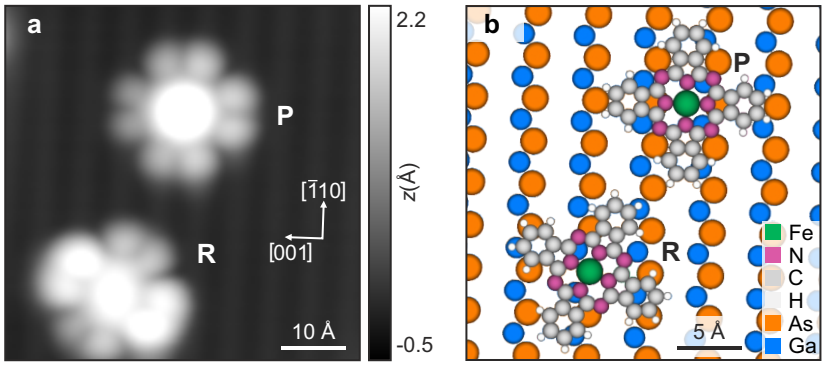

Figure 8.4: Iron(II)-phthalocyanine on GaAs(110). a, Constant-current STM image of two FePc molecules adsorbed on the (110) surface of intrinsic GaAs. The molecules are found in two inequivalent adsorption geometries, labeled P and R, respectively. STM image acquired at a sample bias of $V = -2$ V and a tunneling current of $I = 3$ pA. **b**, Model for FePc on the top-layer of relaxed GaAs(110). Note that images and distances between molecules in (a) and (b) are not to scale.

Figure 8.4a shows a constant-current STM image of two FePc molecules adsorbed on the (110) surface of *intrinsic* GaAs. All FePc molecules are found in two inequivalent adsorption geometries, one aligned with the $[\bar{1}10]$ and [001] directions (labeled P in Fig. 8.4), the other one rotated by an angle of $\pm(25\pm3)°$ (labeled R). The adsorption position and geometry

of both species has been determined from bias-dependent STM imaging and is shown in Fig. 8.4b. The adsorption position determination is discussed in detail in Sec. 8.5.

To probe the electronic properties of adsorbed FePc, we recorded differential conductance $[dI/dV(V)]$ spectra and acquired corresponding bias-dependent STM images for FePc in the P geometry. The $dI/dV(V)$ spectra were acquired with lock-in technique, adding a small *ac* signal of (peak-to-peak) 106 $\mathrm{mV_{pp}}$ and of 160 Hz frequency to the *dc* sample bias.

$dI/dV(V)$ spectra of individual FePc molecules exhibit distinct features on the positive and negative bias side, separated by a broad gap of low conductance, see Fig. 8.5a. To resolve metal-centered as well as ligand-centered molecular resonances, spectra were acquired at the center and at the periphery of the molecule. $dI/dV(V)$ spectroscopy of bare GaAs acquired with the same tip apex in the direct vicinity of the molecule shows an apparent band gap of about 2 eV but is featureless where molecular resonances are observed. This large apparent band gap is attributed to the effects of TIBB [48, 116]. To achieve a high dynamic range in $dI/dV(V)$ spectroscopy, the tip-sample distance was decreased while the sample bias was ramped [$\Delta z(V)$-curve in Fig. 8.5a]. Spectra acquired with the tip-sample distance kept constant do not qualitatively differ from those, as is clarified by the inset of Fig. 8.5a, in which data for a different molecule acquired with a different tip apex are shown [$dI/dV(V)$ data points are averaged of over a bias range of 53 mV]. Bias-dependent images at voltages corresponding to different spectroscopic features (Fig. 8.5b) qualitatively differ from each other: When imaging with relatively low absolute sample bias ($|V| < 1.5$ V), exceeding the apparent band gap of GaAs, the molecule appears (for both sample bias polarities) as a featureless cross closely resembling the molecule's cross-shaped geometry (cf. Fig. 8.3b). In contrast, for sample biases corresponding to the peak positions, the molecule shows pronounced internal structure. The image of the ligand-centered resonance at a negative sample bias of $V = -1.5$ V shows the well-resolved orbital structure of the $\mathrm{a_{1u}}$ orbital, which is the highest occupied ligand-centered

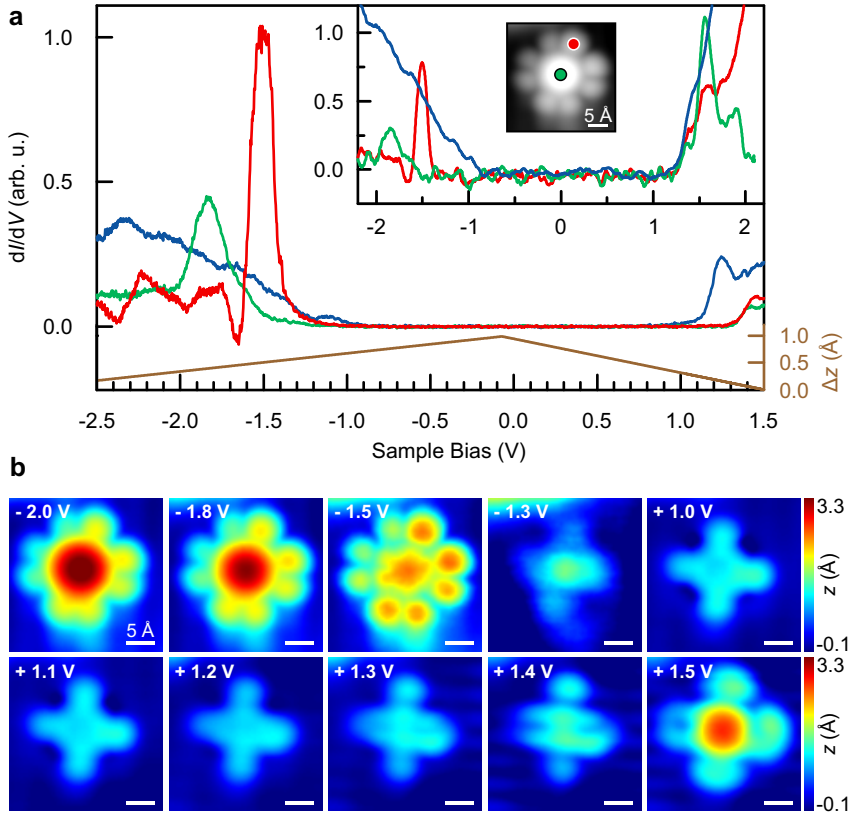

Figure 8.5: STS and bias-dependent STM imaging of FePc on GaAs(110). **a**, $dI/dV(V)$ spectra at the molecules metal center (green line; positions are indicated in the STM image shown as inset, V = -1.8 V, I = 3 pA) and at its ligand (red line). For comparison, a spectrum acquired at the bare GaAs(110) surface is shown (blue line). Whereas the tip-sample distance was varied for the spectra in the main figure (brown line, $\Delta z(V)$ is the change in vertical tip position), it was kept constant for the spectra in the inset. For both sample bias polarities, distinct peaks are observed and attributed to molecular resonances. **b**, While images at absolute bias voltages below molecular resonances ($|V| < 1.5$ V) show a featureless cross, pronounced intra-molecular contrast is observed for higher absolute values of the sample bias. Constant-current STM images recorded at tunneling currents of (from left to right) 3 pA, 3 pA, 1 pA, 0.5 pA, 1 pA (top row) and 2 pA, 2 pA, 2 pA, 1 pA, 1 pA (bottom row), and sample biases as indicated.

orbital (HOMO) of free FePc (cf. Fig. 8.3c) [110, 113]. In particular, we find that the nodal plane structure revealed in our images corresponds exactly to the structure of the free molecule as calculated by DFT. See Fig. 8.6 for a comparison of STM images of FePc molecules in the P and in the R geometry with the DFT-calculated a_{1u} orbital density of the free molecule[4] [117, 118]. The images at a more negative sample bias, beyond the metal-centered peak in $dI/dV(V)$ spectroscopy ($V = -1.8$ V and $V = -2.0$ V, respectively) show, in addition to the structure observed at $V = -1.5$ V, a pronounced protrusion at the metal center. Consequently, the peak in $dI/dV(V)$ spectroscopy at $V = -1.8$ V can be attributed to a metal-centered molecular resonance. This fits well to an a_{1g} metal-centered resonance which is expected at an energy close to the HOMO (cf. Fig. 8.4a) [110]. At a positive sample bias of about +1.5 V, one peak in $dI/dV(V)$ spectroscopy is observed both on the ligand and on the metal center. Correspondingly, the resonance image shows strong intensity distributed across the entire molecule. This image shows no pronounced nodal planes, and its appearance would be consistent with an incoherent superposition of two orthogonal e_g orbitals. An incoherent superposition of orbitals in STM imaging is expected if the orbitals in question all contribute to the current. The free molecule has indeed two degenerate e_g frontier orbitals (cf. Fig. 8.4a).

The above described observations of well-resolved peaks in $\mathrm{d}I/\mathrm{d}V$ spectroscopy and the corresponding orbital structures in bias-dependent images are very reminiscent to studies of molecules on ultrathin insulating films [87, 101, 103]. This proves that the electronic structure of the free molecule is preserved to a large extent upon adsorption. We note that the absolute energies of the FePc's resonances are not straightforward to extract from $dI/dV(V)$ spectra due to TIBB. As the apparent substrate surface corrugation is unperturbed in the direct vicinity of the molecules for both bias polarities, we conclude that the molecule is uncharged at all tunneling conditions used [119, 120]. Qualitatively, spectroscopic data and corresponding images for FePc adsorbed on different positions within *intrinsic* and on *n*-doped GaAs do not differ from each other, except for

[4]The DFT calculation was performed by I. Swart (University of Utrecht).

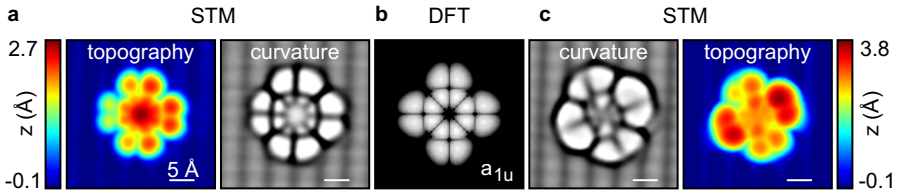

Figure 8.6: Comparison between STM and DFT. a and **c**, Constant-current STM topography and corresponding curvature of individual FePc molecule adsorbed in either P or R geometry, respectively. Images are acquired at V = -1.8 V, I = 1 pA (a) and V = -1.4 V, I = 0.5 pA (c). **b**, a_{1u} orbital density of the free molecule as calculated by DFT. The STM images in (a) and (c) show pronounced intra-molecular contrast; the nodal plane structure observed closely resembles the one of the a_{1u} orbital density of the free molecule.

the positions of molecular resonances in energy. Such is expected due to the change of the electrostatic potential within the *p-i-n* structure, as well as due to the variation of the magnitude of TIBB, which changes for tip positions atop degenerate doped or atop intrinsic GaAs, respectively. The effect of the adsorption position across the *p-i-n* structure on molecular resonances is the subject of chapter 9.

The comparison of the appearance of the molecules in P and R configuration in Fig. 8.6 reveals that the nodal plane structure is very similar for both orientations, underpinning the small influence of the substrate. Only differences in the relative height of the different lobes can be observed. Similar differences are also observed for opposite lobes within individual P-type molecules with respect to the [001] direction. We note that this effect was present for all investigated molecules in the P geometry (24 in total). The observed slight differences in lobe intensities are attributed to the different local environment, caused by the polar nature of the GaAs substrate. For P-type molecules, this effect is discussed in detail in Sec. 8.5.

Note that the STM images in Figs. 8.6a and 8.6c show a protrusion at the metal center of the FePc, whereas the calculated a_{1u} orbital density is zero at the center of the molecule. The STM images have been

acquired at a sample bias more negative then the first ligand-centered resonance in $\mathrm{d}I/\mathrm{d}V(V)$, slightly above the onset of the metal-centered resonance of the FePc molecule (cf. Fig. 8.5a). Hence, both the a_{1u} and a_{1g} orbital contribute to tunneling, and the molecules appearance in the STM images is not only determined by the a_{1u} orbital density, but by an incoherent superposition of a_{1u} and a_{1g} orbitals. The orbital density of the latter is non-zero at the FePc's metal center (cf. Fig. 8.3a) and consequently a protrusion at the molecules metal center is observed.

FePc can be moved laterally by current-induced inelastic excitation, as is shown in Figure 8.7. The current required for an inelastic excitation that results in a lateral motion within a few seconds is in the low pA regime and similar to the one for current-induced manipulation processes of molecules on ultrathin insulating films[5] [121]. In the case of insulating films, such a high yield was attributed to a strongly increased lifetime of injected electrons within the molecule due to the electronic decoupling of the latter [101]. Similarly, FePc molecules adsorbed in P geometry can be switched into the R geometry (Fig. 8.7) and vice versa. After these current-induced processes, spectra and images are the same as before, confirming that the molecule and the substrate are not damaged. These observations provide further evidence that the bonding to the substrate is weak.

In conclusion, the electronic properties of individual physisorbed π-conjugated molecules adsorbed on the (110) surface of intrinsic GaAs have been studied. The findings show that the electronic structure of FePc is preserved to a large extend upon low-temperature adsorption. This results in molecular resonances well separated in energy allowing for molecular orbitals to be imaged. As mentioned above, such weak interaction between an adsorbed molecule and a semiconducting substrate is surprising at first glance, as semiconducting surfaces are typically expected to be chemically reactive due to dangling bonds. A high reac-

[5] The lateral movement of the molecule occurred while the feedback-loop of the STM was switched off and the sample bias ramped. Maximum values of the bias ramp and the tunneling current are $|U| < 2.2$ V and $|I| < 4\ pA$, resulting in a lateral motion within a time $t < 160$ s.

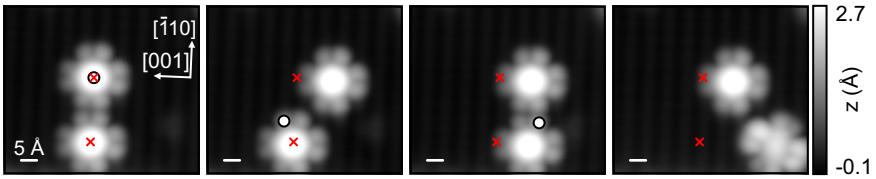

Figure 8.7: Current-induced movement of FePc on GaAs(110). Series of constant-current STM images, showing two FePc molecules adsorbed on GaAs(110). Both molecules are moved (top molecule) and switched from P into R configuration (bottom molecule) by current-induced inelastic excitations. As a guide to the eye, the red crosses indicate the center of the molecules before the first manipulation step. The open dot defines the position where the current was injected. STM images are acquired at a tunneling current of 3 pA and a sample bias of -2 V, except for the right-most figure, which was acquired at -2.2 V.

tivity between molecule and substrate is indeed observed for many silicon surfaces [88, 93, 96] terminated by half-filled dangling bonds. The GaAs(110) surface studied here is terminated by fully occupied and completely empty dangling bonds only (see Sec. 3.2). Thus, the weak interaction between the molecules and the substrate may be a consequence of the lower chemical reactivity attributed to a saturated dangling bond. This idea is corroborated by an STM study of naphtalocyanine molecules adsorbed on the InAs(111)A surface [85]. Similarly to the GaAs(110) surface, the InAs(111)A surface is terminated by completely filled or empty dangling bonds only. Indeed the interaction between molecule and substrate is found to be weak for molecules adsorbed on InAs(111)A. Apart from this, the adsorption of the molecules at low temperatures seem to be of importance, as a room-temperature STM study of copper-phthalocyanine on GaAs(110) resulted in significantly different results as the ones found in our study [122].

The findings discussed above establish that the interaction between adsorbed FePc molecules and the supporting GaAs(110) substrate surface is rather weak. The small effects that are due to the remaining interaction are elucidated in the next section.

8.5. Adsorption Induced Effects

In the STM images of individual P-type molecules differences in the relative apparent heights were observed for lobes opposite each other in the [001] direction (c.f. Fig. 8.4). These different apparent heights were attributed to the different local environment experienced by the individual parts of the molecule, caused by the polar nature of the GaAs(110) surface underneath. This explanation in terms of the substrate surface is justified in this section. We present additional spatially resolved $dI/dV(V)$ spectra acquired atop different lobes within individual FePc molecules. Spectra acquired on lobes opposite each other in the [001] direction differ from each other, although they are considered to be related to tunneling involving the very same molecular resonances.

First, we draw our attention to the asymmetry with respect to the (001) plane observed in the STM images of individual FePc molecules (Fig. 8.4). It is emphasized that this asymmetry was observed with different tip apices and for all FePc molecules investigated (24 in total). It is further noted, that the asymmetry was observed both for molecules adsorbed on the *intrinsic* as well as on *n*-doped layer of the GaAs sample. Hence, the asymmetry cannot be a consequence of the built-in electrostatic potential which is present in the *intrinsic* layer of the heterostructure only.

The combined adsorbate/substrate system has no mirror symmetry with respect to the (100) plane, hence the observed asymmetry is not at all surprising. However, the adsorbate in the P-orientation without the substrate does indeed have this symmetry. Hence the asymmetric appearance of the molecule must have its origin in the adsorbate/substrate interaction. We note that similar reductions of the symmetry of Pc molecules upon adsorption have been observed in previous STM studies of SnPc molecules adsorbed on Ag(111) [102] as well as for FePc and CoPc molecules adsorbed on Cu(111) [123, 124].

To investigate this further, we have determined the exact adsorption po-

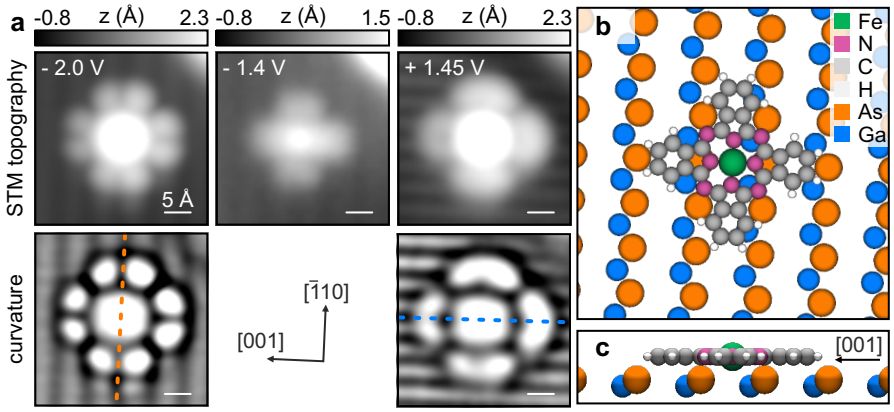

Figure 8.8: Adsorption site determination for FePc on GaAs(110). **a**, Constant current STM topographies (top) and corresponding curvatures (bottom) acquired for different sample biases (as indicated). Left panels: High negative sample bias (-2.0 V, 3 pA). The surface corrugation is determined by the $(A4 + A5)$ surface resonances which both are centered atop As atoms. In the $[001]$ direction, the molecule is found centered in between the As sites. Center panel: STM topography at moderate negative sample bias (-1.4 V, 0.1 pA), showing the cross-like geometry of the molecule with respect to the lattice directions. Right panel: Positive sample bias (+1.45 V, 0.1 pA). The corrugation is determined by the $C3$ surface resonance which is centered above the Ga sites. In the $[\bar{1}10]$ direction, the molecule is found centered in between these sites. **b** and **c**, Top and front view of a ball model for FePc on the top layer of relaxed GaAs(110).

sition and geometry of FePc on GaAs(110) using bias dependent STM imaging. Figure 8.8 shows the site determination for one individual FePc molecule adsorbed in the P geometry. First, the molecule's orientation with respect to the GaAs unit cell is determined by imaging at relative low negative sample bias ($V = -1.4$ V), at which the molecules appearance closely resembles its cross shaped geometry. From Fig. 8.8a center panel, one sees that the arms of the cross-shaped FePc are aligned with the $[\bar{1}10]$ and the $[001]$ directions. Second, the adsorption site is determined by empty and filled state imaging. For the purposes of site determination, only the position of the molecules center with respect to the apparent corrugation of the GaAs(110) surface is considered. For

negative sample bias (Fig. 8.8a left panels, $V = -2$ V), the corrugation runs along the [001] direction and originates from the $A4$ and $A5$ surface resonances. For these two surface resonances, the highest local density of states is around the As atoms. From the alignment observed in the STM image, one can conclude that the FePc molecule is centered between two As atoms in the [001] direction. This site determination is subject to a small uncertainty since the GaAs(110) surface has no mirror plane perpendicular to the [001] direction. For a moderate positive sample bias (Fig. 8.8a right panels, $V = +1.45$ V), the corrugation is rotated by 90° which is a consequence of the $C3$ surface resonance contributing to tunneling. For tunneling into this surface resonance, the maximum of corrugation observed in the STM image is located exactly atop of the Ga atoms. From the STM image, one concludes that the molecule is centered between two Ga atoms in the $[\bar{1}10]$ direction. As the GaAs(110) surface has a mirror plane perpendicular to this direction, this part of the site determination is much more accurate. The resulting adsorption geometry is shown in Fig. 8.8b (top view). The adsorption geometry for FePc in R geometry is determined in the same way.

The geometry of free FePc is planar. As the orbital structure of the free FePc molecule is preserved upon adsorption, the geometries of free and adsorbed FePc molecules have to be identical, or they have to be at least very similar. The STM images indicate, that the plane of the FePc molecule is parallel to the (110) surface plane, maybe with a very small misalignment between both planes. Due to the large size of the molecule even a small misalignment results in large adsorption height differences of equivalent molecular units on GaAs. From low bias images, the size of FePc can be estimated to be about 20 Å (c.f. Fig. 8.8a, center panel). A misalignment of only 3° therefore result in adsorption height differences of about 1 Å. The difference in apparent height observed on lobes opposite to each other in the [001] direction is on the order of 0.5 Å. If this difference would be due to a geometric effect only, one would conclude that the misalignment of FePc is way below 3°. Figure 8.8c shows a model for FePc on GaAs(110) in side view, neglecting a possible (very small) misalignment.

Figure 8.9a shows $dI/dV(V)$ spectroscopy and bias dependent STM images of one individual FePc molecule adsorbed in the intrinsic part of the heterostructure. The data have been acquired on a different molecule and with a different tip apex as those presented in Fig 8.5. The $dI/dV(V)$ data shown here were acquired with lock-in technique (50 mV_{pp}), data points are additionally smoothened over a sample bias range of 25 mV. The $dI/dV(V)$ spectra are spatially resolved, positions at which spectra were taken are indicated in the constant-current STM image shown as inset ($U = -2$ V, $I = 3$ pA). For all spectra, the tip was first moved to the lateral position where the spectra was taken before the feedback loop of the STM was interrupted at a setpoint sample bias of -2 V and a setpoint tunneling current of 3 pA, respectively. Similar to the data shown in Fig. 8.5a, the spectra show peaks well resolved in energy for both negative and positive sample bias, which are attributed to molecular resonances. It is noted that the spectroscopic positions of the peaks observed here differ from those observed in Fig. 8.5. These different spectral positions are a consequence of the different lateral adsorptions positions (across the *p-i-n* diode) of the individual molecules. This effect will be discussed in chapter 9. Here, focus is on $dI/dV(V)$ spectra acquired on lobes opposite each other in the [001] direction within one individual molecule. As indicated by the colored dots in the STM figure shown as inset, one spectra has been acquired at the top-right of the ligand (light red), while a another one has been acquired at the center-left (dark red), respectively. Additional spectra are acquired at the molecules metal center (green), as well as at the bare GaAs surface (blue). The inset-spectra of Fig. 8.9a show the first ligand-centered resonances observed at negative and positive sample bias at a higher spectral resolution. In these spectra, the peak positions of the resonances are indicated by vertical dashed lines. It has to be emphasized that the peak structures observed at different lateral positions of the tip atop the ligand are expected to originate from electronic transport involving the very same molecular resonances. That is because the eigenenergy of a particular molecular orbital *cannot* depend on the lateral position of the microscope's tip at which this energy is probed. On the ligand, these molecular resonances correspond to transport through the a_{1u} symmetric orbital for negative sample bias and the a_{1g} symmetric orbital for positive sample bias

(Sec. 8.4). However, it is immediately apparent that the peak positions observed at different lateral tip positions *differ* from each other. For negative (positive) sample bias, the maximum of the spectra acquired at the top right of the ligand is at about $V = -1.10$ V ($+1.66$ V), while the maximum of the peak of the other spectra is observed at a higher negative (less positive) sample bias of about $V = -1.13$ V (1.59 V). Note that the sequence of the resonances observed at an increasing value of the absolute sample bias *differs* for the different tip positions; for positive sample bias, the ligand centered peak is first observed at the center-left tip position, while for negative sample bias it is first observed at the top-right tip position. Further, the difference between the a_{1u} related resonance peaks observed at negative sample bias is not identical to the difference between the a_{1g} related resonance peaks observed at positive sample bias for different tip positions; the difference observed at positive sample bias ($\Delta V \approx +70$ mV) is about twice the value observed at negative sample bias ($\Delta V \approx -30$ mV; cf. Fig. 8.9a). Finally, also the relative heights of the peaks in $dI/dV(V)$ observed at different lateral tip positions differ from each other. For both the a_{1u} and the a_{1g} related resonance peaks, higher differential conductance is observed at the top right part of the ligand as compared to the center-left one.

Constant-current STM images acquired at sample biases corresponding to the a_{1u} related resonance peak observed in $dI/dV(V)$ are shown in Fig. 8.9b; the images are acquired at sample biases below, at and above a sample bias of $V = -1.1$ V. As established in the previous chapter, the STM image acquired at a sample bias of $V = -1.0$ V (e.g. less negative than the first peak in $dI/dV(V)$ spectroscopy) shows a featureless cross that closely resembles the molecules geometry. At a slightly more negative sample bias (-1.1 V) corresponding to the maximum of the peak in $dI/dV(V)$ acquired at the top-right part of the molecule, the image shows pronounced intra-molecular contrast centered at the ligand. Most remarkably, the contrast observed is asymmetric with respect to the (001) mirror plane; while the nodal plane structure observed at the right side of the molecule corresponds to an a_{1u} symmetry (as expected for the first negative resonance centered on the ligand), the contrast on the left side of the molecule still resembles the featureless cross as observed for a

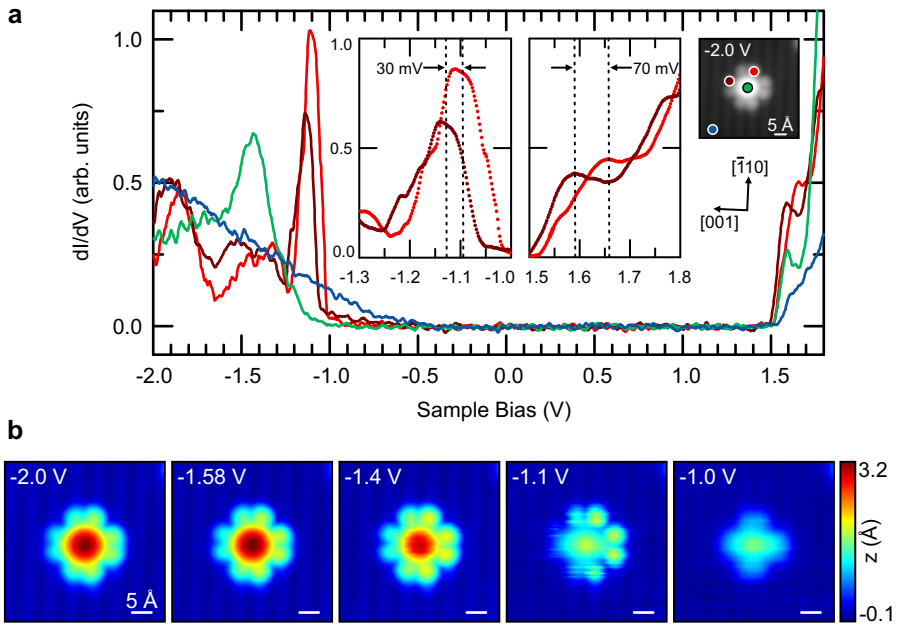

Figure 8.9: Spectroscopy and STM imaging of FePc on GaAs(110). **a**, dI/dV spectra are acquired at the molecules metal center (green line) as well as at its ligand (dark and light red lines), respectively. For comparison, a spectrum acquired at the bare GaAs(110) surface is shown (blue line). The inset-spectra show the ligand-centered resonances at higher spectroscopic resolution, the vertical dotted lines indicate peak positions. The positions at which spectra were taken are indicated by the colored dots in the STM image shown as inset (-2 V, 3 pA). **b**, Bias dependent constant-current STM images recorded at tunneling currents of (from left to right) 3 pA, 3 pA, 3 pA, 0.4 pA, and 0.1 pA, and at sample biases as indicated.

less negative sample bias of $V = -1.0$ V. At a higher negative sample bias of $V = -1.4$ V beyond the spectral positions of both peaks in $dI/dV(V)$ spectroscopy, the contrast observed on the ligand corresponding to the a_{1u} orbital is observed on both sides of the molecule (additionally at this higher negative sample bias a metal centered resonance is observed, as it is expected from $dI/dV(V)$ spectroscopy). However, also at this higher negative sample bias, the ligand centered resonance is asymmetric with respect to a (001) mirror plane; the relative apparent heights of lobes

opposite to each other in the [001] direction are different, the lobes on the molecules right side appear higher as the one on its left side. This picture does not change for images acquired at still higher negative sample biases of $V = -1.58$ V and $V = -2.0$ V, respectively. Hence, for an increasingly negative sample bias both in spectroscopy and in imaging the a_{1u} symmetric ligand centered resonance is first observed on the molecules right side.

From the experimental data, the following conclusions can be drawn. (i) It is once more emphasized that the resonances observed in $dI/dV(V)$ spectra acquired at different lateral positions atop the ligand are related to transport involving the same molecular resonances. This is also corroborated by the STM images shown in Fig. 8.9b. Since the images recorded at a sample bias of $V = -1.1$ V (corresponding to the peak observed at the top-right tip position only) as well as at $V = -1.4$ V (more negative than both peaks observed atop the ligand) both show the same nodal plane structure of the a_{1u} orbital, they both have to be related to tunneling involving the same molecular resonance. (ii) It is noted that a lateral variation of the centroid of $dI/dV(V)$ peak structures has recently been reported for pentacene molecules decoupled by an ultrathin insulating layer from a metallic substrate [125]. There, the lateral variation of the centroid was explained by a suppression of elastic tunneling due to local symmetry considerations, particularly by a different overlap between local s and p like states of the molecule with an s like tip state. This model requires the spatial variation of the centroid to have the same symmetry as the corresponding molecular resonance. Accordingly, such model cannot explain the spatial variation observed here, as the resonance observed at negative sample bias is of a_{1u} symmetry, which, for the given orientation of the molecule, is in particular left-right symmetric. (iii) TIBB effects can be considered. TIBB is known to spread spectroscopic features. If the magnitude of this effect would be different for different tip positions above the ligand, one indeed would observe one and the same molecular resonance at different sample biases for different tip positions. However, TIBB effects are *not* expected to reverse the sequence at which molecular resonances are observed for different polarities of the sample bias as it is observed in our experiments.

Further, on p-type GaAs, the magnitude of TIBB is large for negative sample bias and is small for positive sample bias, see chapter 4. In our experiments however we observe the opposite, as the shift at positive sample bias is about twice as large as the one at negative sample bias. Hence, TIBB effects alone can be ruled out as an explanation of the observed tip-position dependence of molecular resonances. (iv) The apparent height of a particular feature in an constant-current STM image at a particular sample bias is determined by the decay of the corresponding electronic states into the vacuum (that is, towards the tip). From the $dI/dV(V)$ spectra, it is apparent that for a sample bias of $V \leq -1.2$ V the ligand centered state is accessible to tunneling on both sides of the molecule. The difference in apparent height of lobes opposite each other in the [001] direction observed in STM images at $V \leq -1.2$ V is therefore attributed to a different decay of the local wave functions atop the ligand into vacuum. The wave function atop the left part of the ligand seems to decay faster into vacuum as the one on the right side. Such could be due to a (spatial) rearrangement of molecular orbitals due to its asymmetric overlap with fully occupied or empty dangling bond states of the GaAs surface.

In summary, the asymmetry observed in the STM images of FePc molecules adsorbed on GaAs(110) can be rationalized from symmetry considerations. However, so far the tip-position dependence of the resonances observed in STS is not fully understood.

9. A Diode's built-in Potential used as a Local Gate

In this chapter we exploit the spatial variation of a diode's built-in electrostatic potential as a means to tune the spectroscopic features of individual iron-II-phthalocyanine molecules. As across a *p-i-n* diode the electrostatic potential varies while the Fermi level stays constant, the molecular resonances can be tuned with respect to the Fermi level for different lateral adsorption positions of the molecule across the diode. The shift of the molecular resonances is observed from scanning tunneling spectroscopy.

9.1. Introduction

In the field of molecular electronics, one aims at the control of the electronic conductance through an individual molecule, see, e.g. Refs. [90, 126]. From the experimental point of view, the electronic conductance through an individual molecule can be measured either by break-junction based experiments or by scanning probe based experiments. In break-junction based experiments, a single molecule resides in a small gap that separates two metal wires. Such gap is e.g. fabricated by electromigration and the wires separated serve as electrodes applying a bias voltage to a single molecule. In scanning probe experiments, the microscope's tip and the substrate surface serve as electrodes to the single molecule placed in the tunneling gap between.

Since the electronic conductance through a single molecule is intimately connected to the charges residing on the latter [127], the control of the

molecules charge state is highly desirable. Such control can be achieved in a three-terminal device in which the energy levels of the molecule can be shifted relative to the Fermi levels in the electrodes. A macroscopic realization of a three-terminal device is a field effect transistor (FET) [128]. In a FET, the electronic conductance through a narrow channel between source and drain electrodes is controlled by the number of free charge carriers residing in the channel. The latter is, in turn, controlled by the bias voltage applied to a gate electrode. On the single-molecule level, true three-terminal devices have been realized in break-junction experiments, which have the advantage that electromigration techniques can be combined with techniques of micro-patterning of the sample (e.g., optical lithography) [128]. However, break-junction based experiments typically suffer from a lack of knowledge of the exact configuration of the molecule in the junction (e.g., geometry and bonding to the electrodes), and data analysis has typically to be performed in terms of statistics on a large number of sample devices. Scanning probe experiments, on the other hand, offer unprecedented control over the molecular arrangement within the junction, but typically lack a third electrode which could serve as a gate. In order to nonetheless change orbital energies with respect to the Fermi level of the substrate in an STM setup, several different approaches have been taken in the past. Substrate surfaces of different work-functions [103, 129, 130] as well as electrostatic fields emanating from localized charged entities such as adatoms [115, 131], surface defects [132, 133] or dangling bonds [134] spatially located close to individual molecules or adatoms have been employed to tune orbital energies of the latter. On semiconducting surfaces, TIBB has been exploited as a possibility to tune orbital energies [120, 135, 136], and Loth [12] used the electrostatic field within an active *p-i-n* diode to gate dopant atoms buried in the diode's *intrinsic* layer.

Here we exploit the possibility to tune molecular orbital energies via the molecule's lateral adsorption position across a *p-i-n* diode. In the absence of any adsorbate-substrate interaction, the unperturbed energy levels of an adsorbate are aligned with respect to the vacuum level of the sample, which is called the vacuum level alignment rule. Across a *p-i-n* diode, in equilibrium the Fermi level is constant throughout the sample, but the

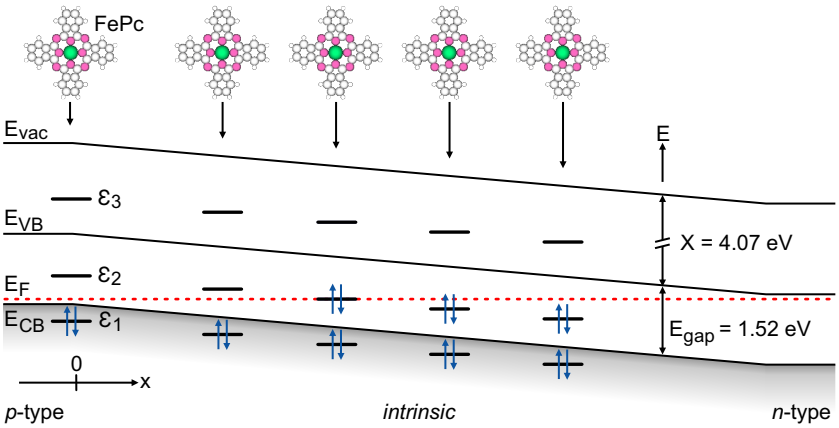

Figure 9.1: Tuning of orbital energies via a diode's built-in potential. With lateral position x across a p-i-n diode, the vacuum level (E_{vac}) and valence (E_{VB}) and conduction band edges (E_{CB}) shift w.r.t to the constant Fermi level E_{F}. The vacuum level alignment rule predicts orbital energies of an adsorbate (FePc molecule, labeled ϵ_{i}) to be aligned with respect to the vacuum level of the sample. Eventually, a molecular orbital crosses the Fermi level of the sample and changes its (average) occupation.

vacuum level changes with lateral position across the diode. Hence, the energy levels of a (non-interacting) molecule change their position with respect to the Fermi level of the sample as the molecule is adsorbed at different lateral positions across the diode. That is, the lateral position of adsorption of the molecule acts like an *effective* gate voltage to the molecule. This concept is sketched in Fig. 9.1.

By now it is well known that the vacuum level alignment rule rarely applies to real adsorbate/substrate system as in any real system there has to be some degree of adsorbate/substrate interaction, otherwise the adsorbate simply would not condense on the substrate surface (see, e.g. [137, 138]). For example, any dipole moment between adsorbate and substrate will shift the energy levels of the substrate and will thus invalidate the vacuum level alignment rule. Such dipole moment for e.g. may be induced by a permanent charge transfer between the adsorbate and the

substrate [137] or by a local push-back of the electrons into the substrate due to the presence of the adsorbate via Pauli repulsion [139].

Here, we present the results of an STM experiment probing the energy levels of individual FePc molecules adsorbed at different lateral positions across the (110) surface of a GaAs-based *p*-*i*-*n* diode. In chapter 8, FePc molecules adsorbed on GaAs(110) have been established to be a weakly interacting molecule/substrate system. In analogy to the scheme depicted in Fig. 9.1, we observe resonance peaks of the molecules which are shifted for molecules adsorbed at different lateral positions. Resonances observed on molecules close to *n*-type GaAs are shifted downward in energy with respect to the resonances observed on molecules close to *p*-type GaAs. That is, the direction of the shift of the resonances follows the built-in potential of the *p*-*i*-*n* diode and hence, the general trend of the shift is correctly predicted by the vacuum level alignment rule, as is expected for a weakly interacting adsorbate/substrate system.

9.2. Adsorbate and Substrate System

The adsorbate (FePc) and the substrate system [the (110) surface of a *p*-*i*-*n* diode] have been introduced in detail in Secs. 8.1 and 8.2. In particular, FePc adsorbed on GaAs has been shown to only weakly interact with the substrate and thus to retain its sequence of orbitals of the free molecule. In STS of FePc on GaAs distinct peaks in $dI/dV(V)$ spectroscopy have been observed for negative and positive sample biases, which have been attributed to resonant tunneling processes involving individual molecular orbitals. The layout of the *p*-*i*-*n* diode used as substrate basically consists of a 200 nm wide nominally undoped (*intrinsic*) layer of GaAs sandwiched between degenerate *n*- and *p*-type doped layers. The position of the Fermi level w.r.t. to the vacuum level (and to the conduction and valence band edges, respectively) is constant within the *n*- and *p*-doped layers. At the high dopant concentrations and low temperatures used in our experiment, inside the doped layers the position of E_F is equal to the ionization energies E_A of the respective dopant

atoms [35]. The ionization energies E_A of Si donors and Mn acceptors in GaAs are 5.8 meV and 113.1 meV, respectively [140]. Hence, the Fermi level is located about 6 meV below the conduction band edge in the *n*-doped layer and 113 meV above the valence band edge in the *p*-doped layer, see Fig. 9.1. It is noted that the Fermi level position in highly Mn doped GaAs is a topic of ongoing research; by now it is believed that the Fermi level is indeed located about 100 meV above the valence band edge [109, 141, 142]. The change of $[1.518 - (0.113 + 0.006)]$ eV ≈ 1.4 eV in the relative band-edge positions across the diode is accompanied by an electrostatic field E_{diode}. This field will (mainly) drop off in the 200 nm wide *intrinsic* layer sandwiched between the *n*- and the *p*-doped layers (cf Fig. 9.1). Hence, E_{diode} can be calculated:

$$E_{\text{diode}} = -\frac{1.4\ \text{V}}{200\ \text{nm}} = -7\ \frac{\text{mV}}{\text{nm}} \tag{9.1}$$

That is, in the *intrinsic* layer the distance between the vacuum level and the Fermi level changes at a rate of 7 mV per nanometer. If the vacuum level alignment rule applies, the orbital energies of the adsorbate are aligned with respect to the vacuum level position of the substrate. That given, the orbital energies of FePc adsorbed at different lateral positions across the *p-i-n* diode are shifted with respect to each other; the lateral position of adsorption, x, acts like an effective gate voltage V_{gate}. In the *intrinsic* layer, V_{gate} can be expressed as

$$V_{\text{gate}} = E_{\text{diode}} \times x \tag{9.2}$$

where x has arbitrarily been set to zero at the interface between the *p*-doped and the *intrinsic* GaAs layers (cf Fig. 9.1).

Here, we probe the electronic transport through resonant levels of FePc from STS at negative sample biases. These resonances have previously been shown to involve transport through an a_{1u} symmetric ligand centered orbital as well as an a_{1g} symmetric metal centered orbital, see Sec. 8.4.

9.3. Gating via a built-in Potential

Figure 9.2 shows $dI/dV(V)$ spectra of three individual FePc molecules adsorbed at three different lateral positions across the *intrinsic* layer of the *p-i-n* diode, namely at $x = 13$ nm (blue line), at $x = 100$ nm (green line) and at $x = 190$ nm (red line, see Fig. 9.1 for the definition of the zero point of x). The inset figure shows the same spectra but for a larger bias range. All spectra have been acquired on the ligand of the individual molecules using the same tip apex. It is immediately apparent that all three spectra show a similar peak structure but are shifted with respect to each other: With increasing lateral position x, the resonance peaks are observed at higher negative sample biases. As a guide to the eye, the first peak of each spectra has been indicated by a vertical dashed line. In order of ascending x values, these peaks are observed at about -1.53 V (13 nm), -1.60 V (100 nm) and -1.85 V (190 nm), respectively.

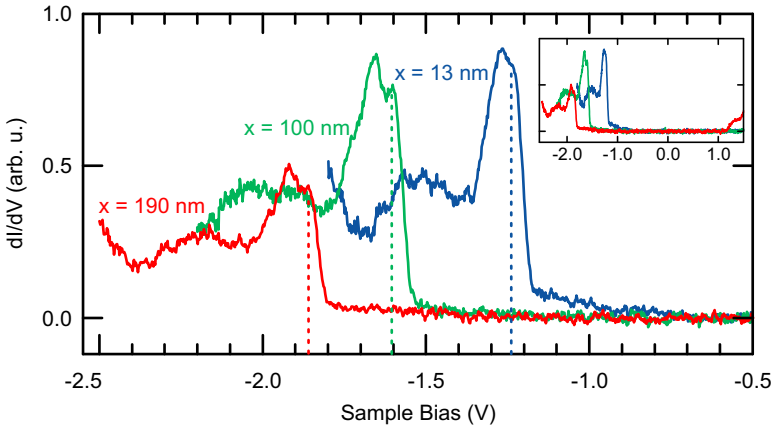

Figure 9.2: Adsorption-position dependence of molecular resonances. $\mathrm{d}I/\mathrm{d}V$ spectra are acquired on three individual FePc molecules adsorbed at different lateral positions x across the 200 nm wide *intrinsic* layer of a *p-i-n* diode (x values as indicated). All spectra have been acquired at the FePcs ligand using the same tip apex. The spectra show a very similar peak structure, but are shifted with respect to each other. The inset shows the same spectra but for a larger sample bias range.

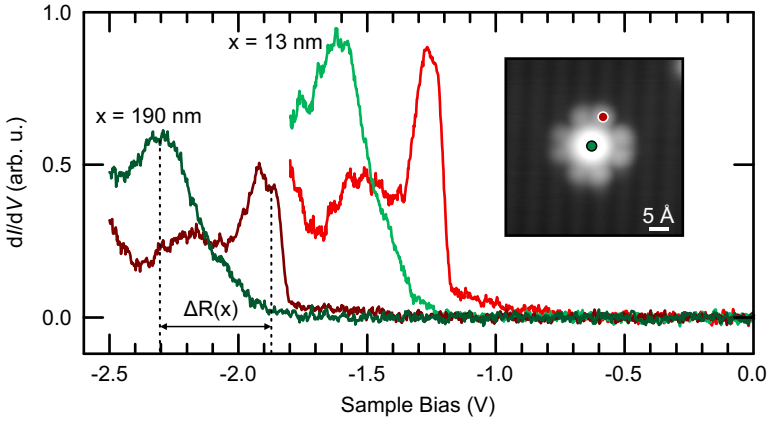

Figure 9.3: Adsorption-position dependence of molecular resonances. $\mathrm{d}I/\mathrm{d}V$ spectra acquired on the metal center (green) as well as on the ligand (red, see inset-figure for positions; $U = -2$ V, $I = 3$ pA), of two different FePc molecules located at two different lateral positions of $x = 13$ nm (bright lines) and of $x = 190$ nm (dark lines). For one individual molecule located at x, $\Delta\mathrm{R}(x)$ is the difference in sample bias at which resonances are observed on the molecules metal-center and on its ligand.

Figure 9.3 shows for the two molecules closest to the n- and p-doped layers spatially resolved $dI/dV(V)$ spectroscopy. The spectra were taken at the individual molecule's ligand (dark and bright red lines), as well at its metal center (dark and bright green lines). In similarity to the shift observed in the spectra acquired on the ligand (Fig. 9.2), the resonance peaks observed on the metal centers are shifted with respect to each other when comparing molecules adsorbed at different lateral positions. While the metal-centered peak of the molecule adsorbed close to the p-doped layer ($x = 13$ nm) is observed at a bias voltage of about $V = -1.20$ V, the one of the molecule adsorbed close to the n-doped layer ($x = 190$ nm) is observed at a bias voltage about $V = -1.88$ V. That is, *both* metal and ligand centered states are shifted to higher negative sample bias for an increasing adsorption position x.

To systematically investigate this shift, 21 individual FePc molecules adsorbed at 21 different lateral positions across the p-i-n diode have been

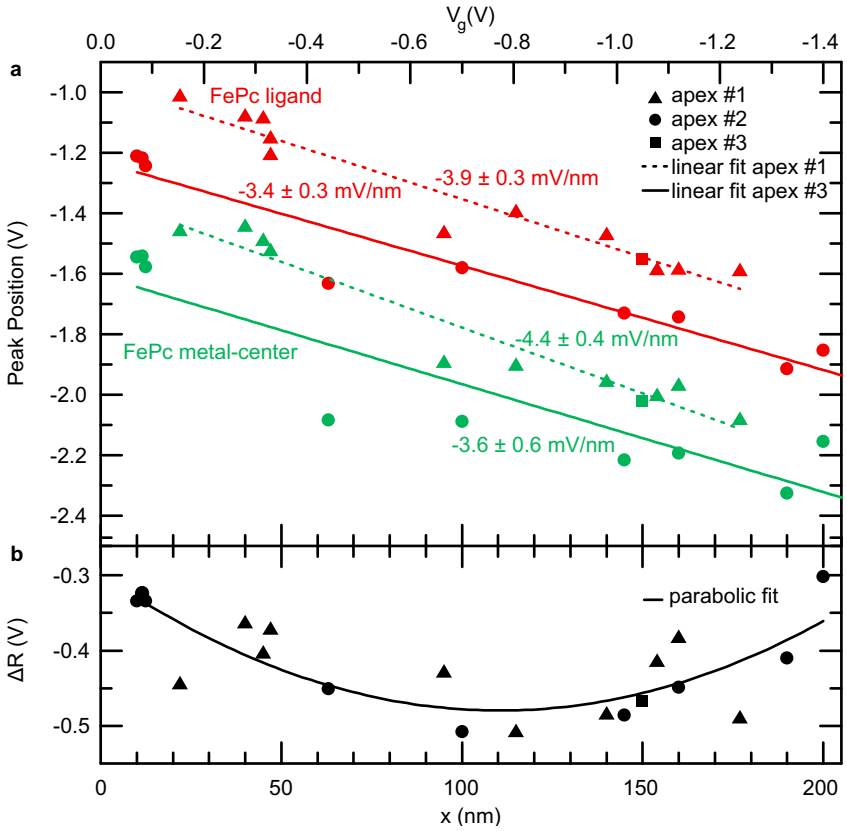

Figure 9.4: Adsorption-position dependence of molecular resonances. **a**, Spectroscopic position of the first molecular resonances observed at negative sample bias at the molecules ligand (red symbols) and at its metal center (green symbols) versus the lateral position of adsorption of the molecule x (bottom axis), as well as versus the corresponding effective gate voltage V_{g} (top axis). Data are plotted for three different tip apices labeled #1 to #3. With increasing distance x (more negative V_{g}), molecular resonances are observed at higher negative sample biases. **b**, Difference between spectroscopic positions of ligand- and metal-centered states $\Delta\mathrm{R}$ versus lateral position of adsorption x. The solid and dashed lines in (a) and (b) are linear and parabolic fits, respectively.

probed by STS. The corresponding data are shown in Fig. 9.4. The spectroscopic position of the first peak observed in STS at negative sample bias at the molecules ligand (red symbols) and at its metal-center (green symbols) versus the lateral adsorption position x of the respective molecule (bottom axis), as well as versus the effective gate voltage V_g (top axis) are shown in Fig. 9.4a. The top axis has been produced by conversion of lateral position into effective gate voltage, using Eq. 9.2. The data have been acquired with three different tip apices, labeled #1 to #3, as is indicated by the different symbols. It is immediately apparent that both ligand- and metal-centered peaks are observed at higher negative sample biases for an increasing lateral position x (more negative potential V_g). That is, the orbital energies are shifted with respect to the Fermi level of the sample, as it is expected from the considerations given above. Data acquired on the individual parts of the molecules and with different tip apices have been fitted separately (cf Fig. 9.4a, dashed and solid lines). From the linear fits to the data acquired with tip apex #1, we extract slopes of -3.9 ± 0.3 mV/nm (ligand) and -4.4 ± 0.4 mV/nm (metal-center), respectively. For apex #3, we extract -3.4 ± 0.4 mV/nm (ligand) and -3.6 ± 0.6 mV/nm (metal-center), respectively. One observes that the data acquired with the different tip apices are shifted with respect to each other; for tip apex #1 (dashed lines), the resonance peaks are observed for less negative sample biases as for apex #3 (solid lines). However, the slopes extracted from measurements acquired with different tip apices are almost identical. The observed overall shift could be due to different work functions of the different tip apices (that is, due to different strenght of the TIBB for different tip apcies). For each individual apex, the slopes are identical within the margin of the error. If we take the numerical average of the four slopes, we find a value of -3.8 mV/nm. From the vacuum level alignment rule, one expects a slope of -7 mV/nm, see Eq. 9.1. Hence, from our experimental findings we conclude that the vacuum level alignment rule *qualitatively* predicts the shift of molecular resonances observed in our experiments, but is not sophisticated enough to *quantitatively* explain the magnitude of the observed shift. This findings are in accordance with a weakly interacting molecule/substrate system.

For the known orbital energies of FePc and the band structure of GaAs, the vacuum level alignment rule predicts orbital energies of FePc to be located within the fundamental band gap of the semiconducting substrate [113]. That given, one initially expects these levels to cross the Fermi level of the substrate as one considers molecules adsorbed at different lateral positions across the *p-i-n* diode (cf. Fig. 9.1). When a molecule changes its charge state as it crosses the Fermi level, a permanent dipole moment is established which should, in fact, result in an abrupt change of the level alignment. Further, for a charged molecule the electronic transport characteristics are expected to be considerably different as for a neutral one. For e.g., Coulomb charging-energies have to be taken into account when considering transport through an orbital (partially) occupied by electrons [130]. From that, the question arises if the resonances observed on molecules adsorbed at different lateral adsorption positions are related to transport involving the same molecular orbitals (which are shifted w.r.t. each other by the effective gate voltage), or if these resonances correspond to transport through different orbitals (as the FePc's charge state has changed somewhere along x). Figure 9.4b shows the *difference* between the sample biases at which (for one individual molecule located at x) the first peak in STS is observed (at negative sample bias) at the FePcs ligand and at its metal-center, $\Delta\mathrm{R}(x)$. For clarity, $\Delta\mathrm{R}$ is indicated in Fig. 9.3. If FePc does not change its charge state, the FePc's transport characteristics will be identical for molecules adsorbed at different lateral positions x, except for an overall shift. In this chase, $\Delta\mathrm{R}(x)$ is expected to be constant in x. If, however, the molecular charge state changes, $\Delta\mathrm{R}(x)$ is expected to have one particular value of $\Delta\mathrm{R}$ that corresponds to the neutral molecule and a different one that corresponds to the charged molecule. In this case, $\Delta\mathrm{R}(x)$ is expected to look like a step-function (here, multiple charge states of FePc are excluded as these states are expected to be unfavorable due to the large Coulomb-energies attributed). In addition, one has to consider TIBB, which may also influence $\Delta\mathrm{R}(x)$. That TIBB effects are indeed not negligible in the intrinsic region has been demonstrated in Sec. 8.2. The effect of TIBB is to spread spectroscopic features along the voltage axis and the magnitude of this effect is expected to be strongest in the center of the *intrinsic* region, where the overlap between the (macroscopic part of the) tip and

the doped layers is minimal. In the experiment, $\Delta R(x)$ is found to have maximal values (of about -0.3 V) at both ends of the *intrinsic* layer, and to have a minimum (of about $-0.5\,V$) in between, somewhere around the center of the *intrinsic* layer (at about 115 nm). The lateral dependence of $\Delta R(x)$ is highlighted by a parabolic fit to the data in Fig. 9.4b (solid line). Hence, the observed spatial dependence of $\Delta R(x)$ is fully consistent with transport including one and the same molecular resonances (no permanent change in charge state of the molecule) plus the spatial varying effects of TIBB. That indeed the charge state of the molecule does not change for changing x values is also corroborated by STM images of the individual molecules. Localized charges on the GaAs(110) surface are typically surrounded by (radial-symmetric) smooth changes of the apparent height, which are caused by the band-bending induced by the localized charge. Here, no such change of the apparent hight of the GaAs lattice in the close vicinity to FePc molecules was observed, indicating a neutral charge state of the molecules.

In conclusion, orbital energies of FePc molecules adsorbed on the *intrinsic* layer of a *p-i-n* diode have been probed by STS. The orbital energies are tuned by the diodes built-in potential, via the lateral adsorption position of the molecule across the diode. The shift of molecular resonances can qualitatively be explained in the framework of the vacuum level alignment rule.

10. Fixing the Energy Scale in Scanning Tunneling Microscopy on Semiconductor Surfaces

The research presented in this chapter is to large extent published in Physical Review Letters [143]. Parts of the text are identical to the publication[1].

In scanning tunneling experiments on semiconductor surfaces, the energy scale within the tunneling junction is usually unknown due to tip-induced band bending. Here, we experimentally recover the zero point of the energy scale by combining scanning tunneling microscopy with Kelvin probe force spectroscopy. With this technique, we revisit shallow acceptors buried in GaAs. Enhanced acceptor-related conductance is observed in negative, zero, and positive band bending regimes. An Anderson-Hubbard model is used to rationalize our findings, capturing the crossover between the acceptor state being part of an impurity band for zero band bending, and the acceptor state being split off and localized for strong negative or positive band bending, respectively.

10.1. Introduction

Since its invention, the STM has been widely used to study semiconductor surfaces. The qualitative interpretation of such studies can be obscured by the presence of tip-induced band bending TIBB(V), i.e., by the bias-dependent shift of all electronic states beneath the microscope's

[1] G. Münnich et al., *Physical Review Letters* **111**, 216802 (2013).

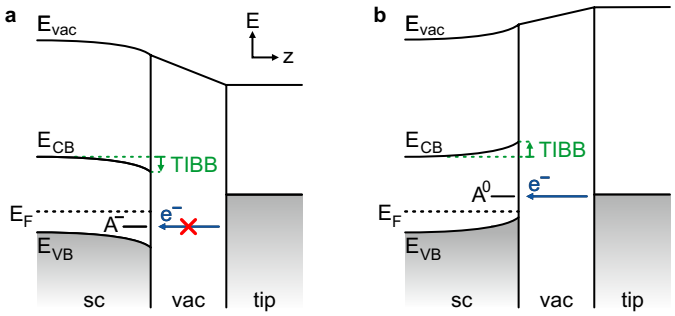

Figure 10.1: Energy diagram of a semiconductor-vacuum-probe tip tunneling junction in the presence of tip-induced band bending (TIBB). **a**, Negative (downward) TIBB. An electronic state labeled A is TIBB-shifted below the Fermi level of the sample. It becomes permanently occupied and cannot directly contribute to the electronic transport within the junction. **b**, Positive (upward) TIBB. The state A is shifted above the Fermi level of the sample, is neutral and contributes to the tunneling current between tip and sample. The sample bias in (a) and (b) is identical; the polarity of the band bending determines whether or not the state A contributes to tunneling.

tip (cf. chapter 4) [9, 42, 144]. If shifted across the Fermi level, TIBB(V) changes the average occupation of an electronic state, which, in turn, determines if this state contributes to the electronic transport within the junction (Fig. 10.1) [120, 132, 135, 145–147]. As discussed in chapter 4, TIBB(V) is a monotonic function of the sample bias, shifted around zero bias by V_{CPD}. In STM, V_{CPD} is, with few exceptions, unknown [51, 148]. Hence, in the relevant bias range not even the polarity of TIBB(V) is known (Fig. 10.1). In this context, the conductance spectra of shallow acceptors buried in III–V semiconductor hosts remained a puzzle unsolved for almost two decades; depending on the sign of the band bending assumed or inferred from scanning tunneling spectroscopy, conductance is explained either due to tunneling of electrons into empty acceptor states (positive TIBB) [149], or due to a modification of the tunneling barrier by the occupied acceptor (negative TIBB) [150], or by the empty acceptor state being in resonance with an impurity band (zero TIBB) [151]. Although the need for an exact value of the CPD has clearly been recog-

nized [12, 52, 150, 151], bare STM-based methods used so far seem not to be sufficient to resolve this puzzle.

To this end, we combine STM on a semiconducting surface with Kelvin probe force spectroscopy, which allows an independent and direct measurement of the CPD, which fixes the polarity of TIBB(V) for all voltages. With this combination, we revisit the shallow acceptor Zn buried in GaAs [46, 149–152].

10.2. Experimental Details

The experiments were performed by means of the combined STM/AFM introduced in chapter 6.

The magnitude of TIBB(V) among others depends on the absolute tip-sample distance (cf. chapter 4). To record all current I versus sample bias V spectra and differential conductance ($\mathrm{d}I/\mathrm{d}V$) maps at the same absolute tip-sample distance, we first opened the feedback loop of the STM at $V = 1.8$ V, $I = 20$ pA, with the tip located away from any acceptor or defect, and then moved the tip to the lateral position where spectra or $\mathrm{d}I/\mathrm{d}V$ maps were taken. $I(V)$ spectra are averaged over each 10 single spectra, acquired along a line in a specific sample region. $dI/dV(V)$ spectra are numerically derived from the $I(V)$ data, with data points averaged over a bias range of 50 mV. For $\mathrm{d}I/\mathrm{d}V$ maps, we used the lock-in technique, adding a small sinusoidal *ac* signal of 50 mV peak-to-peak at 166 Hz to the *dc* sample bias.

For the KPFS data shown here, the tip was retracted by $\Delta z = 5$ Å once the feedback loop of the STM was interrupted at $V = 1.8$ V, $I = 20$ pA with the tip located away from any acceptor or defect (except where stated otherwise). For such increased distance, the CPD measurements are not influenced by atomic scale variations of the sample surface, but depend only on the long-range electrostatic interaction between tip and sample [27], see chapter 5. Moreover, at such increased distance, the

tunneling current is zero, such that we can exclude any influence of the tunneling current on the KPFS signal (Sec. 5.2). As oscillation amplitudes (A) of the qPlus force sensor we used 1.2 Å, 2.5 Å, and 0.5 Å, for measurements with tip apices labeled #1, #2, and #3, respectively.

The apex of the microscope's tip was treated by controlled indentations into the (111) surface of the Cu single crystal mounted on the dual sample holder next to the GaAs sample (see chapter 7).

As samples, we use commercially available Zn-doped GaAs wafers [81, 82]. Sample preparation is performed as described in chapter 7; GaAs samples are cleaved inside the vacuum chamber to expose the (110) surface and are transferred within less than one minute into the cold STM/AFM at a background pressure better than 1×10^{-9} mbar.

10.3. Substituional Zn Impurities in GaAs

The GaAs samples used in our experiments are doped with Zn. In the periodic table of elements (Fig. 10.2) Zn is located left of Ga. Hence, Zn impurities substituting for Ga atoms act as electron acceptors in the GaAs host crystal.

As discussed by A. Richardella, the formation of the acceptor level of substitutional Zn can be understood from the hybridization of the valence state of isolated zinc[2] with the dangling-bond state of an ideal gallium vacancy (V_{Ga}), see Fig. 10.3a [153, 154]. When the Ga vacancy hybridizes with an isolated Ga atom, the derived bonding (antibonding) state will be located within the valence (conduction) band of the host semiconductor. As Zn is less electronegative than Ga, the valence state of Zn is higher in energy than the one of Ga. Accordingly, the bonding V_{Ga}−Zn hybrid (red line in Fig. 10.3a) is not pushed down into the va-

[2]The valence level of isolated Zn is the sp^3 hybrid derived from the zinc's filled $4s$ and empty $4p$ orbitals.

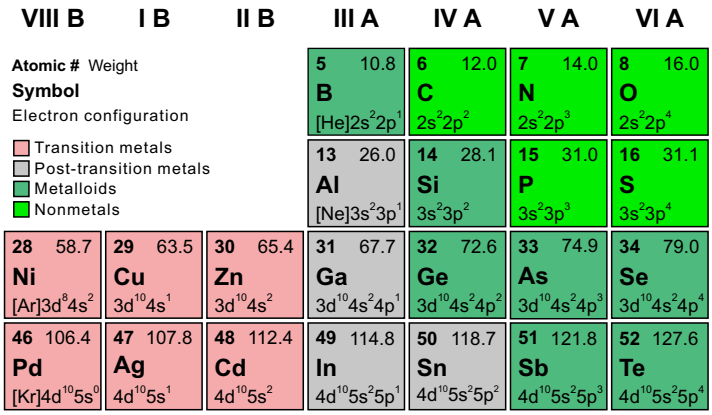

Figure 10.2: Relevant section of the periodic table of elements. Since zinc is located left of gallium, zinc impurities substituting for gallium host atoms act as electron acceptors in gallium arsenide. The $3d$ shell of zinc is completely filled with 10 electrons, hence its $3d$ levels play no role in the bonding of substitutional zinc in gallium arsenide. Note that closed shells are given only for the first element of each row.

lence band of the semiconductor but is located *above* the valence band edge (Fig 10.3a). As the d shell of Zn is fully occupied with 10 electrons and is located deep below the valence band edge of GaAs (-12 eV [154]), the d levels of Zn can be considered as core-levels which do not participate in the bonding. This situation is much different for other transition metal atoms such as Fe or Mn which have only partially filled d shells [153]. The ionization energy (that is, the position of the bonding V_{Ga}-Zn hybrid above the valence band edge) of a single Zn acceptor in GaAs is $E_{\mathrm{A}} = 31$ meV [156]. Per definition, shallow acceptors are defined by ionization energies of $E_{\mathrm{A}} \ll 100$ meV [35]. Hence, substitutional Zn is a shallow acceptor in GaAs.

After having considered the localized electronic state introduced by a *single* Zn acceptor into the band gap of GaAs, we now consider the electronic interaction of these states as will take place for high acceptor concentrations. As specified by the supplier, our samples are doped at an

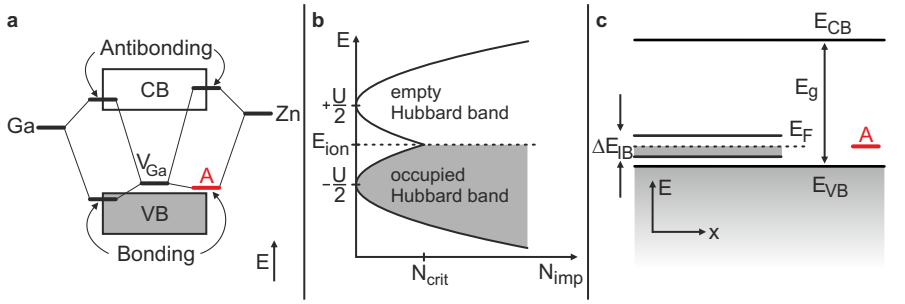

Figure 10.3: Electronic states and interactions of Zn acceptors in GaAs. **a**, Bonding and antibonding states formed by hybridization of an ideal gallium vacancy (V_{Ga}) with a Ga host atom and a Zn impurity. After Ref. [153]. **b**, The interaction of a large number N_{imp} of impurity states can be described in terms of Hubbard bands. The lower band is completely filled (with 1 electron per state on average), the upper one is completely empty. For $N_{\mathrm{imp}} \geq N_{\mathrm{crit}}$, both bands are merged and the system behaves as a metal. After Ref. [155]. **c**, Band diagram. The Zn-dopant-induced impurity band of width ΔE_{IB} is centered around the ionization energy of an individual Zn acceptor (labeled A). The Fermi level is centered within this half-filled band.

average concentration of $N_{\mathrm{A}} = 1 \times 10^{19}$ cm^{-3}. If the Zn acceptors were to occupy sites of a simple cubic lattice, the nearest-neighbor acceptor distance would be $N_{\mathrm{A}}^{-1/3} = 46$ Å. As the acceptors are distributed on random (substitutional) positions within the GaAs host crystal, we expect their *average* nearest-neighbor distance to be ≈ 46 Å. For such high impurity concentration, the acceptor levels will overlap and an *impurity band* will be established (Fig. 10.3c). The width of this impurity band ΔE_{IB} can be estimated from the Coulomb interaction between adjacent acceptors separated by an (average) distance of $N_{\mathrm{A}}^{-1/3}$ as [35]

$$\Delta E_{\mathrm{IB}} \cong \frac{e^2}{4\pi\epsilon\epsilon_0 N_{\mathrm{A}}^{-1/3}} = 24 \text{ meV}. \tag{10.1}$$

The impurity band is centered 31 meV above the valence band edge, that is, around the ionization energy E_{A} of the isolated acceptor. As each Zn acceptor contributes one hole to the impurity band, the impurity band

is half filled and the Fermi level is centered within. This situation is sketched in Fig. 10.3c.

It is noted that some precaution is in order when referring to an impurity *band*. As the dopant atoms are randomly (that is, non-periodically) distributed in the GaAs crystal, no periodic band structure calculation can be used, and no sharp band edges are present [35]. The electronic interaction of randomly distributed impurity states is more correctly described in terms of *Hubbard bands*, see Fig. 10.3b. In a Hubbard band, each electronic state can only be occupied by 1 electron on average (as instead of 2 for a conventional band), and the bands are split into a lower (occupied) and an upper (empty) Hubbard band both separated by an excitation gap of width U. The separation between the bands decreases for increasing impurity concentration N_{imp}, until for a critical concentration N_{crit} the excitation gap vanishes as the Hubbard bands merge. This situation is referred to as *Mott transition*. For $N_{\mathrm{imp}} \geq N_{\mathrm{crit}}$, electrons can be excited at no cost of energy and hence the system behaves metallic. The critical concentration of impurities can be estimated from the *Mott criterion*, which demands adjacent acceptor states to overlap[3]

$$N_{\mathrm{crit}}^{1/3} \times a_{\mathrm{B}}^{*} \cong 0.24 \tag{10.2}$$

where a_{B}^{*} is the effective Bohr radius of the impurity [35]. The effective Bohr radius of an acceptor in a tetrahedral semiconductor (e.g., GaAs) is challenging to calculate as the valence bands are degenerate at the Brillouin zone center. An approximative value is given by

$$a_{\mathrm{B}}^{*} \approx \frac{4\pi\epsilon_0\hbar^2}{me^2}\epsilon\gamma_1 \tag{10.3}$$

where m is the mass of the free electron and γ_1 is a dimensionless (Luttinger) parameter [157]. Using a value of $\gamma_1 = 6.9$ for GaAs [157], we find an effective Bohr radius of a shallow acceptor of $a_{\mathrm{B}}^{*} = 47$ Å. Hence, from the Mott criterion (Eq. 10.2) one expects the Mott transition to occur at a critical impurity concentration of $N_{\mathrm{crit}} = 1.33 \times 10^{17}$ cm^{-3}. This value

[3] If the impurities were to occupy sites of simple cubic lattice, the Mott criterion would simply be $2a_{\mathrm{B}}^{*} = N_{\mathrm{crit}}^{-1/3}$. However, the impurities are randomly distributed.

fits well to the experimentally observed onset of metallic behavior of Zn-doped GaAs at an acceptor concentration of $N_{\mathrm{crit}} = 7 \times 10^{17}$ cm^{-3} [158]. The samples used in our experiments ($N_{\mathrm{A}} = 1 \times 10^{19}$ cm^{-3}) are doped at a concentration well above N_{crit}. Hence, the Hubbard bands are merged in our samples and our samples behave metallically even at low temperatures.

10.4. STM Imaging of Zn Acceptors Buried in GaAs

Before we will focus on the electronic transport through buried Zn acceptors, we will briefly review its topographic contrast as it is observed in STM imaging.

Figure 10.4 shows an atomically resolved constant-current STM image of the (110) surface of Zn-doped GaAs acquired at a sample bias of +1.5 V. At this particular sample bias, the GaAs lattice is visible as parallel stripes running along the $[\bar{1}10]$ direction. A large number of Zn acceptors is visible in the image. Depending on their position *in* or *below* the (110) surface plane, Zn acceptors appear as either anisotropic, localized elevations (typically called "crablike" [159]), or as triangular protrusions superimposed on the GaAs lattice [149]. The topographic contrasts of impurity atoms in III-V semiconductors have been extensively studied in the past [7, 46, 108, 149, 152, 153, 159–162], and shallow Zn acceptors have been reported to be visible for a depth of up to 8 monolayers below the surface plane [163]. The visibility of subsurface impurities in STM is a consequence of the unpinned Fermi level of the GaAs(110) surface. The topographic contrast of a subsurface dopant atom is increasingly smeared out for an increasing depth of the dopant below the surface plane [159, 163]. Hence, the sharpest triangular features observed in Fig. 10.4 originate from subsurface Zn acceptors closest to the surface plane while the most smeared out features originate from Zn acceptors deep below the surface plane.

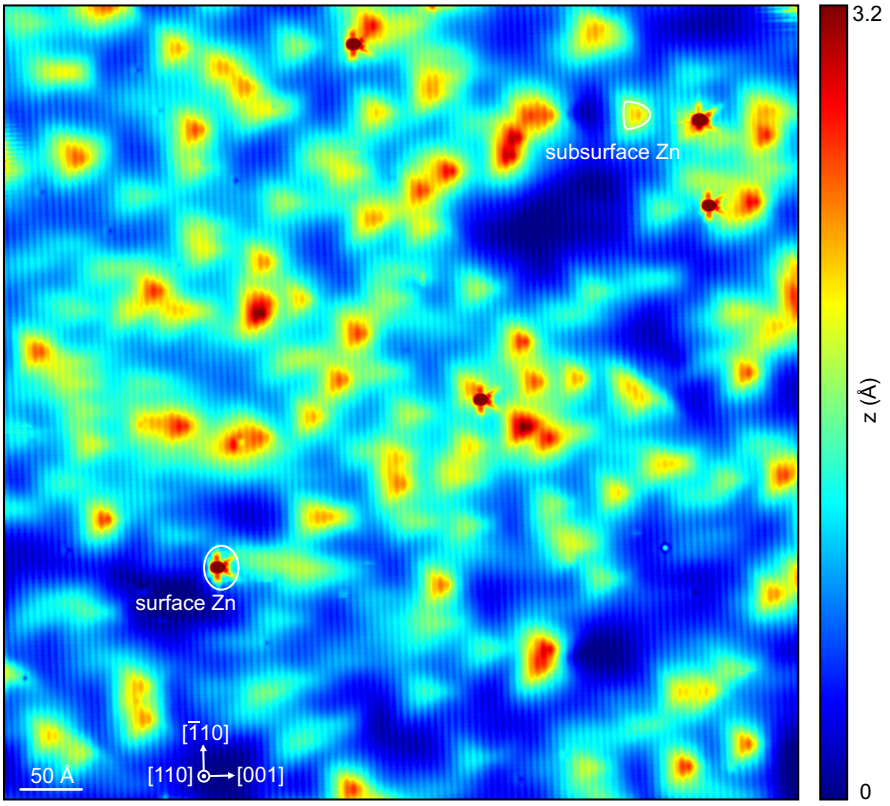

Figure 10.4: Typical low-bias empty state constant-current STM image of the (110) surface of Zn-doped GaAs ($V = +1.5$ V, $I = 10$ pA). At the particular sample bias chosen, the GaAs lattice is visible as parallel stripes running along the $(\bar{1}10)$ direction. Zinc acceptors located in the surface plane are visible as crablike localized features; subsurface Zn acceptors are visible as triangular elevations superimposed on the GaAs lattice.

If we count the number of anisotropic features observed in Fig. 10.4 and assume that these features indeed originate from dopant atoms located within the first 8 monolayers of the sample, we calculate a dopant density of 9×10^{18} cm^{-3}. This number fits exceptionally well to the nominal acceptor concentration of 1×10^{19} Zn/cm^3 specified by the supplier.

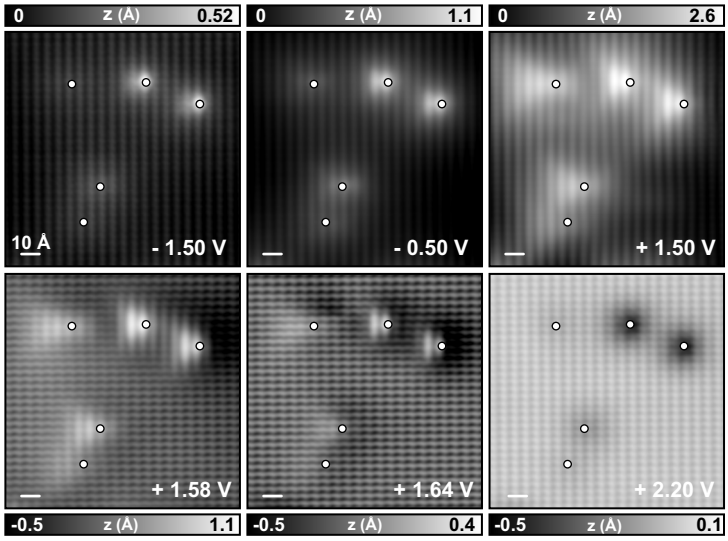

Figure 10.5: Bias dependence of the constant-current STM contrast of subsurface Zn acceptors (sample biases as indicated, $I = 20$ pA). Five acceptors are visible, located in different layers below the (110) surface. As a reference, the lateral position of each acceptor is indicated by an open circle. For positive sample biases around 1.5 V, the acceptors appear as anisotropic, triangular features.

Figure 10.5 shows the bias dependence of the topographic contrast of subsurface Zn acceptors. In the area imaged by the STM, five acceptors are visible, buried at different depths below the surface plane. For a high positive sample bias of $V = +2.20$ V (corresponding to electrons tunneling from the probe tip into empty conduction band states of the sample), the acceptors are visible as circular depressions superimposed on the atomic corrugation. For such high sample bias, the acceptor state is expected to be TIBB-shifted above the Fermi level of the sample and thus to be neutral. That is, the negative charge of the acceptor core is neutralized by the bound hole spread over many lattice sites. Hence, very close the acceptor core, the negative charge of the latter locally reduces the number of states available for tunneling into the conduction band as it locally bends the bands upward [7, 163]. Hence, the observed

depression is related to the core of the acceptor atom and can be used to determine the lateral position of the dopant atom below the surface plane [163]. In the STM images shown in Fig. 10.5, the center of this depression has been indicated by an open circle. For a positive sample bias of $V = +1.5$ V (corresponding to the onset of the tunneling of electrons from the probe tip into nominally empty conduction band states of the sample) the contrast induced by the acceptors is of pronounced triangular shape with the dopant atoms located at the tip of the triangle [150]. For an increased positive sample bias ($V = +1.58$ V and $V = +1.64$ V, respectively) at which the corrugation of the GaAs lattice is determined by electrons tunneling into the empty $C3$ surface resonance, the triangular features shrink in size and a depression at the tip of the triangle is observed. Similarly, at a low negative sample bias of $V = -0.5$ V (electrons tunneling from the occupied valence band of the sample into empty tip states) a triangular shaped feature is observed that shrinks and becomes more circularly symmetric for an increasingly negative sample bias ($V = -1.50$ V). The sample bias range at which the subsurface acceptors are observed as triangular features are reported to vary from tip to tip on the same sample, which is attributed to the different CPDs for different tip apices [151].

From theory, the triangular contrast introduced by buried shallow acceptors has been demonstrated to be due to the cubic symmetry of the host crystal in combination with the strain induced by the relaxation of the (110) surface of GaAs [164].

10.5. Electronic Transport through Buried Acceptors

Having reviewed its bias dependent topographic contrast, we now investigate the *electronic transport* through an individual subsurface Zn acceptor by means of combined KPFS and STS measurements.

Figure 10.6 shows KPFS and STS measurements performed with three different tip apices. These have been changed by controlled indentation

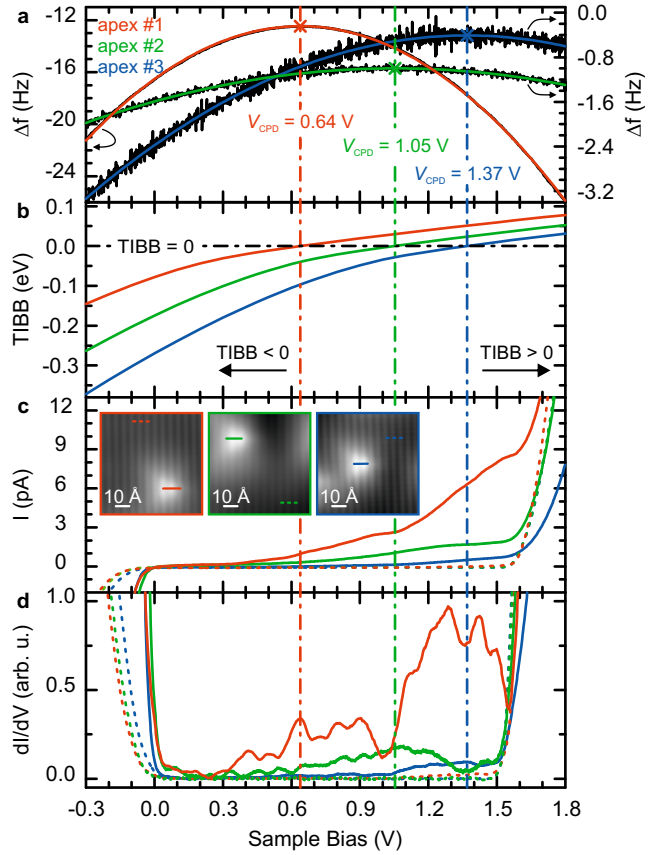

Figure 10.6: Contact potential difference and acceptor-induced conductance for different tip apices. **a**, Frequency shifts measured as a function of sample bias $\Delta f(V)$ (black lines), parabolic fits, and the corresponding flat-band voltages V_{CPD} are indicated (colored lines). **b**, Calculated tip-induced band bending. For any sample bias below (above) V_{CPD}, the band bending is negative (positive). **c**,**d**, show $I(V)$ and $dI/dV(V)$ spectra away from (dashed lines) and atop (solid lines) subsurface acceptors, positions are indicated in the constant-current STM images (inset: $V = 1.5$ V, $I = 20$ pA). For all tip apices, acceptor-induced enhanced current and conductance are observed in negative, zero, and positive band bending regimes.

into a clean Cu(111) surface. In the following, we will discuss data acquired with tip apex #1 (red lines in Fig. 10.6) while showing the results for three different tip apices to underscore the general validity of our findings. Figure 10.6a shows KPFS data. In KPFS, the frequency shift $\Delta f(V)$ of the force sensor is recorded as a function of the *dc* sample bias V at a fixed tip position. As introduced in Sec. 2.2.2, the electrostatic contribution to the force between tip and sample gives rise to a parabolic dependence of $\Delta f(V)$ with V as $\Delta f(V) \propto -(V - V_{\mathrm{CPD}})^2$. For compensated CPD, that is, for $V = V_{\mathrm{CPD}}$, the electrostatic field in the tip-sample junction will be zero and $\Delta f(V)$ will be maximal, respectively. In this situation, there is no electric field to penetrate the semiconductor and hence V_{CPD} is the flat-band voltage [165]. From the parabolic fit[4] to $\Delta f(V)$ (cf. Fig 10.6a), we extract a flat-band voltage of +0.64 V for tip apex #1. The assignment of V_{CPD} to the flat-band condition relies on the (110) surface of GaAs not being subject to Fermi level pinning, our cleaved surface being atomically flat, and our sample being homogeneous and well-conducting at 5 K. As this assignment is the key to our experiments, its uncertainty was experimentally determined by (i) KPFS data taken at different absolute tip-sample distances (see Sec. 5.3) as well as by (ii) comparative KPFS measurements on GaAs(110) and on Cu(111) using the same tip apex (see Sec. 10.8). Here we will only give the result of this determination while the corresponding experiments are presented and discussed in individual sections. From these experiments, we determined a generous upper bound of the uncertainty of the absolute value of V_{CPD} of 0.12 eV [166, 167], which is small compared to the voltage scales considered here.

As TIBB(V) is a monotonic function of the applied sample bias, shifted with respect to zero bias by the CPD, we can attribute a negative (positive) TIBB(V) to any sample bias below (above) +0.64 V, and TIBB(+0.64 V) = 0 for tip apex #1. The bias voltage dependence of TIBB(V) is shown in Fig. 10.6b, where we used V_{CPD} as an input parameter to a one-dimensional Poisson-equation solver[5] developed by

[4] The standard deviations of the parabolic fits to the $\Delta f(V)$ data are below 7 mV.
[5] For the TIBB calculation we assumed an absolute tip-sample distance of 10 Å.

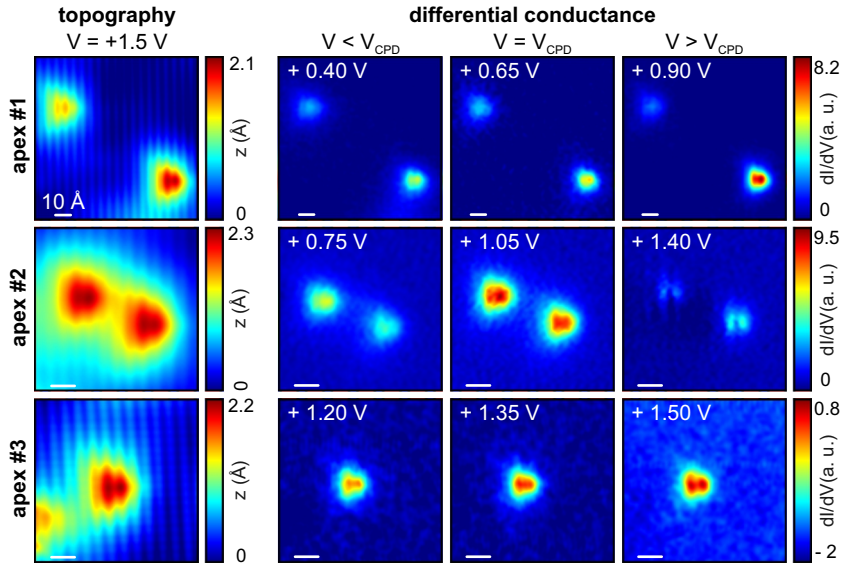

Figure 10.7: dI/dV maps of subsurface acceptors acquired with tip apices #1 to #3. The left column shows the corresponding constant-current STM topographies ($V = 1.5$ V, $I = 20$ pA). For each tip apex, dI/dV maps are acquired at voltages below, at, and above the corresponding flat-band voltage V_{CPD}. For all apices, within all band bending regimes a similar triangular feature of enhanced conductance is observed at the acceptors positions.

R. Feenstra [57]. The flat-band voltage [and the corresponding zero crossing of TIBB(V)] is indicated by a vertical (horizontal) dash-dotted line. We point out that the magnitude of TIBB(V) is still uncertain, as it depends on the geometry of the tip, which cannot be easily extracted from KPFS.

To map out the spatial dependence of the acceptor-related enhanced conductance, we have recorded differential conductance maps. Figure 10.7 shows dI/dV maps acquired with tip apices #1 to #3, recorded at bias voltages well below, right at, and well above the corresponding flat-band voltage. In accordance with previous experiments, we observe a triangular feature of enhanced conductance at the position of the dopant

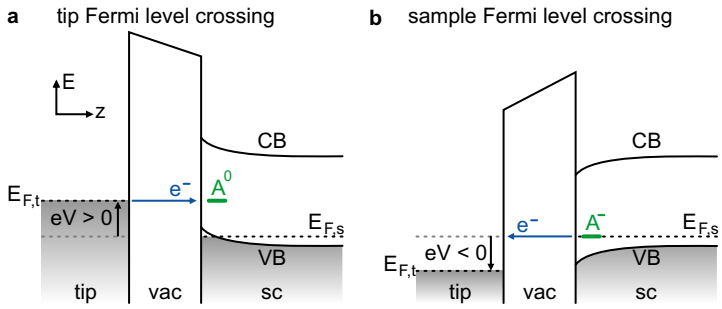

Figure 10.8: Bipolar tunneling. a Positive bias polarity. The electronic state labeled A is unoccupied. At increasing positive sample bias, the Fermi level of the tip eventually crosses A. Then, electrons can tunnel from the tip into the empty state A. **b**, Negative bias polarity. The electronic state A is dragged downward in energy by the TIBB. Eventually, it crosses the Fermi level of the sample and becomes permanently occupied. Then, electrons can tunnel from A into empty tip states. Therefore, one and the same state A contributes to tunneling for both bias polarities.

atom [149]. Most notably, for all apices a similar pattern of enhanced conductance is observed for negative, zero and positive band bending, The similarity present in different band bending regimes suggests that *one* conduction mechanism is responsible for all of them. In STM, in the presence of tip-induced band bending a single transport channel can be observed for *different bias polarities*. This is effect is referred to as bipolar tunneling [148, 149, 168]. As exemplary depicted in Fig. 10.8, in bipolar tunneling an electronic state (labeled A) contributes to tunneling (i) for positive bias polarity as it crosses the Fermi level of the tip (Fig. 10.8a) and (ii) for negative bias polarity, as the state is TIBB-shifted downward and crosses the Fermi level of the sample (Fig. 10.8b). Most importantly, in our experiments the polarity of the sample bias at which the differential conductance maps were acquired remained the same (positive). Hence, the occurrence of one and the same conduction mechanism in different band bending regimes is *not* related to bipolar tunneling.

10.6. Electronic Transport in an Anderson-Hubbard Model

The basis of most pictures used so far in the literature to explain the electronic transport through an individual acceptor in an STM setup is a single *isolated* acceptor level being shifted by TIBB(V) with respect to the Fermi level. In this picture, the occupation of the level has to abruptly change when shifted across the Fermi level, which determines whether or not a particular channel can contribute to transport, independent of the further details of the model (cf. Fig. 10.1) [150, 151]. Hence, in these pictures, no transport mechanisms can be active in *all* three band banding regimes for one particular sample bias polarity. However, our conductance spectra (Fig. 10.6d), related to the flat-band voltage (Fig. 10.6a and Fig. 10.6b), in combination with the dI/dV maps (Fig. 10.7), indeed suggest that one conduction mechanism is active in all three regimes.

To resolve this controversy, we consider not only one single acceptor which is shifted by TIBB, but *several* foremost acceptors which are influenced by the band bending. From a one-dimensional model for TIBB (chapter 4), the penetration depth s of the electric field into the interior of the GaAs sample can be estimated. If we take the known dopant concentration of our sample and a typical value for the absolute tip-sample distance z of 10 Å and assume a total potential difference $\phi_{\mathrm{T}} = eV + \Delta\phi$ between sample and tip of 1.5 eV, we estimate a penetration depth of the TIBB of about $s \approx 80$ Å [49]. This is roughly twice the value of the average nearest neighbor distance of acceptors of 47 Å. In the experimental (three-dimensional) system, assuming a tip-radius of $\gtrsim 150$Å, we expect about 10 acceptors to be located within the space-charge region caused by presence of the tip. This situation is schematically depicted in Fig. 10.9a.

In terms of the tip-induced band bending, two markedly different situations can be distinguished. (i) For zero band bending, all foremost acceptors are in resonance with each other and are at level with the impurity band, which extends to the surface of the sample. Hence, the

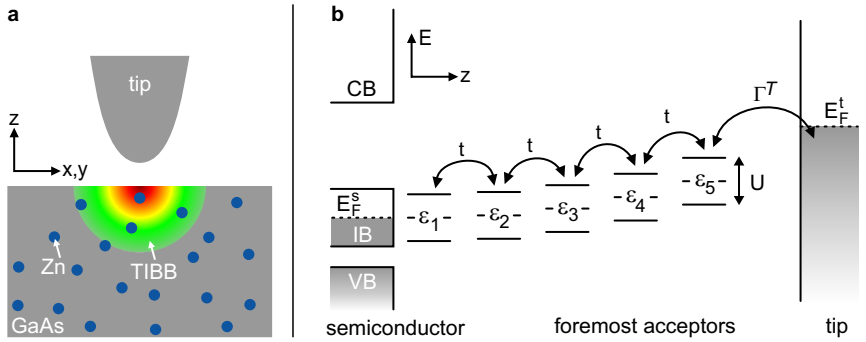

Figure 10.9: **a**, Sketch of the tunneling junction (after Ref. [136]). Several foremost acceptors are influenced by the TIBB. **b**, Energy scheme, sketching the single-particle energy levels relevant to an Anderson-Hubbard model of electron transport. The on-site energies ϵ_i of the foremost acceptors are shifted by the band bending. Two transport channels separated by the on-site Coulomb energy U are attributed to each acceptor. Adjacent acceptors are coupled via a hopping parameter t, the acceptor closest to the surface (acceptor #5) is coupled to the tip states via a tunneling rate Γ^T.

acceptor states are part of the delocalized impurity band. In this situation the Coulomb charging energy U (discussed below) necessary to add (or remove) 1 electron from (to) the system is negligible. (ii) For strong positive or negative band bending, on the other hand, the foremost acceptor states are detuned from each other and from the impurity band, see Fig. 10.9b. Hence, the acceptor states are expected to be localized to one or very few acceptors and Coulomb charging energies are expected to play a significant role in the electron transport. As TIBB(V) is a function of the sample bias, these very different situations of zero and strong band bending will be present within one individual tunneling spectra $I(V)$.

A model which intrinsically captures both, the existence of several interacting acceptor states as well as the cross-over between the different transport regimes outlined above is the *Anderson-Hubbard model*. For our system, transport calculations in the Anderson-Hubbard model

have been performed by Andrea Donarini of the Institute of Theoretical Physics at the University of Regensburg. Due to the computational expense of a many-body description in combination with limited computational power, our model considers a linear chain of N foremost equidistant acceptors (see Fig. 10.9b) as instead of the more realistic three-dimensional random distribution of acceptors depicted in Fig. 10.9a.

Three single-particle energies are relevant to the description of our system in an Anderson-Hubbard model. (i) The *on-site energy* ϵ_i of the ith acceptor. In the absence of TIBB, ϵ_i is constant and corresponds to the ionization energy of the Zn acceptor in GaAs; $\epsilon_i = E_\mathrm{A} = 31$ meV. In the presence of TIBB, ϵ_i is shifted by an amount depending on the depth of the ith acceptor below the surface. If we assume a parabolic drop off of the tip-induced electrostatic potential inside the semiconductor, we can model ϵ_i as

$$\epsilon_i(V) = E_\mathrm{A} + \left(\frac{i-1}{N-1}\right)^2 \times \mathrm{TIBB}(V), \tag{10.4}$$

where the deepest acceptor ($i = 1$) is not influenced by TIBB while the energy of the most superficial acceptor ($i = 5$) is shifted exactly by TIBB(V) [49] (cf. Fig. 10.9b). For our calculations, we have taken TIBB(V) as plotted in Fig 10.6b (tip apex #1). (ii) A *hopping parameter* t. The electron transport between two adjacent (localized) acceptor states is (in similarity to a tight binding model) described by a hopping parameter t. In the tight binding model, the calculated band-width of a linear chain of states is four times the hopping parameter t [169]. As the band-width of the impurity band ΔE_IB in our samples is roughly 20 meV, we have taken $t = 5$ meV. (iii) The *on-site Coulomb energy* U, which is the electrostatic repulsion of two electrons occupying the same acceptor state $\psi(\vec{r})$. It can be calculated from

$$U = \iint \mathrm{d}\vec{r}_1 \mathrm{d}\vec{r}_2 |\psi(\vec{r}_1)|^2 \frac{e^2}{4\pi\epsilon\epsilon_0 |\vec{r}_1 - \vec{r}_2|} |\psi(\vec{r}_2)|^2. \tag{10.5}$$

For a hydrogen-like wave function $\psi(\vec{r})$, this expression can be exactly determined to be [170]

$$U = \frac{5}{8} \frac{e^2}{4\pi\epsilon\epsilon_0 a_\mathrm{B}^*}. \tag{10.6}$$

The effective Bohr radius a_{B}^{*} of the shallow (that is, hydrogen-like) acceptor Zn in GaAs is estimated from Eq. (10.3) to be 47 Å. Hence, the on-site Coulomb energy U of an isolated Zn acceptor in GaAs is estimated to be about 15 meV. This value of the on-site Coulomb energy is much smaller than for an isolated atom or molecule in vacuum which is on the order of 1 eV. This is due to the large effective Bohr radius of the Zn acceptor and the high relative permittivity of GaAs ($\epsilon = 13$). In analogy to the Hubbard bands introduced above, two transport channels separated by U are attributed to each individual acceptor level ϵ_i in the Anderson-Hubbard model (cf. Fig. 10.9b). Each of these transport channels can be occupied by 1 electron on average. In the Anderson-Hubbard model, the Hamiltonian describing the N foremost acceptors reads [171–173]

$$\begin{aligned} H = &\sum_{i=1}^{N} \sum_{\sigma} \epsilon_i c_{i\sigma}^{\dagger} c_{i\sigma} - t \sum_{i=1}^{N-1} \sum_{\sigma} \left(c_{i\sigma}^{\dagger} c_{i+1\sigma} + c_{i+1\sigma}^{\dagger} c_{i\sigma} \right) \\ &+ U \sum_{i=1}^{N} \left(c_{i\uparrow}^{\dagger} c_{i\uparrow} - \tfrac{1}{2} \right) \left(c_{i\downarrow}^{\dagger} c_{i\downarrow} - \tfrac{1}{2} \right) \end{aligned} \tag{10.7}$$

where $c_{i\sigma}^{\dagger}$ creates and $c_{i\sigma}$ annihilates an electron of spin σ on the ith acceptor. The first term of the Anderson-Hubbard Hamiltonian describes the potential energy of the electrons localized at (the TIBB-shifted) acceptor levels. The second term models the kinetic energy of the electronic system and the third term accounts for the Coulomb on-site interaction.

In our model, the rest of the acceptor states (that is, the ones not influenced by TIBB, see Fig. 10.9a) and the valence and the conduction bands have been modeled as an electron bath with the respective densities of states, see Fig. 10.10. In particular, the DOS of the valence (conduction) band has been taken according to the effective mass of the holes (electrons) in this band. The metallic tip has been treated analogously, having a constant DOS. Further, we assume that the tunneling between tip and acceptors is restricted to the most superficial acceptor (Fig. 10.9b) . All foremost acceptors are instead coupled to the bulk of

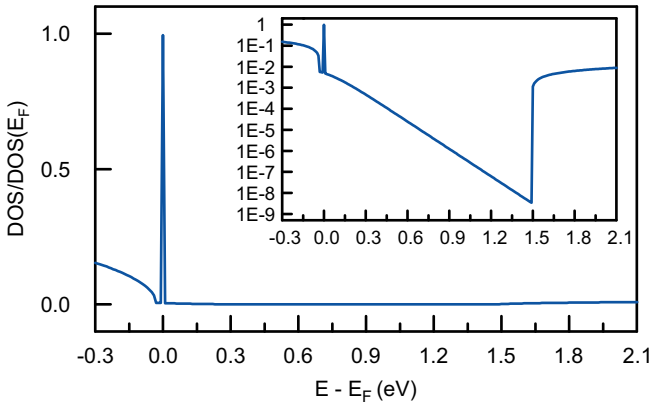

Figure 10.10: The density of states of bulk GaAs as used in our Anderson-Hubbard model. The peak at $E - E_{\mathrm{F}} = 0$ corresponds to the impurity band, the onset of the DOS below zero and above 1.5 eV correspond to the valence and conduction bands. Within the fundamental band gap, the DOS has been taken to be very small but non zero (cf. the semi-logarithmic plot shown as inset figure) to mimic the possibility of inelastic tunneling transport.

the sample. We note that energy dissipation is expected to occur via the inelastic excitation of vibrons [174]. The latter we tried to account for by assuming a very small but finite DOS also in the fundamental band gap of GaAs, see Fig. 10.10.

It is noted that a more elaborate treatment of the Anderson-Hubbard model is beyond the scope of this thesis, and in the following we only summarize the main results as they were derived by A. Donarini [143].

The dynamics of the system is understood as a sequence of tunneling events from (to) the tip or the bulk of the sample which increase (reduce) by 1 the number of electrons populating the foremost acceptors, and the system is described in the framework of the master equation approach. In accordance with the experimental situation, the tunneling rate Γ^T to and from tip states is by far the smallest and thus the foremost acceptors are essentially in equilibrium with the bulk. Moreover, for $V \approx V_{\mathrm{CPD}}$,

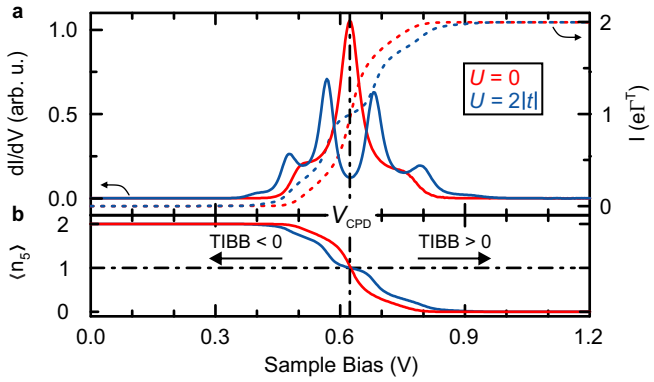

Figure 10.11: Simulated electron transport within the junction. **a**, Calculated $I(V)$ (dashed lines) and $dI/dV(V)$ (solid lines) spectra for vanishing ($U = 0$) and nonvanishing ($U = 2|t|$) on-site Coulomb energy U. The simulation yields nonzero current and conductance in a broad voltage range including negative, zero, and positive band bending. **b**, Calculated average population $\langle n_5 \rangle$ of the foremost acceptor.

electrons cannot tunnel from the foremost acceptors to the tip since all transport resonant levels lie far below the tip's Fermi level. For the above assumptions made, it is found that that the current through the system takes the form

$$I = e\Gamma^T \left(2 - \langle n_N \rangle\right) \tag{10.8}$$

where $\langle n_N \rangle$ is the average occupation of the most superficial acceptor, see Fig. 10.11b [143]. Note that $\langle n_N \rangle$ is *not* an integer number which abruptly changes from 0 to 2 as the most superficial acceptor crosses the Fermi level of the sample, as it would be the case in the simple single-particle models used before in this context [150, 151]. In our many-body Anderson-Hubbard approach, $\langle n_N \rangle$ changes *gradually* with increasing sample bias.

This many-body approach ensures that the *gradual change* of (i) the effective electronic coupling t, (ii) the localization, and (iii) the Coulomb charging energy U of the relevant states as a function of bias voltage

is inherently captured. Figure 10.11a shows the simulated $I(V)$ and $dI/dV(V)$ spectra for different values of U. Neglecting charging energy ($U = 0$), it shows enhanced current and conductance within a large bias range in different band bending regimes, for one sample bias polarity only, which is in accordance with our experimental findings. This phenomenon can be understood as follows. For $V \simeq V_{\mathrm{CPD}}$, $\mathrm{TIBB}(V)$ is smaller than the impurity band width and hence the foremost acceptor state is still part of the impurity band, even if slightly detuned from the bulk impurity states. In this voltage region, the Fermi level still remains inside this impurity band that extends to the foremost acceptor, and hence, finite conductance is observed. The size of this bias voltage range around V_{CPD} is given by the impurity band width $4t$ divided by the lever arm $\alpha = \mathrm{TIBB}(V)/V$. For $U \neq 0$, several peaks and dips appear in the spectra as opposed to just a single broad peak that is observed for $U = 0$. Close to V_{CPD}, the single occupation of the foremost acceptor prevails until $|\mathrm{TIBB}(V)|$ overcomes $U/2$. Hence, the average population and the current develop a plateau around V_{CPD} of width U divided by α.

The simulated spectra in Fig. 10.11a are in qualitative agreement with our experimental ones, showing enhanced conductance in all three band bending regimes. The experimental spectra show enhanced conductance over an even wider bias range than our theory predicts. Whereas U and α may differ from the values anticipated here, we note that electron-vibration coupling [174] could also play an important role, the incorporation of which goes beyond the scope of our model.

Finally, we tested our model against slight variations of the on-site energy (that is, the ionization energy E_{A}) of the most superficial acceptor. Slight variations of the ionization energies of acceptors located close to the surface plane are expected for e.g. due to the gradual change of the relative permittivity ϵ towards the semiconductor/vacuum interface [175, 176], as well as due to the Coulomb interaction between the *randomly* distributed acceptor atoms [177]. The results of this calculation is presented in Figure 10.12. The figure shows the differential conductance as a function of the sample bias. The different curves refer to different values of the on-site energy of the most superficial acceptor ϵ_5 and are offset

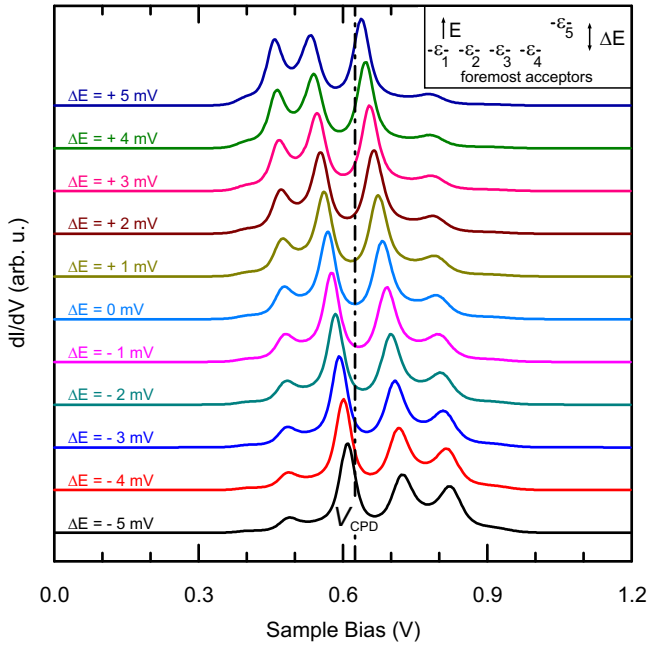

Figure 10.12: Calculated $\mathrm{d}I/\mathrm{d}V(V)$ spectra for eleven different values of the on-site energy of the most superficial acceptor, ϵ_5 (the inset corresponds to $\mathrm{TIBB}(V) = 0$), for $U = 2|t|$. The on-site energy is varied in the range -5 meV $\leq \epsilon_5 \leq +5$ meV. The spectra are vertically offset for clarity. Slight variations of the on-site energy result in considerable shifts of the peak positions with respect to the flat-band voltage V_{CPD} and in changes of the relative peak heights.

for clarity, the inset sketches the energetic alignment of the foremost acceptor states for zero $\mathrm{TIBB}(V)$. While again enhanced conductance is observed in a broad sample bias range including negative, zero and positive band bending regimes, the slight variations of ϵ_5 (on the order of a few meV) result in considerable shifts of the peak positions and of the relative peak heights in the differential conductance, which is an effect of the lever arm as discussed above.

This section can be summarized as follows. The use of combined STS

and KPFS allows us to unambiguously relate the conductance properties of shallow acceptors buried in GaAs to the energy scale of the system, by measuring the flat-band voltage. These measurements show that the voltage range of enhanced acceptor-induced conductance spans three different band bending regimes, ruling out previous conceptions of electronic transport used in this context [149–151]. This experimental finding requires a theoretical description which inherently captures the crossover between the acceptor state being part of an impurity band for zero band bending and the acceptor state being split off and localized for strong negative or positive band bending, respectively. Transport calculations based on an Anderson-Hubbard model yield spectra in qualitative agreement with our experiments.

10.7. Local Density of States Oscillations

In Sec. 10.5, we have used combined KPFS/STS to probe the electronic transport through buried Zn acceptors. Here, we use a combination of spatially resolved $\mathrm{d}I/\mathrm{d}V$ maps and KPFS to investigate the occurrence of local density of states oscillations around the subsurface acceptors.

The occurrence of local density of states oscillations, also referred to as charge density (CDO) or Friedel oscillations, is a pure quantum mechanical phenomena related to the introduction of a stationary charged impurity into an otherwise homogeneous system of mobile charge carriers. As the mobile charge carriers screen the electric field of the impurity, spatial oscillations in the charge density are observed which concentrically surround the impurity and which decay with increasing distance from the latter [178]. In STM, CDO's were first observed in 1996 by van der Wielen et al., who investigated Si donors buried in GaAs at low temperatures [178].

Figures 10.13 and 10.14 show two sets of bias dependent $\mathrm{d}I/\mathrm{d}V$ maps acquired with tip apices labeled #1 (see Sec. 10.5) and #4. For both sets, the feedback loop of the STM was opened at a setpoint bias of +1.8 V

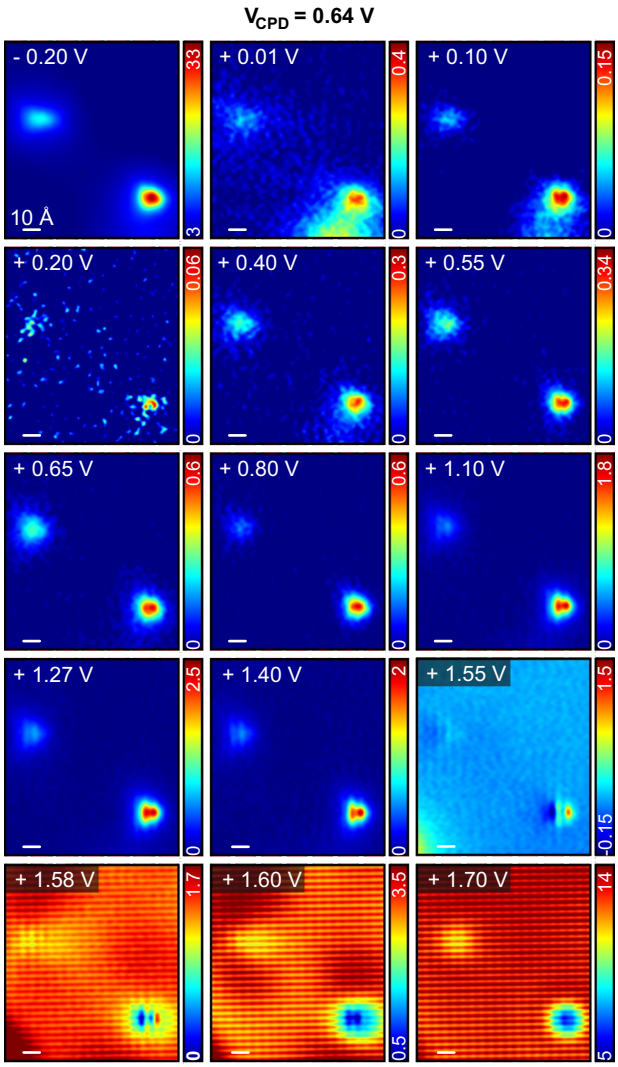

Figure 10.13: Bias-dependent $\mathrm{d}I/\mathrm{d}V$ maps of subsurface acceptors acquired with tip apex #1 (sample biases as indicated). The color-coded $\mathrm{d}I/\mathrm{d}V$ signal is in arbitrary units, the color-scale is adjusted for each individual map. Within a large sample bias window, including positive sample biases below, at, and above the flat-band voltage, a triangular feature of enhanced conductance is observed at the position of the dopant atoms. Local density of states oscillations are observed only at sample biases corresponding to tunneling of electrons from the tip to the conduction band of the sample (i. e. for $V > 1.5$ V).

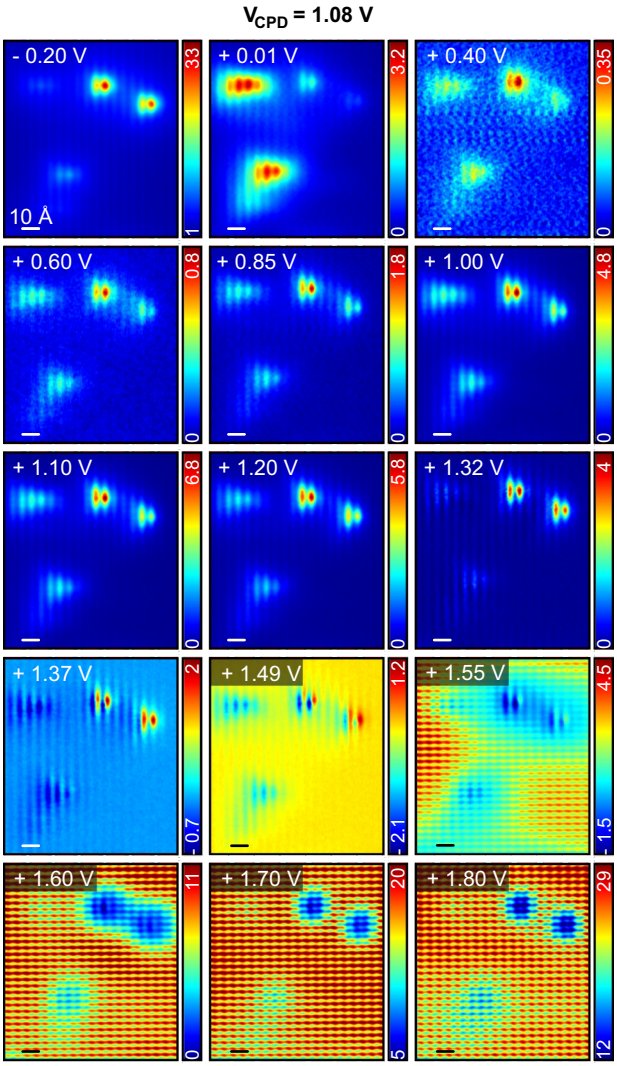

Figure 10.14: Bias-dependent dI/dV maps of subsurface acceptors acquired with tip apex #4 (sample biases as indicated). See the caption of Fig. 10.13 for further details.

and a setpoint current of 20 pA with the tip located away from dopant atoms before the tip was moved to the position where the maps were taken. For the set acquired with tip apex #4, the tip-sample distance was decreased by 0.25 Å once the feedback loop of the STM was opened. All maps are acquired atop subsurface Zn acceptors. In particular, the images acquired with tip apex #1 are recorded on the same area as those shown in Fig. 10.7, and the ones acquired with tip apex #4 are recorded on the same area as those shown in Fig. 10.5.

For these two tip apices, the flat-band voltages V_{CPD} have been determined from KPFS to be $V_{\mathrm{CPD}} = 0.64$ V for tip apex #1 and 1.08 V for tip apex #4. Although their respective flat-band voltages are distinctly different, for both apices we observe for negative, zero, and positive band bending regimes a similar feature of enhanced conduction at the position of the dopant atoms. This is in accordance with the experimental results described in in Sec. 10.5 and shows that the acceptor-related enhanced conductance is independent of the sign of TIBB(V). In fact, we note that for both tip apices the sample bias region in which the triangular feature is observed almost spans the entire semiconductor's band gap region ($0 < V < +1.52$ V). Additionally, these triangular features are also observed for negative sample biases ($V = -0.2$ V).

For increasingly positive sample biases exceeding the band gap of GaAs, ($V \geq 1.49$ V), the subsurface acceptors are observed as circular depressions, the diameter of which shrinks with increasing setpoint bias. This observation is in accordance with previous experimental results on subsurface acceptors [52], and is attributed to the local upward band bending induced by the negatively charged acceptor core introduced in Sec. 10.4. Additionally, we observe a long-range variation of the apparent height in the vicinity of the acceptors. For increasing setpoint biases, these variations become ring-like features centered around the acceptors. The appearance of these long-range variations in $\mathrm{d}I/\mathrm{d}V$ maps is more clearly seen in Fig. 10.15, where the atomic corrugation has been FFT-filtered out. Ring-like structures around subsurface dopant atoms have been reported in previous STM studies and were attributed to Friedel oscillations [52, 152, 178].

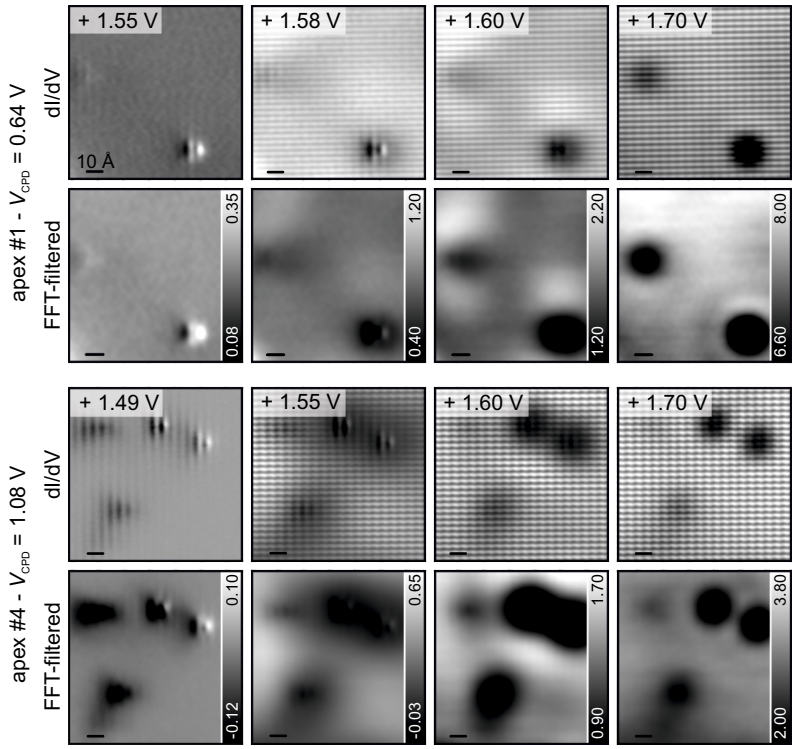

Figure 10.15: dI/dV maps acquired with tip apices #1 (top) and #4 (bottom), at sample biases close to the conduction band edge. To highlight the onset of oscillations in the local density of states, the atomic corrugation has been electronically (FFT) filtered out (bottom rows; the contrast is in arbitrary units and has been adjusted for each individual map).

For both apices the spatial local density of state oscillations are observed *only* for sample biases for which tunneling of electrons from the tip into the conduction band of the sample is possible, i.e. for $V > +1.5$ V, see Fig. 10.15. Indeed, for both tip apices those oscillations basically occur at the same sample bias as the $C3$ surface-resonance-related corrugation known to be due to tunneling of electrons into nominally empty conduction band states of the sample. From previous STM experiments, charge

density oscillations were argued to occur as soon as holes accumulate below the microscope's tip (i.e. for $V \geq V_{\mathrm{CPD}}$) which will be scattered at the negatively charged core-potential of the acceptor [52].

From our experiments however, relating the onset-voltage of oscillations in the local density of states to a quantitative value of the flat-band voltage, we conclude: whereas the existence of hole accumulation ($V \geq V_{\mathrm{CPD}}$) may play a role, the possibility of tunneling into the conduction band ($V > +1.5$ V) apparently is a necessary requirement for the observation of local density of states oscillations around acceptors in p-type GaAs. We note that our observations are consistent with experimental data (but not explanations) found in the literature [52, 152].

Further, we note that when comparing these two apices #1 and #4 in more detail, one realizes that for tip #1 the occurrence of local density of states oscillations occurs at slightly higher sample biases ($V = 1.58$ V) as compared to tip #4 ($V = 1.55$ V, $\Delta V \simeq 30$ mV), see Fig. 10.15. This slight shift is consistent with the CPD values extracted from KPFS under the assumption that oscillations are related to tunneling into the conduction band, but inconsistent under the assumption of being only related to the situation of hole accumulation. Note that for a larger CPD value the onset of tunneling into empty conduction band states occurs at a lower sample bias.

For tip apex #4, the tip-sample distance was slightly decreased after the feedback loop of the STM was opened. The magnitude of the TIBB increases with decreasing tip-sample distance. The stronger the TIBB, the higher the sample bias at which the Fermi level of the tip crosses the conduction band edge at the surface of the sample. For tip apex #4, we observe the onset of tunneling into the conduction band at a lower voltage as compared to tip apex #1. Hence, the observed change of ΔV between the two apices is *not* related to the slightly different tip-sample distances.

In summary, this is yet another example that the unknown CPD in previous experiments resulted in misinterpretation of experimental data [52].

10.8. Determination of the Absolute Error of KPFS

To the experiments presented in this chapter, the flat-bond voltage V_{CPD} determined from KPFS is the key to the interpretation of the data. Here, we present experimental results on the *absolute* uncertainty of the KPFS measurements.

To determine the absolute experimental uncertainty of our KPFS measurements on GaAs(110), we used KPFS data acquired on the clean Cu(111) surface (which we also used for tip preparation) as a reference. For each individual tip apex out of 8 in total, we determined the voltage corresponding to the CPD on both surfaces, i.e. $V_{\mathrm{CPD}}^{\mathrm{GaAs}}$ and $V_{\mathrm{CPD}}^{\mathrm{Cu}}$. The individual tip apices were changed by controlled indentations in the clean (111) surface of the Cu single crystal. For these 8 apices, the total variation of the work function of the tip [as extracted from KPFS on Cu(111)] was found to be about 0.4 eV.

The parameters at which KPFS data were acquired on the Cu(111) surface and on the GaAs(110) surface are as follows: The tip was retracted by $\Delta z = 5$ Å after the feedback loop of the STM was interrupted at a setpoint of $V = 50$ mV, $I = 2.5$ pA [on Cu(111)], or at sample bias ranging from 1.55 V to 1.8 V at a current of $I = 20$ pA [on GaAs(110)]. For each individual KPFS measurement, we fitted a Kelvin parabola to the $\Delta f(V)$ data and extracted the parabola's maximum; the standard deviations of the parabolic fits to the Kelvin parabolas are below 4 meV.

Figure 10.16 shows $\Delta V_{\mathrm{CPD}} = V_{\mathrm{CPD}}^{\mathrm{GaAs}} - V_{\mathrm{CPD}}^{\mathrm{Cu}}$ for eight individual tip apices labeled **a** to **h**. In total, ΔV_{CPD} is found to vary by 0.12 V, at an average value of 0.54 V. From the literature, ΔV_{CPD} is expected to be

$$\begin{aligned} \Delta V_{\mathrm{CPD}} &= \frac{1}{e}\left[\chi_{\mathrm{GaAs(110)}} + (E_{\mathrm{C}} - E_{\mathrm{F}}) - \phi_{\mathrm{Cu(111)}}\right] \\ &= 4.07\ \mathrm{V} + 1.49\ \mathrm{V} - 4.94\ \mathrm{V} \\ &= 0.62\ \mathrm{V} \end{aligned} \tag{10.9}$$

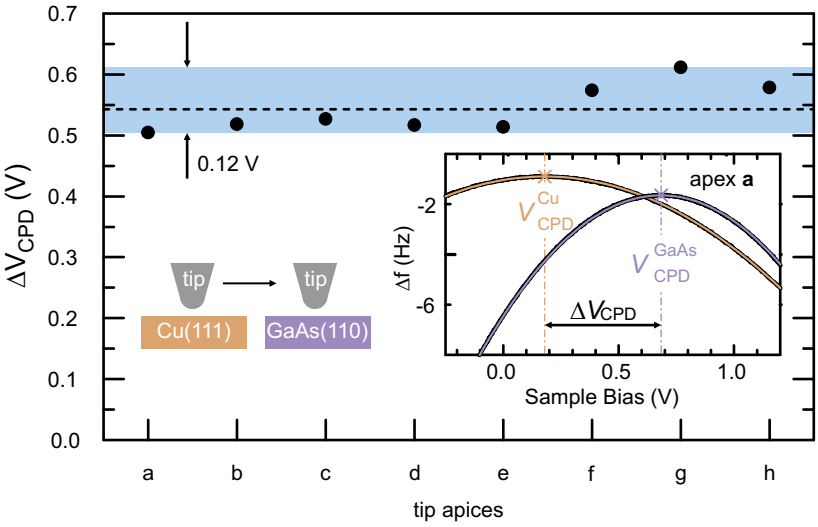

Figure 10.16: Difference of the contact potential difference acquired on Cu(111) and on GaAs(110), ΔV_{CPD}, for eight individual tip apices. The horizontal dashed line indicates the average of ΔV_{CPD} (0.54 V), its absolute variation is found to be 0.12 V. The inset shows, as an example, $\Delta f(V)$ data acquired with tip apex **a** (black lines), parabolic fits are indicated (colored).

with $\chi_{\mathrm{GaAs(110)}}$ and $(E_{\mathrm{C}} - E_{\mathrm{F}})$ being the electron affinity of GaAs(110) and the difference between conduction band edge and Fermi level in Zn-doped GaAs, respectively, and $\phi_{\mathrm{Cu(111)}}$ being the work function of the clean Cu(111) surface. From the literature, we have taken 4.94 eV for the work function of Cu(111) [40], 4.07 eV for the electron affinity of GaAs(110) [34], and (1.52−0.03) eV = 1.49 eV for the energetic difference between conduction band edge and Fermi level in Zn-doped GaAs, with the Fermi level located 0.03 eV above the edge of the valence band [34, 35].

From these finding, we estimate the total error of the KPFS measurements on GaAs(110) to be below 0.12 V [166, 167], which is small compared to the voltage scale considered in our experiment.

11. Summary and Outlook

This thesis focuses on STM and combined STM/KPFS experiments performed in the cross-sectional geometry on GaAs samples. Here, the results of the presented work are briefly summarized.

Individual π-conjugated Molecules Probed from STM

Chapter 8 presented STM investigations of individual iron-II-phthalocyanine molecules adsorbed on the (110) surface of an epitaxially grown GaAs-based heterostructure. From bias dependent imaging and spectroscopy, the electronic structure of the adsorbed molecules was found to largely resemble to one of the free molecule as in the gas phase. This provides strong evidence that the organic/inorganic system iron-II-phthalocyanine on GaAs(110) is weakly interacting. This finding was further underpinned by the possibility of current induced lateral movement of the molecules, leaving both adsorbate and substrate undamaged. As semiconducting surfaces are typically considered to be highly reactive, this finding is rather surprising, but may be understood from the occupation of dangling bonds on GaAs(110).

The built-in potential of the epitaxial heterostructure used as substrate was exploited as a means to tune the resonances of the adsorbed molecules, as it is shown in chapter 9. The molecular resonances observed in STS have been found to be shifted with respect to the constant Fermi level for different lateral adsorption positions of the molecules across the heterostructure. As expected for a weakly interacting molecule/substrate

system, the shift of the resonances was found to be in qualitative agreement with the vacuum-alignment rule.

Fixing the Energy Scale in STM on Semiconductors

The electronic transport through individual Zn acceptors buried below the (110) surface of GaAs has been probed from combined KPFS and STS. Whereas in pure STM experiments the energy scale in the tunneling junction is typically lost due to tip-induced band bending, we here experimentally recovered the zero point of the energy scale from KPFS. From this, the polarity of the tip-induced band bending was fixed for all bias voltages, and the electronic transport through Zn acceptors as probed from STS could be related to the different band bending regimes. As discussed in chapter 10, enhanced acceptor related conductance has been observed similarly in the different regimes of upward, downward and zero band bending. This finding contradicts previous experimental results obtained by other groups and demands a description in a many-body Anderson-Hubbard picture.

The combination of KPFS and STS also shade light on the bias dependent observation of charge density oscillations around subsurface acceptors, which were found to be present only for tunneling conditions at which electrons can access empty states in the sample. As for the electronic transport through buried acceptors, this finding contradicts the theoretical model prevailing in the literature concerning charge density oscillations.

In particular, the combination of KPFS and STS has been demonstrated to overcome one of the long-standing challenges of STM on semiconductors, which is the influence of the mere presence of the microscope's tip on the energy levels from tip-induced band bending.

Outlook

Recently, L. Gross et al. demonstrated combined STM and spatially resolved Kelvin probe spectroscopy to be a highly versatile tool for the investigation of the electronic structure and the charge distribution on a surface [179]. In this thesis, KPFS has so far only been employed to determine the contact potential difference between tip and and sample, and any lateral corrugation of the KPFS signal has been avoided by large tip-sample distances. While many researchers have exploited the possibilities of pure KPFS experiments on semiconductors, allowing for potential profiling of dopant distributions, quantum wells and surface defects [180–187], there are only very few experiments utilizing combined STM/KPFS [188]. In particular, the local charge distribution due to a subsurface dopant atom as well as the charge distribution within the surface unit cell of a polar bonded semiconductor have not been resolved yet [189].

Figure 11.1 shows preliminary spatially resolved combined STM/KPFS results obtained on the (110) surface of Zn-doped GaAs. While from STM (Fig. 11.1a,b) the individual Zn acceptors are unambiguously determined from their bias dependent shape, from KPFS the modification of the *local* contact potential difference (LCPD) induced by the individual acceptors is probed (Fig. 11.1c). For the KPFS map, at a fixed tip-sample distance at each pixel of the map the bias voltage has been ramped and the frequency shift Δf of the force sensor was recorded. Each spectra $\Delta f(V)$ was then fitted by a Kelvin parabola and the maximum of each parabola was determined, which corresponds to the LCPD. While for the KPFS data presented in the main text the tip-sample distance was comparatively large, here a short tip-sample distance was used to achieve a high spatial resolution[1]. Clearly, the modification of the potential landscape due to the presence of the subsurface acceptors can be recognized in the KFPS map. The KPFS map shown in the inset

[1] For the data shown in Fig. 11.1c, the tip-sample distance was given by an STM setpoint of $I = 3.25$ pA, $V = +1.55$ V (main figure), as well as by $I = 20$ pA, $V = +1.53$ V (inset).

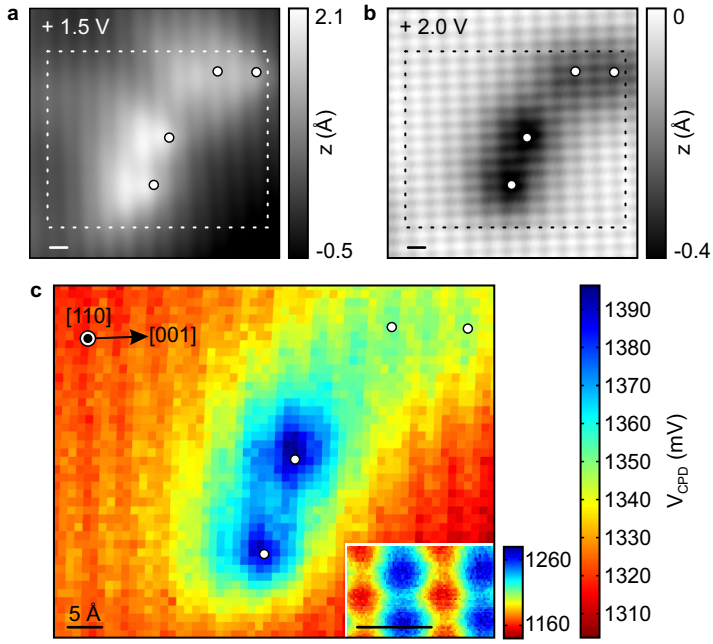

Figure 11.1: LCPD maps of shallow acceptors buried in GaAs. a, b, Constant-current STM topographies of the (110) surface of Zn doped GaAs ($I = 3.3$ pA, bias voltage as indicated). Four subsurface Zn acceptors are located within the area imaged by the STM, the lateral positions of which are indicated by the open circles. **c**, For each lateral tip position within the area framed by the dotted lines in (a) and (b), the bias voltage was ramped and the frequency shift $\Delta f(V)$ of the force sensor was recorded. Each individual dataset was fitted by a Kelvin parabola, the maximum of the parabola V_{CPD} was determined and is displayed as color code. The inset shows an additional LCPD map, acquired with the same tip but for a different tip-sample distance and at a smaller grid spacing, resolving the unit cell of GaAs(110).

clearly exhibits a strong corrugation that follows the periodicity of the surface unit cell of GaAs(110). The preliminary data presented here offer promising prospects for future KPFS/STM studies of the electronic structure around embedded dopant atoms as well as of the corresponding III-V seminconductor host material.

Part IV.

Appendix

APPENDIX A.

Comparison between KPFS and I(z)-Spectroscopy

Without having the capability of performing combined KPFS/STS experiments, in pure STM-based experiments many researchers exploited the dependence of the tunneling current I on the tip-sample distance z to extract the contact potential difference between the microscope's tip and the sample [12, 52, 150, 151, 190–192].

$I(z)$-spectroscopy is a method that allows a determination of the inverse decay constant κ of the tunneling current. As shown in Sec. 2.1.1, in a one-dimensional model the tunneling current is assumed to decay exponentially with tip-sample distance (see Eq. 2.2),

$$I = I_0 e^{-2\kappa z}. \tag{A.1}$$

Figure A.1 shows a semi-logarithmic plot of $I(z)$-spectra acquired with *one individual* tip apex (labeled **a**) on Cu(111) as well as on GaAs(110) surfaces, respectively. For the $I(z)$-spectra shown here, the tunneling current I was recorded while the tip-sample distance z was increased by Δz once the feedback loop of the STM was opened at a setpoint of $V = +50$ mV, $I = 2.5$ pA on Cu(111) and of $V = +1.6$ V, $I = 20$ pA on GaAs(110), respectively. Kelvin probe spectra acquired on both surfaces using the same tip apex **a** are shown in the inset of Fig. 10.16.

If one *assumes* that the inverse decay length κ is indeed linked to an apparent barrier height $\overline{\phi}$ of the tunneling junction via $\kappa = \sqrt{2m\overline{\phi}/\hbar^2}$,

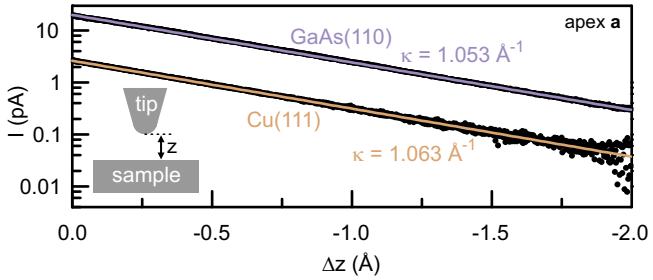

Figure A.1: $I(z)$-spectroscopy on Cu(111) and on GaAs(110) surfaces (black, semilogarithmic plot), single-exponential fits and corresponding values of the inverse decay length κ are indicated (color).

the apparent barrier height then could be experimentally determined from $I(z)$ spectroscopy via the relation

$$\overline{\phi} = \frac{\hbar^2}{2m}\left(\frac{d\ln I}{dz}\right)^2 . \tag{A.2}$$

Whereas the comparison of the apparent barrier height extracted from $I(z)$-spectroscopy on different sample areas (e.g. decorated by an adlayer of varying thickness) can provide a qualitative measure for the changes in work function [193, 194], it is well known that caution is in order when trying to quantitatively interpret this quantity in terms of the CPD [195].

The derivation of an actual value for the CPD from $I(z)$-spectra depends strongly on the model for tunneling that is applied to relate $\overline{\phi}$ to the contact potential difference [12, 52, 150, 151]. For example, image charge effects that arise from the presence of the metallic tip in front of the sample surface have been shown to considerably lower the tunneling barrier (by $\sim$ 1 eV) and to render the shape of the barrier non-trapezoidal. The strength of such image charge effects depends on the tip-sample distance, being strongest for short tip-sample distances [151]. Further, for very short tip-sample distances ($z < 5$ Å), relaxations of the foremost atoms in tip and sample due to the close proximity of each other have

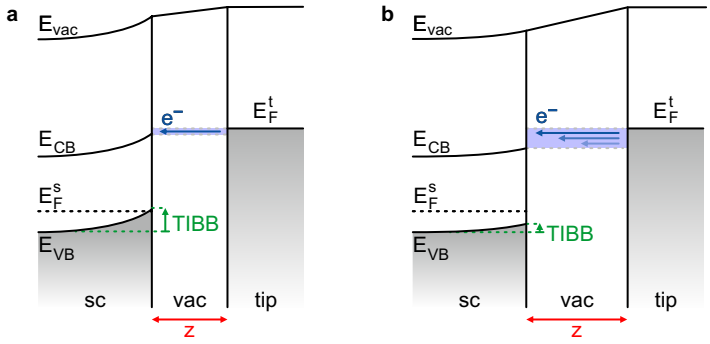

Figure A.2: **a**, and **b**, Semiconductor-vacuum-tip tunneling junctions at different tip-sample distances z; in (b) z is larger than in (a). All electronic states within the energy interval between the Fermi level of the tip, $E_{\mathrm{F}}^{\mathrm{t}}$, and the conduction band edge, E_{CB}, at the surface of the sample contribute to tunneling (shaded blue). At constant bias voltage, with increasing distance z the magnitude of the band bending is decreased, which, in turn, increases the number of states available for tunneling at the sample surface.

been shown to considerably alter the total tip-sample distance [190]. Especially on semiconducting surfaces a qualitative interpretation of $\overline{\phi}$ can be hampered by the tip-sample distance dependence of TIBB, which can affect the $I(z)$-spectra by changing the number of states in the sample available for tunneling as is depicted in Fig. A.2. For a very large tip-sample distance, almost the entire bias applied to the tunneling junction will drop-off within the vacuum gap. However, for a short tip-sample distance a significant fraction of the bias will drop-off within the interior of the sample which will bend the semiconductor's bands at its surface. Hence, the magnitude of the band bending depends on the tip-sample distance and is large if the latter is short. For the positive sample bias used in our experiments, all electronic states within the energy interval between the Fermi level of the tip, $E_{\mathrm{F}}^{\mathrm{t}}$ and the conduction band minimum E_{CB} at the surface of the sample contribute to tunneling. This energy interval is shaded blue in Fig. A.2. It is modified by the TIBB, as the latter changes the number of empty states available at the surface of the sample. For a positive sample bias, the TIBB effects on $I(z)$-

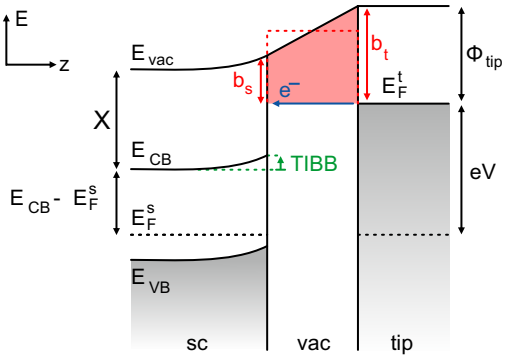

Figure A.3: Geometric model relating the band structures of tip and sample to the tunneling barrier heights b_t and b_s, respectively, experienced by the highest state tunneling (blue arrow). The trapezoidal tunneling barrier (shaded red) is approximated by a rectangular barrier (dashed red lines). After Ref. [12]

spectroscopy are expected to be largest for sample biases corresponding to the onset of tunneling into nominally empty conduction band states (e.g. around $V = +1.5$ V), as here the number of states available in the sample for tunneling is very small. Hence, in this bias range the *relative* change of the number of states available for tunneling is comparable to the total number of states available in the sample [192].

All the above described effects can be neglected or taken into account in different ways leading to several different models to extract the CPD from $I(z)$-spectroscopy. In this chapter, we aim at benchmarking a model for CPD extraction from $I(z)$ spectra that has been used previously in the literature. This model has been developed by S. Loth et al. [12, 52, 150], and is solely based on geometrical considerations. This model makes the assumption that the tunneling current is dominated by the highest state tunneling, see Fig. A.3. This assumption may be justified by the exponential suppression of tunneling probability with increasing barrier height, see Sec. 2.1.2. Here, we only discuss the case of a positive sample bias exceeding the band gap of GaAs ($V \geq +1.5$ V) as used in our experiments. In this bias regime, the highest state tunneling is located at the Fermi level of the tip E_F^t. The height of the tunneling barrier at the surface of the tip and of the sample, b_t and b_s (Fig. A.3), respectively, is related to the band structure of the tip and the sample

by the expressions

$$\begin{aligned} b_\mathrm{t} &= \phi_\mathrm{tip} \\ b_\mathrm{s} &= E_\mathrm{CB} - E_\mathrm{F}^\mathrm{s} + \chi + \mathrm{TIBB}(V) - eV \end{aligned} \tag{A.3}$$

where ϕ_tip is the work function of the tip, $E_\mathrm{CB} - E_\mathrm{F}^\mathrm{s}$ is the difference between the sample's conduction band minimum and its Fermi level, and $\mathrm{TIBB}(V)$ is the band bending at the surface of the semiconductor, respectively. Note that the notation used here is identical to one used by S. Loth [12]. To connect the heights of the trapezoidal shaped tunneling barrier b_t and b_s, respectively, to the experimentally determined apparent barrier height $\overline{\phi}$, the rectangular shaped tunneling barrier is then simplified to a rectangular one (Fig. A.3), the height of which is the average of b_t and b_s

$$\overline{\phi} = \frac{b_\mathrm{t} + b_\mathrm{s}}{2}. \tag{A.4}$$

Insertion of Eqs. A.3 and A.4 into the definition of the CPD (Eq. 4.1) finally yields

$$V_\mathrm{CPD}^\mathrm{GaAs} = \frac{2}{e}\left[E_\mathrm{CB} - E_\mathrm{F}^\mathrm{s} + \chi + \mathrm{TIBB}(V) - \overline{\phi}\right] - V \tag{A.5}$$

where we note that the work function of the semiconducting sample at its surface is $\phi_\mathrm{GaAs} = E_\mathrm{CB} - E_\mathrm{F,s} + \chi + \mathrm{TIBB}(V)$. In Eq. A.5 all terms except for the bias dependent $\mathrm{TIBB}(V)$-term are known. If we choose a sample bias well above the onset of tunneling of electrons from the tip into nominally empty conduction band states ($V \gg 1.49$ V), the z dependence of $\mathrm{TIBB}(V)$ discussed above is expected to be negligible, and the $\mathrm{TIBB}(V)$-term gives rise to a small correction only (below 0.1 eV, see Fig. 10.6a, positive sample bias), which should not affect our comparison and which we therefore neglect.

For the $I(z)$-spectra acquired on Cu(111), we proceed likewise in data analysis. Here, the barrier height at the surface of the tip and of the sample (Eq. A.3) are the respective work functions, hence, from Eq. 4.1 and A.4 we find:

$$V_\mathrm{CPD}^\mathrm{Cu} = \frac{2}{e}\left(\phi_\mathrm{t} - \overline{\phi}\right) \tag{A.6}$$

Method	KPFS	$I(z)$
$V_{\mathrm{CPD}}^{\mathrm{Cu(111)}}$ (V)	0.18 ± 0.12	1.27
$V_{\mathrm{CPD}}^{\mathrm{GaAs(110)}}$ (V)	0.68 ± 0.12	1.06

Table A.1: Comparison of V_{CPD} acquired with one individual tip apex on both Cu(111) and on GaAs(110) surfaces.

Table A.1 presents V_{CPD} values inferred from the $I(z)$-spectra shown in Fig. A.1 and determined from the KPFS data shown in the inset of Fig. 10.16. The data have been acquired with one and the same tip apex on both Cu(111) and on GaAs(110) surfaces. First, we notice that the V_{CPD} values inferred from $I(z)$-spectroscopy are inconsistent with the ones extracted from KPFS, with differences as large as 1 V. When we compare the data acquired on different surfaces, the changes of V_{CPD} values inferred from $I(z)$-spectroscopy even have the wrong sign. The work function of clean Cu(111) is $\phi_{\mathrm{Cu(111)}} = 4.94\ eV$ [40], whereas the one of Zn-doped GaAs(110) is $\phi_{\mathrm{GaAs}} = E_{\mathrm{CB}} - E_{\mathrm{F,s}} + \chi = 1.49 + 4.07 = 5.56$ eV (neglecting TIBB effects). As $\phi_{\mathrm{GaAs}} > \phi_{\mathrm{Cu}}$, the CPD has to increase when going from Cu(111) to GaAs(110). The values determined from the $I(z)$-spectra, however, decrease. By contrast, the change in V_{CPD} extracted from KPFS of 0.5 V reproduces the correct value of the change of V_{CPD} of 0.62 V within the margin of the error.

With the tip apex labeled #3 from Sec. 10.5, we recorded a series of 20 individual $I(z)$-spectra on GaAs(110). The lateral positions at which the individual spectra were taken are equidistantly spaced along a 40 Å long line, oriented parallel to the crystallographic [001] direction, located away from dopant atoms or defects. Using the model described above, we inferred V_{CPD} from each individual spectra and subsequently calculate mean and standard deviation of the series of spectra. This procedure was repeated three times, interrupting the feedback loop of the STM at a current of 20 pA and three different sample biases. The corresponding results are presented in Table A.2. The values inferred from $I(z)$-

Method	KPFS	$I_{+1.5\,\mathrm{V}}(z)$	$I_{+1.6\,\mathrm{V}}(z)$	$I_{+2.0\,\mathrm{V}}(z)$
$V_{\mathrm{CPD}}^{\mathrm{GaAs}}(V)$	1.37 ± 0.12	0.65 ± 0.43	-0.01 ± 0.30	1.81 ± 0.14

Table A.2: Comparison of V_{CPD} values as determined from KPFS and as inferred from $I(z)$-spectroscopy for tip apex #3. For the $I(z)$ spectra, the feedback loop of the STM was interrupted at three different setpoints of the sample bias and at a tunneling current of 20 pA each. The setpoint bias is indicated as subscript.

spectroscopy show a strong variation with setpoint sample bias, which is most likely due to the influence of the z-dependence of TIBB(V) on $I(z)$-spectra acquired at the onset of tunneling into nominally empty conduction band states (e.g., $V = +1.5$ V and $V = +1.6$ V) as it is explained above. Additionally the tip-sample distance at which the feedback loop of the STM is interruped before the tip is retracted is larger for a higher setpoint sample bias, which further reduces the z-dependence of TIBB(V). This larger tip-sample distance may also account for the comparatively low standard deviation of the V_{CPD} value inferred at +2.0 V setpoint bias, as for a larger tip-sample distance atomic-scale variations of the sample surface are expected to be increasingly smeared out.

In conclusion, our comparative measurements show that the V_{CPD} values extracted from $I(z)$-spectroscopy are neither correct nor self-consistent, at least if the tunneling junction is modeled by the simple model used in this chapter. The fact that the CPD values extracted from $I(z)$-spectroscopy do not even reproduce the correct sign of changes of the CPD when comparing GaAs with Cu shows that the derivations are way beyond any useful error margins.

Bibliography

[1] P. M. Koenraad and M. E. Flatté, *Single dopants in semiconductors*, Nat. Mater. **10**, 91 (2011).

[2] G. Binnig, H. Rohrer, C. Gerber, and E. Weibel, *Surface Studies by Scanning Tunneling Microscopy*, Phys. Rev. Lett. **49**, 57 (1982).

[3] G. Binnig, C. F. Quate, and C. Gerber, *Atomic Force Microscope*, Phys. Rev. Lett. **56**, 930 (1986).

[4] G. A. Fiete and A. de Lozanne, *Seeing Quantum Fractals*, Science **327**, 652 (2010).

[5] G. Binnig, H. Rohrer, C. Gerber, and E. Weibel, *7×7 Reconstruction on Si(111) Resolved in Real Space*, Phys. Rev. Lett. **50**, 120 (1983).

[6] R. M. Feenstra and A. P. Fein, *Surface morphology of GaAs(110) by scanning tunneling microscopy*, Phys. Rev. B **32**, 1394 (1985).

[7] J. F. Zheng, X. Liu, N. Newman, E. R. Weber, D. F. Ogletree, and M. Salmeron, *Scanning tunneling microscopy studies of Si donors (Si_{Ga}) in GaAs*, Phys. Rev. Lett. **72**, 1490 (1994).

[8] R. M. Feenstra and J. A. Stroscio, *Tunneling spectroscopy of the GaAs(110) surface*, Journal of Vacuum Science & Technology B **5**, 923 (1987).

[9] J. K. Garleff, A. P. Wijnheijmer, and P. M. Koenraad, *Challenges in cross-sectional scanning tunneling microscopy on semiconductors*, Semiconductor Science and Technology **26**, 064001 (2011).

[10] C. J. Chen, *Introduction to Scanning Tunneling Microscopy*, 2nd ed. (Oxford University Press, 2008), pp. 5, 6, 54, 96, 158, 245, 351.

[11] F. Mohn, *Probing electronic and structural properties of single molecules on the atomic scale*, PhD thesis (Universität Regensburg, 2012).

[12] S. Loth, *Atomic Scale Images of Acceptors in III-V Semiconductors*, PhD thesis (Universität Göttingen, 2008).

[13] N. Pavliček, *Scanning Probe Methods Applied to Molecular Electronics*, PhD thesis (University of Regensburg, 2013).

[14] G. Binnig, H. Rohrer, C. Gerber, and E. Weibel, *Tunneling through a controllable vacuum gap*, Applied Physics Letters **40**, 178 (1982).

[15] D. M. Eigler and E. K. Schweizer, *Positioning single atoms with a scanning tunneling microscope*, Nature **344**, 524 (1990).

[16] R. Feenstra, J. A. Stroscio, and A. Fein, *Tunneling spectroscopy of the Si(111) 2×1 surface*, Surface Science **181**, 295 (1987).

[17] F. J. Giessibl, *Atomic Resolution of the Silicon (111)-(7x7) Surface by Atomic Force Microscopy*, Science **267**, 68 (1995).

[18] T. R. Albrecht, P. Grütter, D. Horne, and D. Rugar, *Frequency modulation detection using high-Q cantilevers for enhanced force microscope sensitivity*, Journal of Applied Physics **69**, 668 (1991).

[19] G. Meyer and N. M. Amer, *Obtical-beam-deflection atomic force microscopy: The NaCl(001) surface*, Applied Physics Letters **56**, 2100 (1990).

[20] F. J. Giessibl, *Atomic resolution on Si(111)-(7 × 7) by noncontact atomic force microscopy with a force sensor based on a quartz tuning fork*, Applied Physics Letters **76**, 1470 (2000).

[21] F. Schwabl, *Quantenmechanik*, 7th ed. (Springer Berlin, 2007), p. 63.

[22] J. Bardeen, *Tunnelling from a Many-Particle Point of View*, Phys. Rev. Lett. **6**, 57 (1961).

[23] J. Tersoff and D. R. Hamann, *Theory of the scanning tunneling microscope*, Phys. Rev. B **31**, 805 (1985).

[24] G. Hörmandinger, *Imaging of the Cu(111) surface state in scanning tunneling microscopy*, Phys. Rev. B **49**, 13897 (1994).

[25] R. J. Hamers, *Atomic-Resolution Surface Spectroscopy with the Scanning Tunneling Microscope.* Annu. Rev. Phys. Chem. **40**, 531 (1989).

[26] F. J. Giessibl, *Forces and frequency shifts in atomic-resolution dynamic-force microscopy*, Phys. Rev. B **56**, 16010 (1997).

[27] L. Gross, F. Mohn, P. Liljeroth, J. Repp, F. J. Giessibl, and G. Meyer, *Measuring the Charge State of an Adatom with Noncontact Atomic Force Microscopy*, Science **324**, 1428 (2009).

[28] S. Morita, R. Wiesendanger, and E. Meyer, eds., *Noncontact Atomic Force Microcopy* (Springer, Berlin, 2002), pp. 2, 20.

[29] M. Guggisberg et al., *Separation of interactions by noncontact force microscopy*, Phys. Rev. B **61**, 11151 (2000).

[30] F. J. Giessibl, *Advances in atomic force microscopy*, Rev. Mod. Phys. **75**, 949 (2003).

[31] H. Hamaker, *The London-van der Waals attraction between spherical particles*, Physica **4**, 1058 (1937).

[32] S. Sadewasser and T. Glatzel, eds., *Kelvin Probe Force Microscopy*, Vol. 48 (Springer, Heidelberg, 2011), pp. 7, 11, 47, 134.

[33] M. Saint Jean, S. Hudlet, C. Guthmann, and J. Berger, *Van der Waals and capacitive forces in atomic force microscopies*, Journal of Applied Physics **86**, 5245 (1999).

[34] S. Adachi, *GaAs and Related Materials. Bulk Semiconducting and Superlattice Properties* (World Scientific, Singapore, 1999), pp. 15, 19, 115, 165, 181.

[35] E. F. Schubert, *Doping in III–V Semiconductors* (Cambridge University Press, 2005), pp. 31, 35, 43, 187.

[36] C. A. Coulson, L. B. Redei, and D. Stocker, *The Electronic Properties of Tetrahedral Intermetallic Compounds. I. Charge Distribution*, Proceedings of the Royal Society of London. Series A. **270**, 357 (1962).

[37] K. S. Chandrasekaran, S. K. Mohanlal, and R. Saravanan, *Charge transfer in the bonding of GaAs*, physica status solidi (b) **196**, 3 (1996).

[38] GaAs band sturcture and carrier concentration, `www.ioffe.ru/SVA/NSM/Semicond/GaAs`.

[39] E. Kaxiras, *Atomic and Electronic Structure of Solids* (Cambridge University Press, England, 2003), p. 402.

[40] D. R. Linde, ed., *Handbook of Chemistry and Physics*, 90th ed. (CRC Press, Boca Raton, 2004), pp. 12–121, 9–98.

[41] A. R. Lubinsky, C. B. Duke, B. W. Lee, and P. Mark, *Semiconductor Surface Reconstruction: The Rippled Geometry of GaAs(110)*, Phys. Rev. Lett. **36**, 1058 (1976).

[42] R. M. Feenstra, J. A. Stroscio, J. Tersoff, and A. P. Fein, *Atom-selective imaging of the GaAs(110) surface*, Phys. Rev. Lett. **58**, 1192 (1987).

[43] G. Schwarz, *Untersuchungen zu Defekten auf und nahe der (110) Oberfläche von GaAs und weiteren III-V-Halbleitern*, PhD thesis (Technischen Universität Berlin, 2002).

[44] P. Ebert, B. Engels, P. Richard, K. Schroeder, S. Blügel, C. Domke, M. Heinrich, and K. Urban, *Contribution of Surface Resonances to Scanning Tunneling Microscopy Images: (110) Surfaces of III-V Semiconductors*, Phys. Rev. Lett. **77**, 2997 (1996).

[45] J. R. Chelikowsky and M. L. Cohen, *Self-consistent pseudopotential calculation for the relaxed (110) surface of GaAs*, Phys. Rev. B **20**, 4150 (1979).

[46] Z. F. Zheng, M. B. Salmeron, and E. R. Weber, *Empty state and filled state image of Zn_{Ga} acceptor in GaAs studied by scanning tunneling microscopy*, Applied Physics Letters **64**, 1836 (1994).

[47] R. M. Feenstra, *Tunneling spectroscopy of the (110) surface of direct-gap III-V semiconductors*, Phys. Rev. B **50**, 4561 (1994).

[48] R. M. Feenstra, G. Meyer, F. Moresco, and K. H. Rieder, *Low-temperature scanning tunneling spectroscopy of n-type GaAs(110) surfaces*, Phys. Rev. B **66**, 165204 (2002).

[49] R. M. Feenstra, *Electrostatic potential for a hyperbolic probe tip near a semiconductor*, Journal of Vacuum Science & Technology B **21**, 2080 (2003).

[50] R. M. Feenstra, Y Dong, M. P. Semtsiv, and W. T. Masselink, *Influence of tip-induced band bending on tunnelling spectra of semiconductor surfaces*, Nanotechnology **18**, 044015 (2007).

[51] R. Dombrowski, C. Steinebach, C. Wittneven, M. Morgenstern, and R. Wiesendanger, *Tip-induced band bending by scanning tunneling spectroscopy of the states of the tip-induced quantum dot on InAs(110)*, Phys. Rev. B **59**, 8043 (1999).

[52] S. Loth, M. Wenderoth, R. G. Ulbrich, S. Malzer, and G. H. Döhler, *Connection of anisotropic conductivity to tip-induced space-charge layers in scanning tunneling spectroscopy of p-doped GaAs*, Phys. Rev. B **76**, 235318 (2007).

[53] R. G. Wilson, *Vacuum Thermionic Work Functions of Polycrystalline Be, Ti, Cr, Fe, Ni, Cu, Pt, and Type 304 Stainless Steel*, Journal of Applied Physics **37**, 2261 (1966).

[54] R. Smoluchowski, *Anisotropy of the Electronic Work Function of Metals*, Phys. Rev. **60**, 661 (1941).

[55] P. Hahn, J. Clabes, and M. Henzler, *LEED-investigations and work-function measurements of the first stages of epitaxy of tungsten on tungsten (110)*, Journal of Applied Physics **51**, 2079 (1980).

[56] W. Schottky, *Halbleitertheorie der Sperrschicht*, Naturwissenschaften **26**, 843 (1938).

[57] The caluclation was perfomed by use of the SEMITIP software, `www.andrew.cmu.edu/user/feenstra/`, Version 6.

[58] D. C. Gohlke, *Tuning the Properties and Interactions of Manganese Acceptors in Gallium Arsenide with STM*, PhD thesis (Ohio State University, 2010).

[59] L. Kelvin, *Contact electricity of metals*, Philosophical Magazine Series 5 **46**, 82 (1898).

[60] M. Nonnenmacher, M. P. O'Boyle, and H. K. Wickramasinghe, *Kelvin probe force microscopy*, Applied Physics Letters **58**, 2921 (1991).

[61] S. Hudlet, M. S. Jean, B. Roulet, J. Berger, and C. Guthmann, *Electrostatic forces between metallic tip and semiconductor surfaces*, Journal of Applied Physics **77**, 3308 (1995).

[62] T. Vančura, S. Kičin, T. Ihn, K. Ensslin, M. Bichler, and W. Wegscheider, *Kelvin probe spectroscopy of a two-dimensional electron gas below 300 mK*, Applied Physics Letters **83**, 2602 (2003).

[63] A. J. Weymouth, T. Wutscher, J. Welker, T. Hofmann, and F. J. Giessibl, *Phantom Force Induced by Tunneling Current: A Characterization on Si(111)*, Phys. Rev. Lett. **106**, 226801 (2011).

[64] A. J. Weymouth and F. J. Giessibl, *The effect of sample resistivity on Kelvin probe force microscopy*, Applied Physics Letters **101**, 213105, 213105 (2012).

[65] F. Krok, K. Sajewicz, J. Konior, M. Goryl, P. Piatkowski, and M. Szymonski, *Lateral resolution and potential sensitivity in Kelvin probe force microscopy: Towards understanding of the sub-nanometer resolution*, Phys. Rev. B **77**, 235427 (2008).

[66] T. Hochwitz, A. K. Henning, C. Levey, C. Daghlian, and J. Slinkman, *Capacitive effects on quantitative dopant profiling with scanned electrostatic force microscopes*, Journal of Vacuum Science & Technology B **14**, 457 (1996).

[67] G. Meyer, *A simple low-temperature ultrahigh-vacuum scanning tunneling microscope capable of atomic manipulation*, Review of Scientific Instruments **67**, 2960 (1996).

[68] `www.sps-createc.com`.

[69] S. Zöphel, *Der Aufbau eines Tieftemperatur-Rastertunnelmikroskops und Strukturuntersuchungen auf vicinalen Kupferoberflächen*, PhD thesis (Freie Universität Berlin, 2000).

[70] M. Neu, *Rasterkraftmikroskopie auf atomarer Skala: Van-der-Waals Wechselwirkung in molekularen Systemen*, PhD thesis (Universität Regensburg, 2013).

[71] K. Besocke, *An easily operable scanning tunneling microscope*, Surface Science **181**, 145 (1987).

[72] J. Frohn, J. F. Wolf, K. Besocke, and M. Teske, *Coarse tip distance adjustment and positioner for a scanning tunneling microscope*, Review of Scientific Instruments **60**, 1200 (1989).

[73] F. J. Giessibl, pat. DE196 33 546 A1 (1998).

[74] S.-W. Hla, K.-F. Braun, V. Iancu, and A. Deshpande, *Single-Atom Extraction by Scanning Tunneling Microscope Tip Crash and Nanoscale Surface Engineering*, Nano Letters **4**, 1997 (2004).

[75] L. Gross, N. Moll, F. Mohn, A. Curioni, G. Meyer, F. Hanke, and M. Persson, *High-Resolution Molecular Orbital Imaging Using a p-Wave STM Tip*, Phys. Rev. Lett. **107**, 086101 (2011).

[76] M. F. Crommie, C. P. Lutz, and D. M. Eigler, *Imaging Standing Waves in a Two-dimensional Electron Gas*, Nature **363**, 524 (1993).

[77] K. Sauthoff, M. Wenderoth, A. J. Heinrich, M. A. Rosentreter, K. J. Engel, T. C. G. Reusch, and R. G. Ulbrich, *Nonlinear dynamic instability in brittle fracture of GaAs*, Phys. Rev. B **60**, 4789 (1999).

[78] M. A. Rosentreter, M. Wenderoth, N. H. Theuerkrauf, A. J. Heinrich, M. A. Schneider, and R. G. Ulbrich, *Nonequilibrium configurations of monatomic steps on cleaved GaAs(110) surfaces*, Phys. Rev. B **56**, 10538 (1997).

[79] A. M. Yakunin, *Mn in GaAs studied by X-STM: from a single impurity to ferromagnetic layers*, PhD thesis (Technische Universität Eindhoven, 2005).

[80] D. S. Kitchen, *Atom-by-Atom Substitution of Transition Metals in GaAs and Visualization of Hole-Mediated Interactions*, PhD thesis (University of Illinois at Urbana-Champaign, 2006).

[81] www.wafertech.co.uk.

[82] www.axt.com.

[83] D. Lee, *Atomic Scale Gate Electrode Formed by a Charged Defect: Scanning Tunneling Microscopy of Single Impurities in GaAs Semiconductors*, PhD thesis (Ohio State University, 2010).

[84] S. Modesti, H. Gutzmann, J. Wiebe, and R. Wiesendanger, *Correction of systematic errors in scanning tunneling spectra on semiconductor surfaces: The energy gap of Si(111)-7 × 7 at 0.3 K*, Phys. Rev. B **80**, 125326 (2009).

[85] G. Münnich, F. Albrecht, C. Nacci, M. Utz, D. Schuh, K. Kanisawa, S. Fölsch, and J. Repp, *Probing individual weakly-coupled π-conjugated molecules on semiconductor surfaces*, Journal of Applied Physics **112**, 034312 (2012).

[86] F. Albrecht, *Scanning Tunneling Microscopy on Iron Phthalocyanine Molecules on a GaAs surface*, Diploma thesis (Universität Regensburg, 2010).

[87] J. Repp, G. Meyer, S. M. Stojković, A. Gourdon, and C. Joachim, *Molecules on Insulating Films: Scanning-Tunneling Microscopy Imaging of Individual Molecular Orbitals*, Phys. Rev. Lett. **94**, 026803 (2005).

[88] R. A. Wolkow, *Controlled Molecular Adsorption on Silicon: Laying a Foundation for Molecular Devices*, Annual Review of Physical Chemistry **50**, 413 (1999).

[89] G. Comtet, G. Dujardin, L. Hellner, M. Lastapis, M. Martin, A. J. Mayne, and D. Riedel, *Atomic-scale STM experiments on semiconductor surfaces: towards molecular nanomachines*, Philosophical Transactions of the Royal Society of London. Series A **362**, 1217 (2004).

[90] J. R. Heath, *Molecular Electronics*, Annual Review of Materials Research **39**, 1 (2009).

[91] I. Fleming, *Molecular Orbitals and Organic Chemical Reactions*, Student Edition (John Wiley & Sons Ltd., United Kingdom, 2009), p. 27.

[92] G. Ashkenasy, D. Cahen, R. Cohen, A. Shanzer, and A. Vilan, *Molecular Engineering of Semiconductor Surfaces and Devices*, Accounts of Chemical Research **35**, 121 (2002).

[93] R. Passmann et al., *Adsorption structure of cyclopentene on InP-(001)(2×4)*, Phys. Rev. B **80**, 125303 (2009).

[94] R. J. Hamers, S. K. Coulter, M. D. Ellison, J. S. Hovis, D. F. Padowitz, M. P. Schwartz, C. M. Greenlief, and J. N. Russell, *Cycloaddition Chemistry of Organic Molecules with Semiconductor Surfaces*, Accounts of Chemical Research **33**, 617 (2000).

[95] F. Nunzi, A. Sgamellotti, C. Coletti, and N. Re, *Adsorption and Interfacial Chemistry of Pentacene on the Clean Si(100) Surface: A Density Functional Study*, The Journal of Physical Chemistry C **112**, 6033 (2008).

[96] R. Lin, M. Galili, U. J. Quaade, M. Brandbyge, T. Bjørnholm, A. D. Esposti, F. Biscarini, and K. Stokbro, *Spontaneous dissociation of a conjugated molecule on the Si(100) surface*, Journal of Chemical Physics **117**, 321 (2002).

[97] A. Bellec, F. Ample, D. Riedel, G. Dujardin, and C. Joachim, *Imaging Molecular Orbitals by Scanning Tunneling Microscopy on a Passivated Semiconductor*, Nano Letters **9**, 144 (2009).

[98] A. Zhao et al., *Controlling the Kondo Effect of an Adsorbed Magnetic Ion Through Its Chemical Bonding*, Science **309**, 1542 (2005).

[99] C. Iacovita, M. V. Rastei, B. W. Heinrich, T. Brumme, J. Kortus, L. Limot, and J. P. Bucher, *Visualizing the Spin of Individual Cobalt-Phthalocyanine Molecules*, Phys. Rev. Lett. **101**, 116602 (2008).

[100] N. Tsukahara et al., *Adsorption-Induced Switching of Magnetic Anisotropy in a Single Iron(II) Phthalocyanine Molecule on an Oxidized Cu(110) Surface*, Phys. Rev. Lett. **102**, 167203 (2009).

[101] P. Liljeroth, J. Repp, and G. Meyer, *Current-Induced Hydrogen Tautomerization and Conductance Switching of Naphthalocyanine Molecules*, Science **317**, 1203 (2007).

[102] Y. Wang, J. Kröger, R. Berndt, and W. A. Hofer, *Pushing and Pulling a Sn Ion through an Adsorbed Phthalocyanine Molecule*, Journal of the American Chemical Society **131**, 3639 (2009).

[103] I. Swart, T. Sonnleitner, and J. Repp, *Charge State Control of Molecules Reveals Modification of the Tunneling Barrier with Intramolecular Contrast*, Nano Letters **11**, 1580 (2011).

[104] J. J. Cox, S. M. Bayliss, and T. S. Jones, *Influence of substrate orientation on the formation of ordered copper phthalocyanine overlayers on InAs*, Surface Science **425**, 326 (1999).

[105] N. Papageorgiou, E. Salomon, T. Angot, J.-M. Layet, L. Giovanelli, and G. L. Lay, *Physics of ultra-thin phthalocyanine films on semiconductors*, Progress in Surface Science **77**, 139 (2004).

[106] E. Salomon, T. Angot, N. Papageorgiou, and J.-M. Layet, *Self-assembled monolayer of tin-phthalocyanine on InSb(001)-(4×2)/c(8×2)*, Surface Science **596**, 74 (2005).

[107] A. Tekiel, M. Goryl, and M. Szymonski, *Copper phthalocyanine molecules on an InSb(001)-c(8×2) surface studied by ultra-high-vacuum STM and non-contact AFM*, Nanotechnology **18**, 475707 (2007).

[108] A. M. Yakunin, A. Y. Silov, P. M. Koenraad, J. H. Wolter, W. Van Roy, J. De Boeck, J.-M. Tang, and M. E. Flatté, *Spatial Structure of an Individual Mn Acceptor in GaAs*, Phys. Rev. Lett. **92**, 216806 (2004).

[109] A. Richardella, P. Roushan, S. Mack, B. Zhou, D. A. Huse, D. D. Awschalom, and A. Yazdani, *Visualizing Critical Correlations Near the Metal-Insulator Transition in $Ga_{1-x}Mn_xAs$*, Science **327**, 665 (2010).

[110] N. Marom and L. Kronik, *Density functional theory of transition metal phthalocyanines, II: electronic electronic structure of MnPc and FeP–symmetry and symmetry breaking*, Applied Physics A **95**, 165 (2009).

[111] J. F. Kirner, W. Dow, and W. R. Scheidt, *Molecular stereochemistry of two intermediate-spin complexes. Iron(II) phthalocyanine and manganese(II) phthalocyanine*, Inorganic Chemistry **15**, 1685 (1976).

[112] J. Clayden, N. Greeves, S. Warren, and P. Wothers, *Organic Chemistry* (Oxford University Press, Oxford, England, 2008), p. 1179.

[113] M.-S. Liao and S. Scheiner, *Electronic structure and bonding in metal phthalocyanines, Metal=Fe, Co, Ni, Cu, Zn, Mg*, The Journal of Chemical Physics **114**, 9780 (2001).

[114] B. W. Dale, R. J. P. Williams, C. E. Johnson, and T. L. Thorp, *S = 1 Spin State of Divalent Iron. I. Magnetic Properties of Phthalocyanine Iron (II)*, The Journal of Chemical Physics **49**, 3441 (1968).

[115] C. Uhlmann, I. Swart, and J. Repp, *Controlling the Orbital Sequence in Individual Cu-Phthalocyanine Molecules*, Nano Letters **13**, 777 (2013).

[116] R. Maboudian, K. Pond, V. Bressler-Hill, M. Wassermeier, P. Petroff, G. Briggs, and W. Weinberg, *Tunneling spectroscopy on the GaAs(110) surface: Effect of dopant concentration*, Surface Science **275**, L662 (1992).

[117] DFT calculations were perfomed with the NWChem package version 6.0, using the pbe0 exchange correlation functional and the def2-tzvpp basis set.

[118] M. Valiev et al., *NWChem: A comprehensive and scalable open-source solution for large scale molecular simulations*, Computer Physics Communications **181**, 1477 (2010).

[119] I. Nevo and S. Cohen, *Scanning tunneling microscopy of single dye molecules on GaAs(110) surfaces*, Surface Science **583**, 297 (2005).

[120] K. Teichmann, M. Wenderoth, S. Loth, R. G. Ulbrich, J. K. Garleff, A. P. Wijnheijmer, and P. M. Koenraad, *Controlled Charge Switching on a Single Donor with a Scanning Tunneling Microscope*, Phys. Rev. Lett. **101**, 076103 (2008).

[121] A. J. Mayne and G. Dujardin, eds., *Atomic and Molecular Manipulation*, Vol. 2 (Elsevier Science, 2011).

[122] R. Möller, R. Coenen, A. Esslinger, and B. Koslowski, *The topography of isolated molecules of copper–phthalocyanine adsorbed on GaAs(110)*, Journal of Vacuum Science & Technology A **8**, 659 (1990).

[123] A. Scarfato, S.-H. Chang, S. Kuck, J. Brede, G. Hoffmann, and R. Wiesendanger, *Scanning tunneling microscope study of iron(II) phthalocyanine growth on metals and insulating surfaces*, Surface Science **602**, 677 (2008).

[124] A. F. Takács, F. Witt, S. Schmaus, T. Balashov, M. Bowen, E. Beaurepaire, and W. Wulfhekel, *Electron transport through single phthalocyanine molecules studied using scanning tunneling microscopy*, Phys. Rev. B **78**, 233404 (2008).

[125] N. Pavliček, I. Swart, J. Niedenführ, G. Meyer, and J. Repp, *Symmetry Dependence of Vibration-Assisted Tunneling*, Phys. Rev. Lett. **110**, 136101 (2013).

[126] *Molecular Electronics*, CHIMIA **6** (2010).

[127] C. H. Ahn et al., *Electrostatic modification of novel materials*, Rev. Mod. Phys. **78**, 1185 (2006).

[128] H. Song, Y. Kim, Y. H. Jang, H. Jeong, M. A. Reed, and T. Lee, *Observation of molecular orbital gating*, Nature **462**, 1039 (2009).

[129] L. B. Ruppalt and J. W. Lyding, *Charge transfer between semiconducting carbon nanotubes and their doped GaAs(110) and InAs(110) substrates detected by scanning tunnelling spectroscopy*, Nanotechnology **18**, 215202 (2007).

[130] C. Uhlmann, *Tieftemperatur-Rastertunnelmikroskopie an Phthalocyanin-Molekülen auf ultradüunnen Isolatorfilmen: Ladungszustand, Jahn-Teller Effekt und ein molekularer Schalter*, PhD thesis (Universtität Regensburg, 2013).

[131] N. A. Pradhan, N. Liu, C. Silien, and W. Ho, *Atomic Scale Conductance Induced by Single Impurity Charging*, Phys. Rev. Lett. **94**, 076801 (2005).

[132] D. H. Lee and J. A. Gupta, *Tunable Field Control Over the Binding Energy of Single Dopants by a Charged Vacancy in GaAs*, Science **330**, 1807 (2010).

[133] D.-H. Lee and J. A. Gupta, *Tunable Control over the Ionization State of Single Mn Acceptors in GaAs with Defect-Induced Band Bending*, Nano Letters **11**, 2004 (2011).

[134] P. G. Piva, G. A. DiLabio, J. L. Pitters, J. Zikovsky, M. Rezeq, S. Dogel, W. A. Hofer, and R. A. Wolkow, *Field regulation of single-molecule conductivity by a charged surface atom*, Nature **435**, 658 (2005).

[135] H. Zheng, J. Kröger, and R. Berndt, *Spectroscopy of Single Donors at ZnO(0001) Surfaces*, Phys. Rev. Lett. **108**, 076801 (2012).

[136] A. P. Wijnheijmer, J. K. Garleff, K. Teichmann, M. Wenderoth, S. Loth, and P. M. Koenraad, *Single Si dopants in GaAs studied by scanning tunneling microscopy and spectroscopy*, Phys. Rev. B **84**, 125310 (2011).

[137] I. G. Hill, A. Rajagopal, A. Kahn, and Y. Hu, *Molecular level alignment at organic semiconductor-metal interfaces*, Applied Physics Letters **73**, 662 (1998).

[138] M. T. Greiner, M. G. Helander, W.-M. Tang, Z.-B. Wang, J. Qui, and Z.-H. Lu, *Universal energy-level alignment of molecules on metal oxides*, Nature Materials **11**, 76 (2011).

[139] H. Vázquez, Y. J. Dappe, J. Ortega, and F. Flores, *Energy level alignment at metal/organic semiconductor interfaces: "Pillow" effect, induced density of interface states, and charge neutrality level*, The Journal of Chemical Physics **126**, 144703 (2007).

[140] O. Madelung, *Semiconductors: Data Handbook*, 3rd ed. (Springer Berlin, 2003), p. 125.

[141] K. T. Shinobu Ohya and M. Tanaka, *Nearly non-magnetic valence band of the ferromagnetic semiconductor GaMnAs*, Nature Physics **7**, 342 (2011).

[142] J. Fujii et al., *Identifying the Electronic Character and Role of the Mn States in the Valence Band of (Ga,Mn)As*, Phys. Rev. Lett. **111**, 097201 (2013).

[143] G. Münnich, A. Donarini, M. Wenderoth, and J. Repp, *Fixing the Energy Scale in Scanning Tunneling Microscopy on Semiconductor Surfaces*, Phys. Rev. Lett. **111**, 216802 (2013).

[144] M. McEllistrem, G. Haase, D. Chen, and R. J. Hamers, *Electrostatic sample-tip interactions in the scanning tunneling microscope*, Phys. Rev. Lett. **70**, 2471 (1993).

[145] F. Marczinowski, J. Wiebe, J.-M. Tang, M. E. Flatté, F. Meier, M. Morgenstern, and R. Wiesendanger, *Local Electronic Structure near Mn Acceptors in InAs: Surface-Induced Symmetry Breaking and Coupling to Host States*, Phys. Rev. Lett. **99**, 157202 (2007).

[146] F. Marczinowski, J. Wiebe, F. Meier, K. Hashimoto, and R. Wiesendanger, *Effect of charge manipulation on scanning tunneling spectra of single Mn acceptors in InAs*, Phys. Rev. B **77**, 115318 (2008).

[147] S. R. Schofield, P. Studer, C. F. Hirjibehedin, N. J. Curson, G. Aeppli, and D. R. Bowler, *Quantum engineering at the silicon surface using dangling bonds*, Nature Communications **4**, 1649 (2013).

[148] K. Hashimoto et al., *Quantum Hall Transition in Real Space: From Localized to Extended States*, Phys. Rev. Lett. **101**, 256802 (2008).

[149] G. Mahieu, B. Grandidier, D. Deresmes, J. P. Nys, D. Stiévenard, and P. Ebert, *Direct Evidence for Shallow Acceptor States with Nonspherical Symmetry in GaAs*, Phys. Rev. Lett. **94**, 026407 (2005).

[150] S. Loth, M. Wenderoth, L. Winking, R. G. Ulbrich, S. Malzer, and G. H. Döhler, *Probing Semiconductor Gap States with Resonant Tunneling*, Phys. Rev. Lett. **96**, 066403 (2006).

[151] A. P. Wijnheijmer, J. K. Garleff, M. A. v. d. Heijden, and P. M. Koenraad, *Influence of the tip work function on scanning tunneling microscopy and spectroscopy on zinc doped GaAs*, Journal of Vacuum Science & Technology B **28**, 1086 (2010).

[152] R. de Kort, M. C. M. M. van der Wielen, A. J. A. van Roij, W. Kets, and H. van Kempen, *Zn- and Cd-induced features at the GaAs(110) and InP(110) surfaces studied by low-temperature scanning tunneling microscopy*, Phys. Rev. B **63**, 125336 (2001).

[153] A. Richardella, D. Kitchen, and A. Yazdani, *Mapping the wave function of transition metal acceptor states in the GaAs surface*, Phys. Rev. B **80**, 045318 (2009).

[154] S. T. Pantelides, ed., *Deep Centers in Semiconductors*, 1st ed. (Gordon and Breach, New York, 1986), 21 ff.

[155] H. Kamimura and H. Aoki, *The Physics of Interacting Electrons in Disordered Systems* (Oxford University Press, Oxford, England, 1990), p. 7.

[156] D. Ashen, P. Dean, D. Hurle, J. Mullin, A. White, and P. Greene, *The incorporation and characterisation of acceptors in epitaxial GaAs*, Journal of Physics and Chemistry of Solids **36**, 1041 (1975).

[157] P. Y. Yu and M. Cardona, *Fundamental of Semiconductors*, 4th ed. (Springer, Heidelberg, Germany, 2010), pp. 175, 176.

[158] H. Neumann, B. Jacobs, and W. Hörig, *Band tail conduction in Zn-doped GaAs*, Crystal Research and Technology **25**, 343 (1990).

[159] J. K. Garleff, C. Çelebi, W. Van Roy, J.-M. Tang, M. E. Flatté, and P. M. Koenraad, *Atomically precise impurity identification and modification on the manganese doped GaAs(110) surface with scanning tunneling microscopy*, Phys. Rev. B **78**, 075313 (2008).

[160] A. Depuydt, C. Van Haesendonck, N. S. Maslova, V. I. Panov, S. V. Savinov, and P. I. Arseev, *Scanning tunneling microscopy and spectroscopy at low temperatures of the (110) surface of Te-doped GaAs single crystals*, Phys. Rev. B **60**, 2619 (1999).

[161] R de Kort, W Kets, and H van Kempen, *A low-temperature scanning tunneling microscopy study on the Sn- and Zn-doped InP(110) surfaces*, Surface Science **482**, 495 (2001).

[162] A. M. Yakunin, A. Y. Silov, P. M. Koenraad, W. V. Roy, J. D. Boeck, and J. H. Wolter, *Imaging of the (Mn^{2+} $3d^5$ + hole) complex in GaAs by cross-sectional scanning tunneling microscopy*, Physica E **21**, 947 (2004).

[163] S. Loth, M. Wenderoth, L. Winking, R. G. Ulbrich, S. Malzer, and G. H. Döhler, *Depth Resolved Scanning Tunneling Spectroscopy of Shallow Acceptors in Gallium Arsenide*, Japanese Journal of Applied Physics **45**, 2193 (2006).

[164] C. Çelebi, J. K. Garleff, A. Y. Silov, A. M. Yakunin, P. M. Koenraad, W. Van Roy, J.-M. Tang, and M. E. Flatté, *Surface Induced Asymmetry of Acceptor Wave Functions*, Phys. Rev. Lett. **104**, 086404 (2010).

[165] Y. Rosenwaks, R. Shikler, T. Glatzel, and S. Sadewasser, *Kelvin probe force microscopy of semiconductor surface defects*, Phys. Rev. B **70**, 085320 (2004).

[166] C. Sommerhalter, T. W. Matthes, T. Glatzel, A. Jäger-Waldau, and M. C. Lux-Steiner, *High-sensitivity quantitative Kelvin probe microscopy by noncontact ultra-high-vacuum atomic force microscopy*, Applied Physics Letters **75**, 286 (1999).

[167] W. Melitz, J. Shen, S. Lee, J. S. Lee, A. C. Kummel, R. Droopad, and E. T. Yu, *Scanning tunneling spectroscopy and Kelvin probe force microscopy investigation of Fermi energy level pinning mechanism on InAs and InGaAs clean surfaces*, Journal of Applied Physics **108**, 023711 (2010).

[168] S. W. Wu, G. V. Nazin, X. Chen, X. H. Qiu, and W. Ho, *Control of Relative Tunneling Rates in Single Molecule Bipolar Electron Transport*, Phys. Rev. Lett. **93**, 236802 (2004).

[169] C. Kittel, *Einführung in die Festkörperphysik*, 14th ed. (Oldenburg, München, 2006), pp. 79, 259.

[170] L. I. Schiff, *Quantum Mechanics*, 3rd ed. (McGraw-Hill Book Company, 1968), p. 258.

[171] P. W. Anderson, *Localized Magnetic States in Metals*, Phys. Rev. **124**, 41 (1961).

[172] J. Hubbard, *Electron Correlations in Narrow Energy Bands*, Proceedings of the Royal Society of London. Series A. **276**, 238 (1963).

[173] P. Arseev, N. Maslova, V. Panov, and S. Savinov, *Nonequilibrium tunneling effects of interacting Hubbard-Anderson impurities*, Journal of Experimental and Theoretical Physics **94**, 191 (2002).

[174] M. Berthe et al., *Electron Transport via Local Polarons at Interface Atoms*, Phys. Rev. Lett. **97**, 206801 (2006).

[175] A. P. Wijnheijmer et al., *Enhanced Donor Binding Energy Close to a Semiconductor Surface*, Phys. Rev. Lett. **102**, 166101 (2009).

[176] J. K. Garleff, A. P. Wijnheijmer, A. Y. Silov, J. van Bree, W. Van Roy, J.-M. Tang, M. E. Flatté, and P. M. Koenraad, *Enhanced binding energy of manganese acceptors close to the GaAs(110) surface*, Phys. Rev. B **82**, 035303 (2010).

[177] K. Teichmann, M. Wenderoth, S. Loth, J. K. Garleff, A. P. Wijnheijmer, P. M. Koenraad, and R. G. Ulbrich, *Bistable Charge Configuration of Donor Systems near the GaAs(110) Surfaces*, Nano Letters **11**, 3538 (2011).

[178] M. C. M. M. van der Wielen, A. J. A. van Roij, and H. van Kempen, *Direct Observation of Friedel Oscillations around Incorporated Si_{Ga} Dopants in GaAs by Low-Temperature Scanning Tunneling Microscopy*, Phys. Rev. Lett. **76**, 1075 (1996).

[179] F. Mohn, L. Gross, N. Moll, and G. Meyer, *Imaging the charge distribution within a single molecule*, Nature Nanotechnology **7**, 227 (2012).

[180] M. Arakawa, S. Kishimoto, and T. Mizutani, *Kelvin Probe Force Microscopy for Potential Distribution Measurement of Cleaved Surface of GaAs Devices*, Japanese Journal of Applied Physics **36**, 1826 (1997).

[181] T. Usunami, M. Arakawa, S. Kishimoto, T. Mizutani, T. Kagawa, and H. Iwamura, *Cross-Sectional Potential Imaging of Compound Semiconductor Heterostructure by Kelvin Probe Force Microscopy*, Japanese Journal of Applied Physics **37**, 1522 (1998).

[182] A. Schwarz, W. Allers, U. D. Schwarz, and R. Wiesendanger, *Detection of doping atom distributions and individual dopants in InAs(110) by dynamic-mode scanning force microscopy in ultra-high vacuum*, Phys. Rev. B **62**, 13617 (2000).

[183] C.-S. Jiang, H. R. Moutinho, D. J. Friedman, J. F. Geisz, and M. M. Al-Jassim, *Measurement of built-in electrical potential in III–V solar cells by scanning Kelvin probe microscopy*, Journal of Applied Physics **93**, 10035 (2003).

[184] T. Glatzel, S. Sadewasser, R. Shikler, Y. Rosenwaks, and M. C. Lux-Steiner, *Kelvin probe force microscopy on III-V semiconductors: the effect of surface defects on the local work function*, Materials Science and Engineering B **102**, 138 (2003).

[185] A. Schwarzman et al., *Nanoscale potential distribution across multiquantum well structures: Kelvin probe force microscopy and secondary electron imaging*, Journal of Applied Physics **98**, 084310 (2005).

[186] S. Sadewasser, P. Jelinek, C.-K. Fang, O. Custance, Y. Yamada, Y. Sugimoto, M. Abe, and S. Morita, *New Insights on Atomic-Resolution Frequency-Modulation Kelvin-Probe Force-Microscopy Imaging of Semiconductors*, Phys. Rev. Lett. **103**, 266103 (2009).

[187] S. Kawai, T. Glatzel, H.-J. Hug, and E. Meyer, *Atomic contact potential variations of Si(111) − 7 × 7 analyzed by Kelvin probe force microscopy*, Nanotechnology **21**, 245704 (2010).

[188] T. Eguchi et al., *Imaging of all Dangling Bonds and their Potential on the Ge/Si(105) Surface by Noncontact Atomic Force Microscopy*, Phys. Rev. Lett. **93**, 266102 (2004).

[189] G. H. Enevoldsen, T. Glatzel, M. C. Christensen, J. V. Lauritsen, and F. Besenbacher, *Atomic Scale Kelvin Probe Force Microscopy Studies of the Surface Potential Variations on the TiO_2(110) Surface*, Phys. Rev. Lett. **100**, 236104 (2008).

[190] L. Olesen, M. Brandbyge, M. R. Sørensen, K. W. Jacobsen, E. Lægsgaard, I. Stensgaard, and F. Besenbacher, *Apparent Barrier Height in Scanning Tunneling Microscopy Revisited*, Phys. Rev. Lett. **76**, 1485 (1996).

[191] J. F. Jia, K. Inoue, Y. Hasegawa, W. S. Yang, and T. Sakurai, *Variation of the local work function at steps on metal surfaces studied with STM*, Phys. Rev. B **58**, 1193 (1998).

[192] J. A. Mol, J. Salfi, J. A. Miwa, M. Y. Simmons, and S. Rogge, *Interplay between quantum confinement and dielectric mismatch for ultrashallow dopants*, Phys. Rev. B **87**, 245417 (2013).

[193] F. E. Olsson, M. Persson, J. Repp, and G. Meyer, *Scanning tunneling microscopy and spectroscopy of NaCl overlayers on the stepped Cu(311) surface: Experimental and theoretical study*, Phys. Rev. B **71**, 075419 (2005).

[194] L. Vitali, G. Levita, R. Ohmann, A. Comisso, A. D. Vita, and K. Kern, *Portrait of the potential barrier at metal-organic nanocontacts*, Nature Materials **9**, 320 (2010).

[195] T. König, G. H. Simon, H.-P. Rust, and M. Heyde, *Work Function Measurements of Thin Oxide Films on Metals–MgO on Ag(001)*, The Journal of Physical Chemistry C **113**, 11301 (2009).

Acknowledgments

This thesis could not have been written without the help of many people. First and foremost, I would like to express my gratitude towards Prof. Dr. Jascha Repp, for offering me the possibility to conduct research in his lab, for his always inspiring guidance, and especially for his helpful words and deeds throughout the years. I am also deeply indebted to the other members of the Repp group, particularly to Andreas Pöllmann and Florian Albrecht for many insightful discussions and for instrumentation support. I would like to thank Dr. David Gohlke for proofreading parts of this thesis. I owe thanks to Dr. Dieter Schuh and Dr. Martin Utz from the research group for epitaxial nanostructures for providing some of the samples investigated in this thesis, and for help in wafer thinning. I am grateful to Dr. Andrea Donarini from the department of theoretical physics for many fruitful discussions on many-body physics, and for his willingness to complement our experiments from the theory side. I would like to thank Dr. Stefan Fölsch from the Paul-Drude-Institut Berlin and Dr. Martin Wenderoth from the University of Göttingen for co-authoring our joint publications. On the domestic front, I would like to thank Luise and Gerhard Münnich for giving me all possible support and encouragement. Finally, I would like to thank Caroline for more than words allow me to express.